University of Cincinnati

Date: 6/9/2011

I, Brian J Williams , hereby submit this original work as part of the requirements for the degree of Master of Science in Mechanical Engineering.

It is entitled:

Applications of Electrochemical Impedance Spectroscopy in In Vivo Corrosion Monitoring and Tissue Discrimination

Student's name: **Brian J Williams**

This work and its defense approved by:

Committee chair: Mark Schulz, PhD

Committee member: Vesselin Shanov, PhD

Committee member: David Thompson, PhD

1778

Last Printed:7/11/2011

Document Of Defense Form

Applications of Electrochemical Impedance Spectroscopy in In Vivo Corrosion Monitoring and Tissue Discrimination

A thesis submitted to the
Graduate School
of the University of Cincinnati
in partial fulfillment of the
requirements of the degree of

Master of Science

in the School of Dynamic Systems
in the College of Engineering and
Applied Science
by

Brian Williams
B.S. Georgia Institute of Technology
June 2011

Committee Chair: Mark J. Schulz, Ph.D.

ABSTRACT

This thesis summarizes work conducted in the Nanoworld lab at the University of Cincinnati studying the application of electrochemical impedance spectroscopy to provide real time data on corrosion and biofouling of electrodes implanted in live mice as well as the application of electrochemical impedance spectroscopy (EIS) for tissue discrimination. The Nanoworld lab is a member of the NSF ERC for Revolutionizing Metallic Biomaterials (ERC-RMB), where many groups are developing new magnesium-based materials and coatings for implanted devices. In vitro experimentation is inadequate to simulate the complexity of the target human tissue environment. In vivo experimentation conducted to date provides limited end point data by studying the chemical composition, mass, and other properties only at the end of the experiment.

This paper discusses the development of techniques to monitor corrosion in real time by EIS, the implementation of this technique in mice, and the development of CNT based thread as an alternative to copper wire for use in this line of experimentation. Experiments are conducted in 4 different mice, and important phenomena relevant to the state of an implanted electrode are identified. The direct electrical connection to the implants required to collect this data provide the potential to not only characterize corrosion rates but also control the corrosion rate by the application of cathodic protection. Experiments are conducted and described in this document demonstrating this potential.

Electrochemical impedance spectroscopy also provides a means to characterize tissue with a remarkable level of discrimination. Several groups have conducted research demonstrating the ability to use EIS to discriminate between cancerous tissue and healthy tissue in several tissue types. Lung surgeons at the University of Cincinnati have expressed significant interest in the potential for the application of this technique to differentiate between benign lung nodules and malignant tumors. This document describes the development of techniques and equipment to characterize tissue via EIS and describes preliminary work analyzing cancerous tissue.

ACKNOWLEDGEMENTS

I would like to take this opportunity to express my gratitude to those who enabled my research efforts. Professor Mark Schulz of the School of Dynamic Systems at the University of Cincinnati provided guidance, assistance, and support throughout the research process and acted as the chair to my thesis committee. Professor Schulz also provided financial support for me through the NSF ERC-RMB. Professor Vesselin Shanov of the Chemical and Materials Engineering Department at the University of Cincinnati also provided guidance in many of the materials related aspects of my research and also participated in my thesis committee. Dr. Zhongyun Dong in the Hematology/Oncology department provided facilities and training in the relevant biological applications. Professor David Thompson of the School of Dynamic Systems at the University of Cincinnati generously agreed to be part of my thesis committee. John Yin played a critical role in providing equipment for the execution of these experiments. Zongqing Tan provided assistance with mouse handling, animal surgeries, and other biological procedures. Doug Hurd provided a great amount of assistance in the fabrication of components for experimentation. Ron Flenniken assisted with clean room procedures for the fabrication of custom devices. Joe Kluener assisted with CNT thread spinning and mechanical testing of CNT materials. Dingchuan Xue, Mitesh Oswal and Surya Sundaramurthy provided assistance with electrochemical impedance spectroscopy and LabView.

Table of Contents

Table of Figures

1. Introduction

1.1. Summary

This document summarizes research conducted in the Nanoworld lab at the University of Cincinnati developing electrochemical impedance spectroscopy (EIS) based techniques to monitor in vivo corrosion in real time and nondestructively study properties of tissue. This first chapter will introduce basic concepts related to the research conducted and cite relevant publications. The second chapter will discuss in vivo corrosion monitoring. Chapter 3 will discuss the development and characterization of CNT based thread for use in in vivo corrosion monitoring. Chapter 4 will discuss research conducted demonstrating the potential for using cathodic protection to increase control over the degradation of implanted devices. Chapter 5 will discuss the development of techniques for the differential identification of cancerous tissue by EIS.

1.2. Electrochemistry

Basic concepts in electrochemistry relevant to the research discussed in this document are covered in this section. Electronic current is the migration of free electrons in the presence of an electric field, typically observed in metals where electrons are not confined to specific atoms. Ionic current is the migration of charged ions under the influence of an electric field in a substance permitting the movement of these ions. An electrolyte is a solution with free ions, thus facilitating ionic current. In low frequency electric fields, electrolytics dominates the electrical properties of solutions and tissue, with current carried predominantly by ion migration. At high frequencies, dielectric properties dominate, characterized by very small shifts in the positions of charges and little net movement of charge carrying species. The frequency range used in all work discussed in this document is limited to the electrolytic range.

An electrode is a point of transfer where the vehicle for current propagation shifts from electronic current to ionic current. The chemical reaction that occurs at each electrode accompanying the charge shift from electronic to ionic is known as electrolysis. A double layer will form on the surface of the electrode submerged in an electrolyte. A double layer is composed of 2 layers of ions on the surface of an object in a solution. The first is directly on the surface of the object. The second layer, of opposite charge, encases the first layer. This double layer provides a capacitive impedance to current crossing the electrode/electrolyte gap.

Electronegativity is a frequently cited quantity which is used to identify the potential for a species to become a negative ion. In particular, if a species has a higher electronegativity, than it is more likely to gain additional electrons and become a negative ion. A species' electronegativity is strongly related to its native electron configuration in its outermost shell, filled by valence electrons. As a filled valence shell is the most stable configuration for an atom, species that are closer to having this state are more likely to gain or lose electrons.

Ions are typically formed when susceptible substances, such as acids, bases, and salts, react with water. After the substance disassociates into positive and negative ions, water molecules, which form a strong dipole, form a protective layer around individual ions, acting as a barrier prohibiting the ions from recombining with ions of the opposite charge in a process known as hydration. However, these water molecules have zero net charge. As a result, within a characteristic length called the Debye length of a given ion, there exists a higher probability of finding an ion of the opposite charge than compared to the bulk solution. Furthermore, there exists a characteristic time for a local volume to adjust and restabilize in response to a sudden change in charge distribution. Such a characteristic time factor is considered a relaxation time, and will play a significant role in the electrochemical impedance spectrum of a given solution.

Conventional discussion of electromagnetics uses the variables Z for impedance and I for current. When working with electrochemistry, a different formulation is typically used in lieu of the poorly defined volume through which current flows. In particular, J is defined as the current density, with units of A/m^2, and σ for the conductivity, with units S/m.

$$J = \sigma E$$

When analyzing the ionic conductivity of a medium, one must consider the contributions of all individual species of ions present in the medium. Notably, different species may dissolve more or less frequently. As a result, γ is defined as an activity coefficient between zero and one reflecting the portion of an ion species contributing to the current density. The conductivity of a solution is considered to be independent of the frequency when working below the MHz regime. However, other factors including pH and temperature directly affect the conductivity of a medium.

Other types of electrolytes exist and are relevant to the study of bioimpedance. Colloidal electrolytes occur when mobile colloidal particles are surrounded by a charged double layer. Solid electrolytes occur when mobile ions exist in a solid. Mixed conductors exist, where both electronic and ionic conduction are possible in a medium.

Electrochemical cells are formed by putting two electrically connected electrodes in a conductive electrolyte. A galvanic cell has two unique metals for the anode and cathode, resulting in a potential between the two electrodes and a natural current flow from the cathode to the anode through the circuit. An anode is an electrode from which electrons flow into a device. The cathode is the electrode where electrons flow out of the device and back into the electrochemical cell. The cell potential can be calculated by adding the standard electrode potentials with respect to a standard hydrogen electrode. The open circuit potential can be determined by hooking a voltmeter between the anode and cathode in the absence of current flow. The voltage between the anode and cathode is dependent upon current. An electrolytic cell can be made with two unique metal electrodes or a pair of identical metal electrodes. In an electrolytic cell, an external voltage is applied, driving the current from the cathode to the anode through the circuit.

Electrochemical impedance spectroscopy (EIS) is a tool for analyzing the electrical response of a system across a range of frequencies in the applied electric field. Mathematically, impedance spectroscopy determines the transfer function between the applied voltage *V(t)* and the current *I(t)*. The impedance *Z* is defined as the transfer function:

$$Z(\omega) = \frac{V(t)}{I(t)} = Z'(\omega) + jZ''(\omega) = R + jX$$

Alternatively, the admittance *Y(ω)*, the inverse of the impedance, is defined as the transfer function:

$$Y(\omega) = \frac{I(t)}{V(t)} = Y'(\omega) + jY''(\omega) = G + j\omega C$$

Z'(ω) and *Y'(ω)* are associated with the real parts of the transfer functions, and *Z"(ω)* and *Y"(ω)* are associated with the imaginary parts, characterized by a phase offset of 90 degrees. An alternative notation commonly used defines *R* as the real resistance, *X* as the reactance (composed of capacitance and inductance), *G* as the conductance, and *C* as the capacitance. *G* and *C* can be explicitly calculated from *R* and *X* as follows:

$$G = \frac{R}{R^2 + X^2}$$

$$C = \frac{-X}{\omega(R^2 + X^2)}$$

Two more commonly used quantities, the conductivity σ and the relative permittivity ε_r, are defined as:

$$\sigma = BG$$

$$\varepsilon_r = \frac{BC}{\varepsilon_0}$$

B is a scaling factor to adjust for the geometry of the system, and ε_0 is the permittivity in free space. The magnitude of the transfer function is defined as:

$$|Z(\omega)| = \sqrt{Z'^2 + Z''^2}$$

The phase is defined as:

$$\theta = \tan^{-1}\left(\frac{Z''(\omega)}{Z'(\omega)}\right)$$

Bode plots and Nyquist plots are commonly used to plot transfer functions. Bode plots consist of 2 plots; the first maps the magnitude of the transfer function as a function of the log of the frequency, and the second maps the negative phase (linear scale) as a function of the log of the frequency. Nyquist plots map the imaginary part as a function of the real part of the transfer function. Figure 1 and Figure 2 contain a sample Bode plot and Nyquist plot, respectively. Each plot is useful for identifying different phenomena in the transfer function.

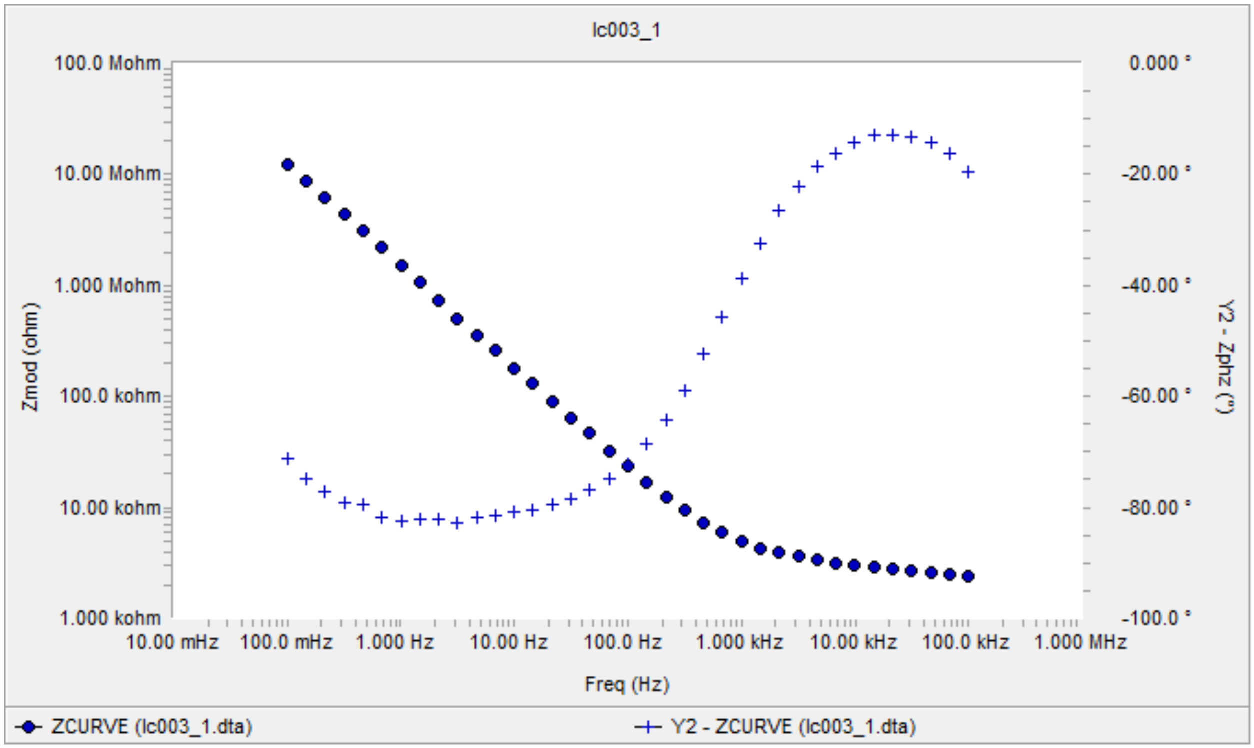

Figure 1: Sample Bode plot. Dots plot magnitude of impedance, and crosses plot phase

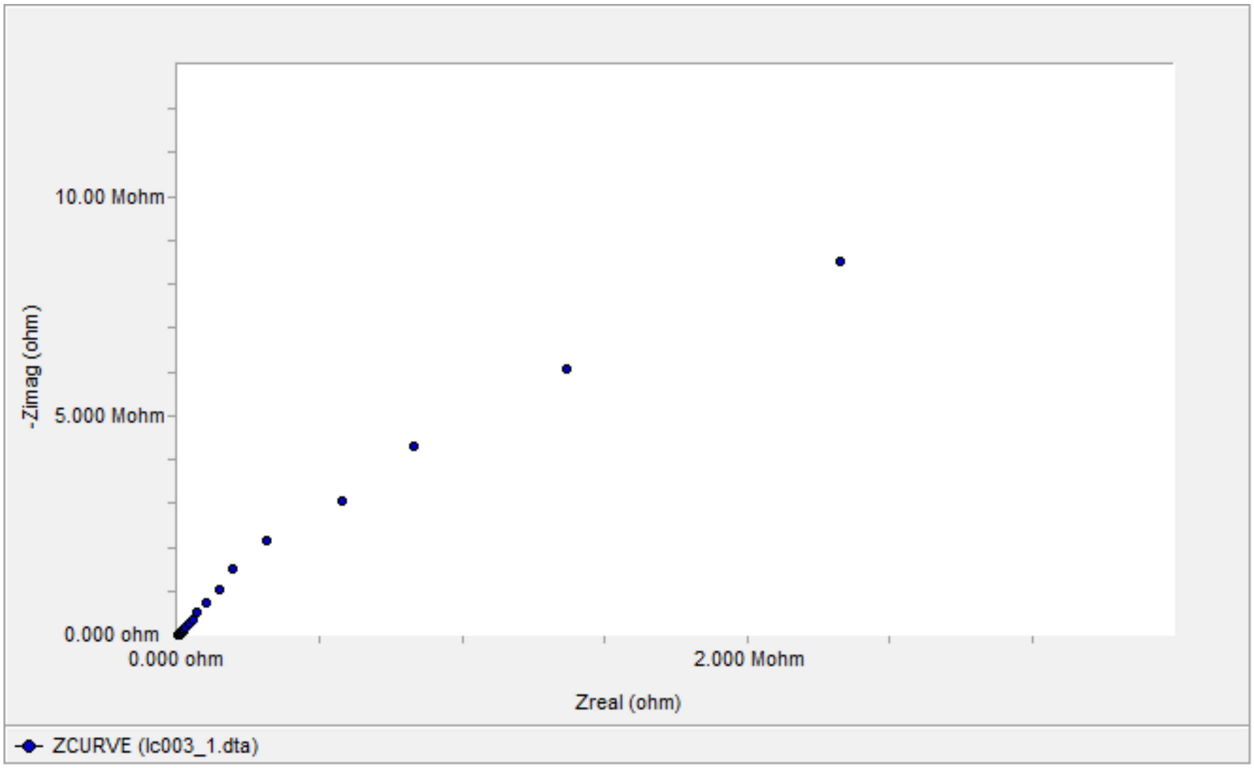

Figure 2: Sample Nyquist plot, with real part on x-axis, and negative imaginary part on y-axis

In the lab, a potentiostat is used to conduct EIS. Most commonly, a 3-electrode configuration is employed, with a working electrode, counter electrode, and reference electrode. The working electrode is connected to the material under study. A reference electrode is a self-contained half cell with constant, known potential. A commonly used reference electrode is an Ag/AgCl electrode, which consists of a silver electrode bathed in a silver chloride solution. Such a setup typically employs a small glass housing for the silver chloride solution and silver wire with a small hole exposing the reference electrode to the solution while minimizing loss of the silver chloride solution. The potentiostat will maintain the potential of the working electrode with respect to the reference electrode. The counter electrode is used as either an anode or cathode to permit the transmission of current to or from the working electrode. [1]

1.3. Electrochemistry in Tissue

Tissue behaves as an electrolytic material at low frequencies (typically less than 1MHz) and a dielectric material at high frequencies. The frequency range of all experimentation conducted by the author in this document is in the low frequency range. As such, particular focus will be given to electrolytic properties of tissue.

Na^+ is, by far, the most common cation in blood, and Cl^- is the most common anion. Inside the cell, K^+ is the most common cation and HPO_4^{2-}, SO_4^{2-}, and other organic acids are the most common anions. Other common cations in tissue include Ca^{2+}, Mg^{2+}, and H^+. Other common anions in tissue are HCO_3^- and protein. Proteins, which are particularly common inside cells, are considered a negative macro ion. Proteins are composed by amino acids. Amino acids have varying electrical properties that change with pH. For example, a given amino acid may have net charge for high pH, and be electrically neutral at lower pH. Amino acids typically exhibit a dipole. As previously discussed, water molecules form a sheath layer around ions and local areas of net charge. When sheathing proteins, water can be attracted with such a large magnitude that its properties change and the material becomes known as bound water.

Full protein structures are composed of many amino acids. These complex chains can form many complex structures. Extreme or excessive characteristics in the environment, such as temperature or pH, can denature a protein, destroying the geometric structure and changing its biological function. A protein characterized by having a net charge is called a polyelectrolyte, and is capable of contributing to ionic current. Carbohydrates, used as a fuel for cellular activity, do not contribute significantly to the electrical properties of tissue.

The passive cell membrane is composed of polar lipids. Bilayer lipid membranes are composed of two monolayers of lipids. The polar structure of lipids results in a hydrophobic side and a hydrophilic side. A bilayer is formed with the hydrophobic side of each layer facing the center. The hydrophilic side of each monolayer faces outwards, towards either the intracellular or extracelluluar environment. The cell membrane also contains active components such as active ionic channels, which are capable of selectively permitting the flow of ions and other structures through the cell membrane in a controlled direction. These active mechanisms enable the cell to maintain a negative potential inside the cell compared to the extracellular environment, typically in the range of -10 to -70mV.

Electrically, the bilayer lipid membrane has very low conductivity, and active transport mechanisms are typically modeled as shunt pathways in parallel with the bilayer lipid membrane. Because the bilayer lipid membrane is so thin (approximately 7nm), it acts as a capacitor with a low breakdown potential (at approximately 150mV). The capacitance is often considered to be frequency independent, with values on the order of 20 $\mu F/cm^2$. [2]

Dispersion in dielectric materials defines the frequency dependent permittivity of a material. Relaxation is the associated time delay required for a material to reach equilibrium in the presence of some form of disturbance. In particular, certain types of relaxation contribute heavily to the dielectric properties of a material under excitation in specific frequency ranges. When observing EIS data in tissue, several dispersion regions are of particular importance. The γ-dispersion occurs with relaxation due to the polarization of water molecules in the gigahertz regime. β-dispersion occurs with relaxation of the polarization of cellular membranes and proteins, and typically occurs on the order of 100kHz. α-dispersion occurs at lower frequencies and is associated with relaxation of ionic transport processes across the cell membrane. Other dispersion regions may be observed depending on the tissue and cell type under investigation. [3-5]

Tissue is a significantly more complex, inhomogenous electrical structure. Functional arrangement of layers and cells mean that the electrical properties in tissue are often anisotropic. In extreme cases, the conductivity in one direction may differ in magnitude from that in another by a full order of 10. If we consider a simplified tissue consisting of cells in a conductive medium, current path is highly frequency dependent. At low frequencies, the high capacitance of cell membranes will resist intracellular current, resulting in a current path that twists around cells. Liquids saturating the extracellular regions of tissue exhibit DC conductivities on the order of $1S/m$. However, certain tissue layers, such as epithelial layers, are characterized by extremely tight cell packing with a resultant low DC conductance. At higher frequencies, the cell membrane provides little resistance, and the resultant current path will go straight through cells and the surrounding medium. The observed conductivity in tissue is highly temperature dependent. Different tissue types exhibit significantly different electrical properties. Of particular interest to the work covered in this document are muscle tissue and blood.

Muscle tissue can be classified as skeletal muscle, smooth muscle, and cardiac muscle. Skeletal muscle is a highly anisotropic tissue composed of collinear fibers made of myosin and actin proteins. The highly ordered structure facilitates the application of force along a specific direction. It also results in the highly anisotropic electrical properties of skeletal muscle tissue. Electrically, muscle tissue has a very large α-dispersion, particularly in the direction parallel to the muscle fibers. Perpendicularly to muscle fibers, a β-dispersion is present. Smooth muscle is another type of muscle with less exaggerated anisotropic electrical properties. Smooth muscle can be found in vessels and tracts.

Whole blood consists of red blood cells, or erythrocytes, and plasma, which is composed of electrolytes and other charged particles. Whole blood is electrically characterized to have β-dispersion, γ-dispersion, and δ-dispersion in the MHz and greater regime, beyond the frequency range used in the experiments discussed in this document. α-dispersion is not observed in whole blood. [2]

1.4. Corrosion

Corrosion is the deterioration of a material initiated by electron transfer. Two reactions occur during corrosion: an anodic reaction where a chemical species loses electrons, and a cathodic reaction where a species gains electrons. Many types of corrosion have been heavily studied, including atmospheric corrosion, galvanic corrosion, crevice corrosion, filiform corrosion, pitting corrosion, biological corrosion, and selective leaching corrosion. Galvanic corrosion and pitting corrosion are of particular relevance to the research conducted in this lab.

Galvanic electrochemical corrosion occurs when two metals with different potentials are connected and exposed to an electrolyte, permitting current flow from the metal with a more negative potential to the metal with a more positive potential. Individual types of metal have a characteristic standard metal potential determined by measuring the voltage compared to a standard hydrogen electrode. In general, the rate of corrosion increases with current flow, which increases with the potential difference between the two metals creating the galvanic cell. Thus proper selection of the metals in the cell can either enhance or limit galvanic corrosion. The microstructure of a metal exposed to an electrolyte is a source of galvanic corrosion. Crystal defects and potential differences across grain boundaries induce current flow and corrosion.

Pitting corrosion forms very small pits in the surface of metal structures. This corrosion is induced by small defects in the surface of the metal that induce anodic and cathodic reactions. Pitting corrosion is typically constrained to a very small area. As a result, it provides little mechanical damage to adequately large structures. However, pitting corrosion can substantially reduce the strength of a surface layer. [6]

1.5. EIS Corrosion monitoring

A thorough study of the corrosion of new materials is critical for many applications, particularly in biomedical devices. Magnesium alloys, for example, are considered a promising candidate for the construction of biodegradable implantable devices. To provide more control over the exact corrosive properties of these devices, novel alloys and coatings are being studied. The ERC-RMB is active in this research. Common studies employ immersion tests in a corrosive medium intended to simulate the environment of the end application, such as bodily fluids.

After immersion for a specified period of time, conventional methods to analyze the corrosive activity include mass comparison, mechanical testing, scanning electron microscopy (SEM), energy dispersive X-ray spectroscopy (EDS), X-ray diffraction (XRD), and Fourier transform infrared spectroscopy (FTIR). These tests all require the removal of the sample form the corrosive environment, making it impractical or impossible to obtain data with a high enough frequency to develop accurate timelines describing the evolution of corrosive activities in the system. Concentrations of ions of interest in the solution can be measured by inductively coupled plasma atomic emission spectrometry or with ion concentration sensors dedicated to the species of interest.

During the immersion of the sample, real-time data can be obtained by monitoring hydrogen production and by using electrochemical impedance spectroscopy [7-24]. For example, J. Chen et al. [7] used EIS to monitor the corrosion of AZ91 in sodium sulfate solutions. This research group observed the evolution of capacitive loops in mid frequency ranges coincident with the development of integrated corrosion forms on the surface of the samples. Capacitive loops in high frequency ranges represented the double layer effect. Other inductive and capacitive loops were attributed to surface state variables. The availability of such data permits the research to formulate a detailed timeline of the development of relevant corrosive events occurring during the experiment. In particular, the researcher is able to determine precisely when certain chemical reactions start occurring by matching electrical models and the EIS data with the expected reactions.

Other electrochemical techniques can be used to study the corrosive behavior of a sample in solution. The corrosive potential (E_{corr}), the corrosive current density (I_{corr}), and the electron transfer resistance (R_{et}) can be compared between different samples. Increased I_{corr} is associated with increased corrosion rates, and R_{et} indicates a materials resistance to corrosion. H.M. Wong et al. [8] found the corrosion potential (E_{corr}) for various coatings on magnesium-based structures.

They show that the coated materials exhibit higher corrosion resistance associated with increased corrosion potentials.

Several important quantities can be determined by analysis of the impedance transfer function. The solution resistance R_s is the resistance to charge transfer contributed by resistance to ion migration in the solution. The polarization resistance R_p is used to determine the corrosion current density I_{corr}, which is then used to determine the rate of corrosion. The double layer capacitance C_{dl} is the capacitive contribution to the impedance caused by resistance to charge transfer past the double layer formed at the surface of the electrode. The diffusion impedance Z_D, related to the Warburg impedance, characterizes diffusion contributions to the impedance. [6]

1.6. Corrosion Control

Many applications in the ERC-RMB require controlled corrosion rates for implanted devices to ensure that the device is intact for long enough to accomplish its designed function but biodegrades in order to eliminate the need for a second surgery. Proper selection of material properties may yield a device that meets these requirements. Active corrosion control methods have the potential to increase the utility of such devices by permitting the user to actively control the corrosion rate after the implant procedure is complete. Cathodic protection is a common method of corrosion control which is being investigated by the ERC-RMB for use in implantable devices.

Cathodic protection is a method of reducing or stopping corrosion rates by suppressing anodic reactions on the structure of interest. Corrosion occurs when current flows from the corroding surface resulting in oxidation and the deterioration of the material on the surface. By applying an external power supply, the potential at the surface of the structure can be controlled and driven beneath the corrosion potential.

As an alternative to achieving cathodic protection by applying an external power source, a sacrificial anode can be used to control the potential on the structure of interest and similarly suppress corrosion. The sacrificial anode must be connected to the structure of interest, and the material of the sacrificial anode must be selected such that it is anodic compared to the structure. As a result, electrons will flow from the sacrificial anode to the structure of interest. [6]

1.7. EIS inspection of cancerous tissue

The electrical properties of tissue are extremely sensitive to changes in cellular morphology. Cancerous tissue frequently displays distinct differences in cellular morphology. Several groups have conducted research applying EIS to discriminate between cancerous tissue and healthy tissue [25-34]. There are two broad approaches to this problem. First, the researcher can collect large quantities of data, and statistically identify which features calculable from the data are most effective in identifying cancerous tissue. Da Silva et al. [25] used this approach in a study that successfully found criteria to distinguish carcinoma from other types of breast tissue.

Figure 3 plots a sample Nyquist plot for an ideal tissue measurement. Several simple parameters are labeled on the plot. Many of these parameters are not commonly used in the study of electrochemistry but are geometric parameters of the measured curve that have potential for use in discrimination of tissue type. IP_{MAX} is the maximum imaginary part of the measured impedance. I_0 is the real value of the impedance associated with zero imaginary impedance at the lower frequency limit. This value typically needs to be extrapolated from the available data. D_A is calculated as the distance between I_0 and the other extreme of the curve. *AREA* is the area underneath the curve, and $AREA_{DA}$ is the area scaled by the value D_A.

The group collected 104 usable datasets from 64 patients with 6 different tissue classes present. 3 normal, healthy tissue classes included in the dataset were connective tissue, adipose tissue, and glandular tissue. 3 pathological tissue classes present were carcinoma, fibro-adenoma, and mastopathy. The group conducted a linear discriminant analysis to determine what values calculable from the EIS data are effective for identifying the associated tissue class. Care was taken to determine a function of an appropriate number of variables; too few variables would limit the ability to identify tissue class, and too many variables would overfit the data, limiting its ability to predict tissue classes for data not included in this study.

Results of the linear discriminant analysis identified I_0, $AREA_{DA}$, and IP_{MAX} as the most appropriate parameters for tissue discrimination. I_0 was effective for discriminating between adipose tissue, connective tissue, and the group of glandular tissue, carcinoma, fibro-adenoma, and mastopathy. Both $AREA_{DA}$ and IP_{MAX} were effective for discriminating between carcinoma and the group of glandular tissue, fibro-adenoma, and mastopathy. The result of the identification of these parameters was the discrimination of breast cancer from healthy tissue with a success rate of approximately 92% and the discrimination of carcinoma from other tissue classes with a success rate greater than 86%. The entire experiment was conducted without employing a tissue model. [25]

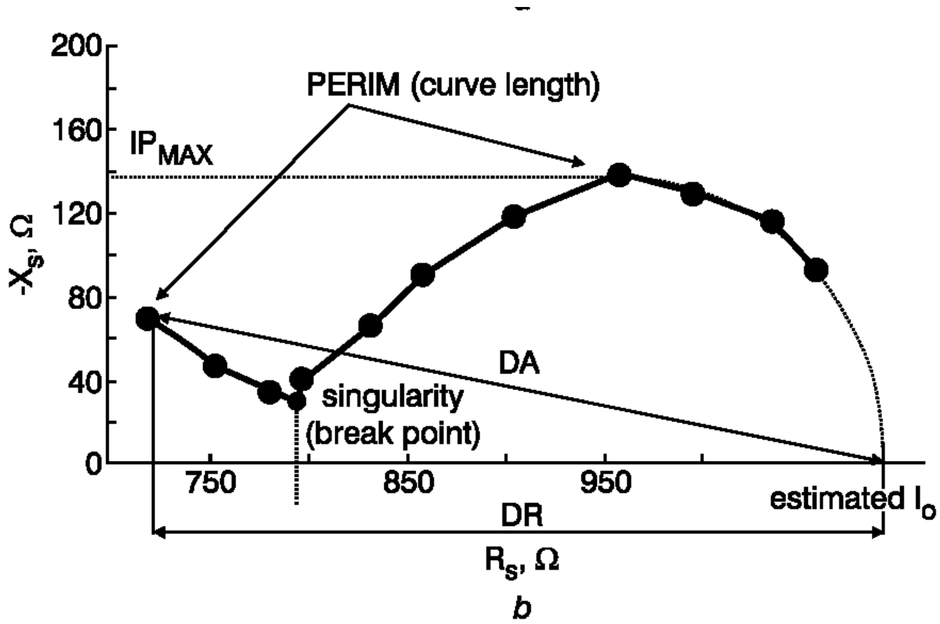

Figure 3: Computed quantities used in discrimination of carcinoma (da Silva, J. E., de Sa, J.P. M., Jossinet, J. Classification of breast tissue by electrical impedance spectroscopy. Medical & Biological Engineering & Computing 38 (2000) 27.)

Other groups' work employ tissue models and use insight provided by the modified morphologies of cancerous tissue to identify potential shifts in the EIS data that may permit tissue discrimination. Halter et al. [26] and Lee et al. [27] conducted research that took advantage of such a shift in cellular morphology in the analysis of prostate cancer. Prostate cancer development typically occurs in the peripheral region of the prostate and is associated with dense regions of epithelial cells. Epithelial cells line surfaces and walls of organs and other structures in the body. The healthy prostate consists of a network of ducts. Each duct is lined with two layers of epithelial cells. Cancerous regions of a prostate are characterized by densely packed regions of cancerous epithelial cells, leading to an increase in the density of the gland. With this increased density, the impedance associated with current paths flowing around cells increases, resulting a decrease in conductivity.

Figure 4 plots the average conductivities and relative permittivities for healthy (dashed line) and cancerous (solid line) tissues from 5 different samples measured less than 20 minutes after removal from the patient. Measurements are taken with a coaxial probe with an estimated measurement volume of $46mm^3$ and a frequency range of 10kHz to 1MHz. The healthy tissue measurements are taken in the symmetric position from the cancerous measurement on the same prostate, minimizing the effect of variation in tissue properties associated with different location in the prostate. The data consistently shows a decrease in conductivity for cancerous tissue, as predicted by the observed change in tissue properties in cancerous regions. Histological data, including cell type and gleason score, is used to support this data. [26]

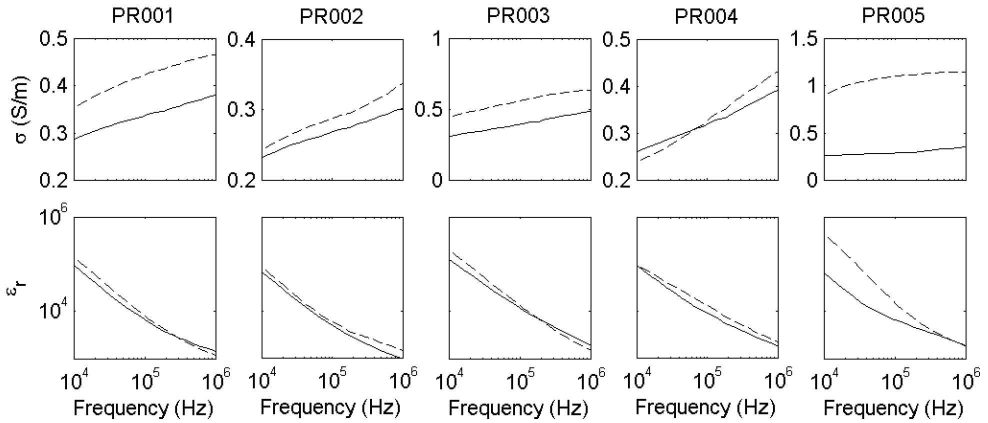

Figure 4: Comparison of conductivity and relative permittivity for healthy (dashed lines) and cancerous (solid lines) tissue. Halter, R.J. et al. Electrical Impedance Spectroscopy of the Human Prostate. Transactions on Biomedical Engineering 54 (2007) 1325.

The application of EIS to identify cancerous tissue has the advantage that multiple tissue locations can be studied with limited cost and with real-time feedback. Furthermore, this application can potentially be used not only to identify cancerous tissue but fight cancer. By applying electrical pulses on the order of 1kV/cm, cells are electroporated, increasing the rate at which these cells absorb medicine. As a result, the application of toxic medicine can be localized to a degree by pretreating tissue regions of interest with electroporation and increasing their susceptibility. Furthermore, Tang et al. [28] have conducted research demonstrating the ability to induce apoptosis (programmed cell death) with electric pulses. The group successfully manipulated the intracellular behavior of target cells and observed the externalization of phosphatidylserine on the plasma membrane, an indicator of apoptotic cells. This approach has the potential to provide a completely drug-free method of battling cancer. [28]

Other impedance methods are under consideration for the identification of cancer. Preliminary research has been conducted in the Nanoworld lab using a clamp type apparatus to physically contact a target cell species from two points of contact and use impedance to identify the presence and concentration of the target cell. This concept is illustrated in Figure 5. This method requires that only the target cell type is immobilized on the surface of the apparatus, which can be achieved by coating one surface with suitable antibodies. By patterning the electrode surfaces with microstructures on the order of the size of the target cell type, a uniform, controlled minimum gap can be achieved between the two surfaces, ensuring that the apparatus does not crush the immobilized cells. By measuring impedance directly across the cells without a solution impedance, a greater sensitivity can be potentially achieved.

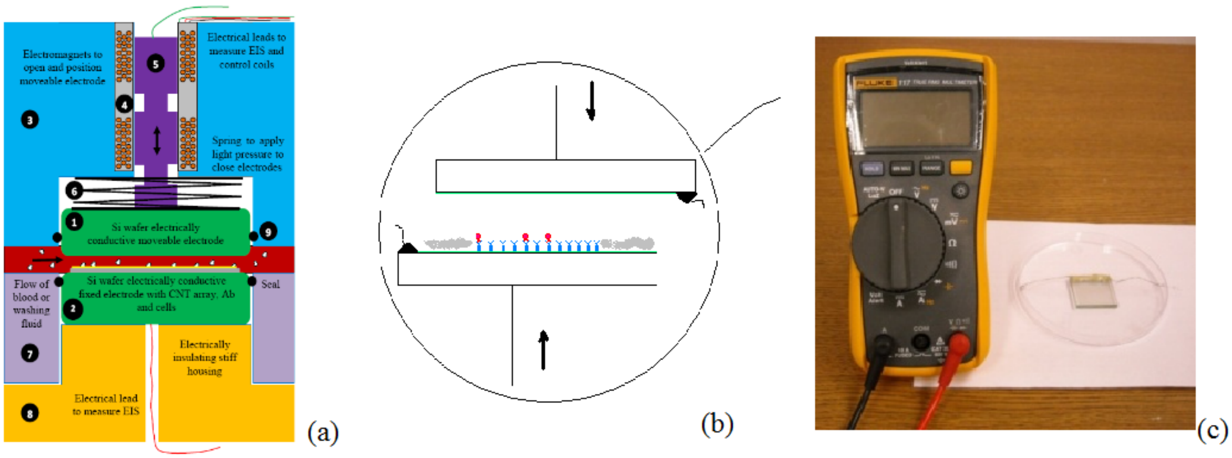

Figure 5: Illustration of alternative impedance based method for identification of target cell species

2. Electrochemical Impedance Spectroscopy monitoring of implanted magnesium electrodes

2.1. Summary

The ERC for Revolutionizing Metallic Biomaterials (ERC-RMB) conducts research for the application of magnesium biodegradable devices. In vivo data is required to supplement extensive in vitro experimentation. Previous in vivo experimentation has been conducted by the ERC-RMB in which samples were implanted in mice. The samples were left in the mouse for several weeks, removed, and analyzed, providing data on mass change, chemical compositions on the surface, and mechanical properties. This data provided limited insight to what was occurring in the mouse.

Significant research has been conducted using electrochemical impedance spectroscopy (EIS) to monitor corrosion in real time to provide additional data in characterizing corrosive activities of magnesium samples implanted in living mice. This approach has several significant problems. There is no evident way to employ a typical reference electrode in vivo. As such, measurements would be required to use a simplified 2-electrode setup. This setup reduces the accuracy and physical significance of the obtained impedance spectra. Even with this limit on accuracy, significant insight can still be gained.

Second, running a wire through the skin poses significant issues. Using a metal wire is likely to cause significant irritation to the skin, resist proper wound healing, and make the subject susceptible to infection. Alternative electrical current delivery materials, such as CNT thread, have large resistances and questionable material properties for this application. Several experiments were conducted, with varying experimental procedures and material selections. This chapter summarizes the development of these techniques and materials for the monitoring of corrosion and biofouling via

EIS in live mice. Several mice are used in the course of the experimentation. To differentiate between mice, each subject is identified by a letter in the Greek alphabet, i.e. 'alpha' or 'beta'.

2.2. Experiment

2.2.1. Equipment

Data in the first set of experiments was collected with a CH Instruments CHI660C potentiostat. A simplified 2-electrode configuration is used by connecting the working lead of the potentiostat to one of the two implanted electrodes and connecting both the counter electrode and the reference leads of the potentiostat to the other implanted electrode. This simplification to 2 electrodes limits the accuracy of the data. Data was collected using the potentiostatic AC impedance method applying voltages with a 5mV amplitude and frequency range from 1 to 100,000Hz.

Later experiments employed a Gamry potentiostat. A Series G 750 PCI card potentiostat is used. Unless otherwise specified, the standard settings used to collect EIS data are a 5mV amplitude with a frequency range of 0.1Hz to 100kHz. 6 points per decade are collected by default. The Gamry is capable of going down to 0.01 Hz, however, for most applications covered in this document, the time requirements for this low frequency data were excessive.

2.2.2. Electrode Fabrication

All electrodes are fabricated in the Mechanical Engineering department. Samples are cut on the lathe in the Mechanical Engineering machine shop under the guidance of Doug Hurd. Starting with mouse 'beta,' sample dimensions are standardized between experiments, as dimensioned in Figure 24. With the small size of the samples, extreme caution must be taken to minimize the size of metal nipple left on the sample when it falls off of the metal stock. If a straight cutting tool is used, the resultant excess metal on the sample is greater than 1mm in diameter. Attempts to remove this significant piece of metal with a chisel typically end up damaging the sample. To get around this, a cutoff tool is customized with an approximately 30 degree angle to minimize the thickness of the nipple at the point where it contacts the final sample, making the removal of this excess metal with a chisel easy.

Graphite samples are fabricated with an identical methodology and dimensions as magnesium samples. However, when cutting graphite on the lathe, a vacuum must be set up such that the hose is placed in close proximity to the cutoff tool to suck up graphite particulates and minimize harmful inhalation of these powders.

Depending on the experiment, either copper magnet wire or CNT wire is used to provide a transdermal electrical connection to the electrodes. When using copper magnet wire, the insulating enamel coating must be removed from the wire at the point where the wire is to be connected to the sample and at the point where the potentiostat alligator clips will be attached. This is accomplished by locking the wire in a clamp and carefully scraping off small sections of the enamel with a razorblade, taking care to remove the coating around the entire circumference of the wire.

Once the enamel is removed and the wire is cut to length, the wire is attached to the sample with silver conductive epoxy. When attaching magnet wire, Epoxy Technology H20E silver conductive epoxy is applied in very small quantity to the top of the sample. The magnet wire is placed on top of the epoxy dot and tamped into place with a wooden dowel. The sample is cured at 120 degrees Celsius for 20 minutes. Finally, to ensure that all current pumped through the wire is forced through the magnesium sample, the entire top surface of the sample is coated with a nonconductive epoxy. Initial experiments used Permatex PermaOxy general purpose epoxy. After observing that this epoxy would prematurely fail in corrosive environments, Buehler EpoKwick was used for later experiments. This lower viscosity epoxy requires careful application on the small diameter samples to ensure that the insulating epoxy was constrained to the top of the sample.

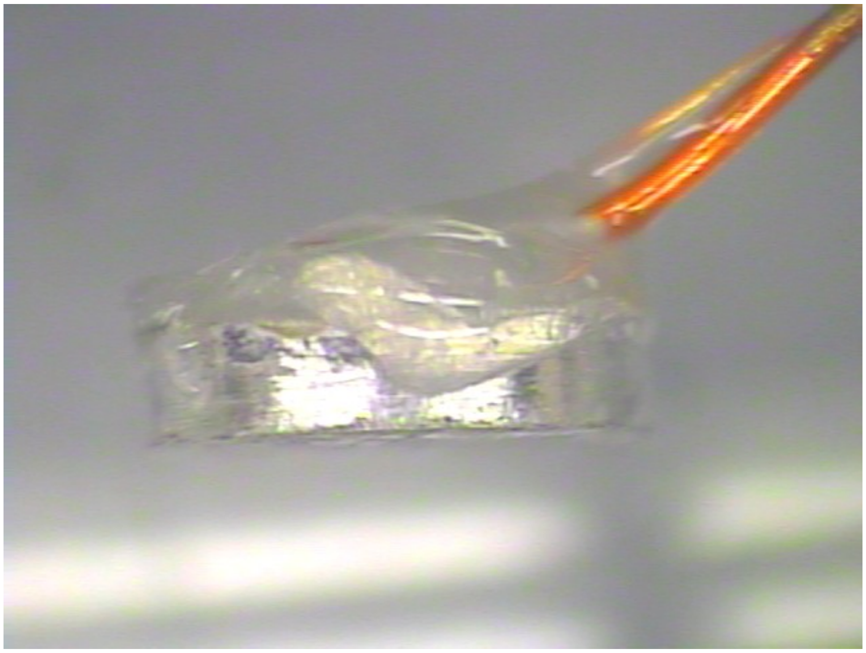

Figure 6: Mg electrode connected to copper magnet wire

Samples fabricated with CNT wire required a different attachment procedure. A PVC coated CNT thread was provided by Atkins and Pearce for these experiments. The PVC coating provided an electrically resistant layer, as characterized in Chapter 3. To selectively remove this insulating coating at the locations where the thread was to be attached to the sample or to the potentiostat alligator clips, the thread was submerged in THF for 20-30 seconds. This time was determined appropriate after the characterization conducted in Chapter 3. This CNT thread could not be attached to the sample with the Epoxy Technology silver epoxy because curing at 120 degrees Celsius would damage the PVC coating. Instead, Chemtronics CW2400 conductive silver epoxy was used, which can be cured at room temperature in 4 hours. The final epoxy was softer than the Epoxy Technology epoxy, but after coating with an insulating epoxy this is not a problem. Once again, Buehler EpoKwick epoxy was used to provide a protective insulating layer on the top face of the samples.

Particularly if working with a black haired mouse, the visibility of the electrode wire must be considered. Experimentation with the coated CNT thread also demonstrated inconsistent connectivity when connecting to the wire by touching directly with a probe. To address both of these issues, small pieces of copper were attached to the exposed, uninsulated section of the CNT thread. To make this copper section, two strips of copper tape are cut to a size significantly larger than the desired final size. All adhesive is removed by scrubbing with acetone, as the adhesive showed unstable conductivity. The uninsulated section of the thread is attached to the face of one of the strips with a small quantity of conductive epoxy. The second strip is laid on top of the thread and the first piece of copper. After curing, the final copper shape is cut from the strip, as shown in Figure 7 and Figure 8.

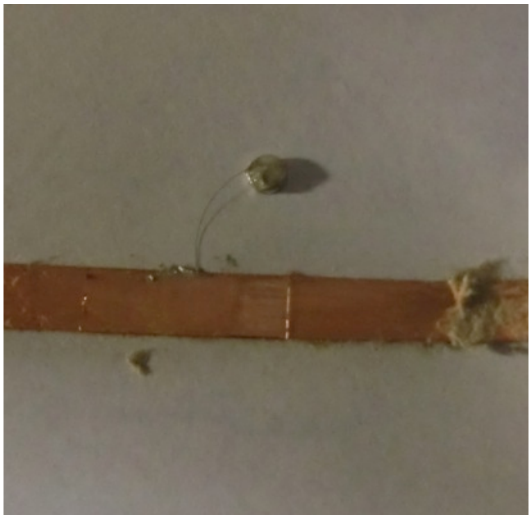

Figure 7: Mounting of copper contact strips to end of CNT thread

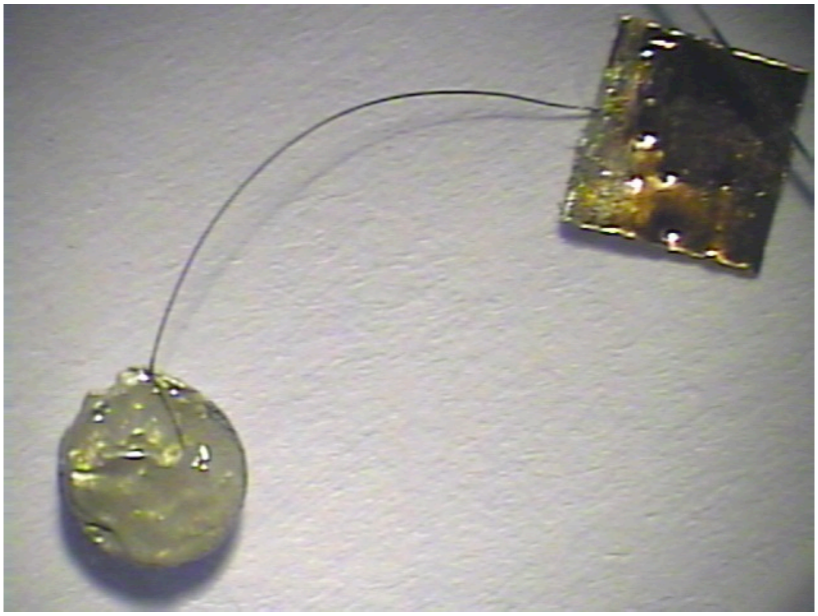

Figure 8: Final CNT thread connected Mg electrode with copper connection tab

2.2.3. Mouse Handling

For all implant experiments, the subject mouse is stored in it's own cage to eliminate the possibility of other mice chewing on the exposed wires. In compliance with IACUC regulations after the recent Hook Worm infection, the subject mice are kept in the 'Return Room,' and brought to and from Dr. Dong's lab whenever measurements are taken. Transportation requires PPE, including booties and gown upon entrance to the facilities, and a second layer of PPE inside the return room. The cage must be covered with a drape and taped securely when transporting the mouse outside the animal facilities. A filtered lid and functioning water bottle must be provided prior to transport.

To minimize signal noise during EIS measurements, the mouse must be immobilized. It is unadvisable to knock the mouse out with medication for every measurement. Instead, mouse immobilization tubes were made from 50mL vials. A small hole was cut in the bottom of the tube to permit the mouse to breath. A hole was cut in the lid to make it possible to thread the tail through. Holes were cut in the side of the vial at the estimated location of the electrodes to enable access with the copper clips. Several tubes were made with electrode holes in different locations to ensure proper fit.

All experiments were conducted in the fume hood in the Vontz center lab. To immobilize the mouse, the filtered lid is removed from the mouse cage and set aside. The cage lid used for holding food and water is lifted with one hand, and the other hand is used to pick the mouse up by the tail and remove the mouse from the cage. The wire lid is replaced, and the mouse is set gently on the wire lid, permitting it to grab the wire. The second hand is used to gently pinch the skin on the upper back, just beneath the ears, between the forefinger and thumb. The pinky is used to hook the tail of the mouse, thus enabling complete control of the mouse with one hand. The free hand is used to guide the head of the mouse into an immobilization tube. At this point, the mouse can be gently pushed into the tube. Kim wipes are used to constrain the mouse all the way in the front of the tube. The lid is screwed on to trap the mouse in the tube.

The tube is taped down to the floor of the hood. Loose sections of potentiostat wires are taped to minimize how much they can pull on the mouse. One copper alligator clip, connected to the reference and counter electrodes of the potentiostat, is clipped on to one of the wires on the mouse. Another copper alligator clip, connected to the potentiostat's working electrode, is clipped to the remaining implanted electrode. Initially, a pair of alligator clips soldered onto regular hookup wire with insulated outer diameter of 2mm was used to make these connections. After the first measurement, it became obvious that the force applied by these alligator clips combined with their sharp edges would destroy the low diameter wires attached to the electrodes on the mouse. Destruction of the wires connected to the implanted electrodes would prematurely end the ability to collect data from the subject. As a result, a new pair of clips were made using copper spring clips with flat surfaces. These new clips did not bend the electrode wire and applied less force. The diameter of the hookup wire attached to these alligator clips was minimized to reduce the force applied to the implanted electrodes. These new clips were extremely light and flexible, minimizing pull on the electrode wires.

2.3. Results

2.3.1. Implants in dead mouse

Prior to implantation in a live mouse, a trial experiment was conducted in a deceased mouse to verify the ability to collect meaningful data. Approximately 30 minutes after sacrificing a black haired mouse, approximately 1cm incisions were cut in the back of the deceased mouse. A pair of square cut magnesium pellets with hookup wire connectors was placed on the underlying muscle tissue, allowing the separated skin to come back down and hold the electrodes in place. The scale of these electrodes is depicted in Figure 9. EIS scans were taken with standard settings on the CH potentiostat.

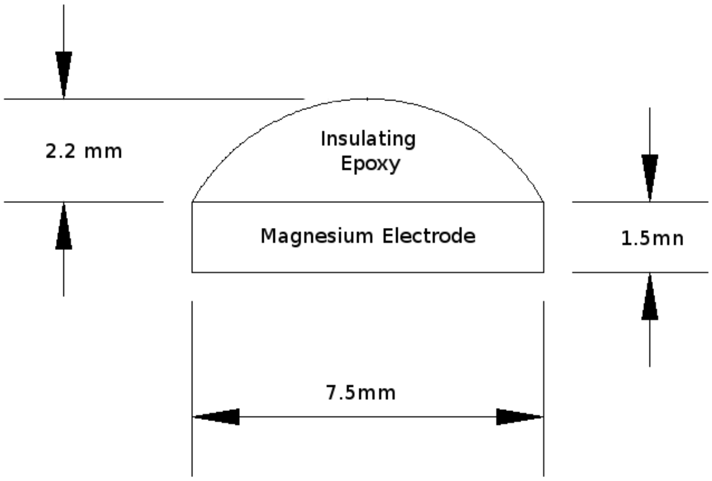

Figure 9: Size of square cut magnesium electrodes used in preliminary experiment on deceased mouse

3 trials were taken, varying the separation between the pair of electrodes from 0.5 cm, to 1.5 cm to 3.0 cm. Resultant Bode plots are found in Figure 10. The resultant plots are, not surprisingly, similar in form to those taken in tissue impedance measurements collected with a pair of tungsten needles discussed in Chapter 5. The observed impedance is predominantly resistive with low phase. A local maximum in the phase occurs around 15 Hz, and a local minimum in the phase occurs around 2000 Hz. Some variance in the frequency location of this minima and maxima is observed, with an

apparent decrease in the frequency location associated with an increased electrode separation. There is not enough data present, however, to make any statistically valid assertions from these observations.

The magnitude plots exhibit increasing impedance associated with lower frequencies and increased impedance associated with increased electrode separation. This is particularly evident comparing the 5mm separation trial with either the 15mm or 30mm separation trials. Noise is present in the plots, particularly in the phase. Use of the Gamry potentiostat would likely eliminate this issue, as this piece of equipment takes several measurements at each frequency to reduce error. Even with the noise, the general behavior of the system is easily observable.

The data collected provided ample justification for the general electrode type, implant location, and data collection procedure. Preparations to implant in a live mouse were initiated, with plans to reduce the size of the electrodes to reduce potential discomfort in the animal.

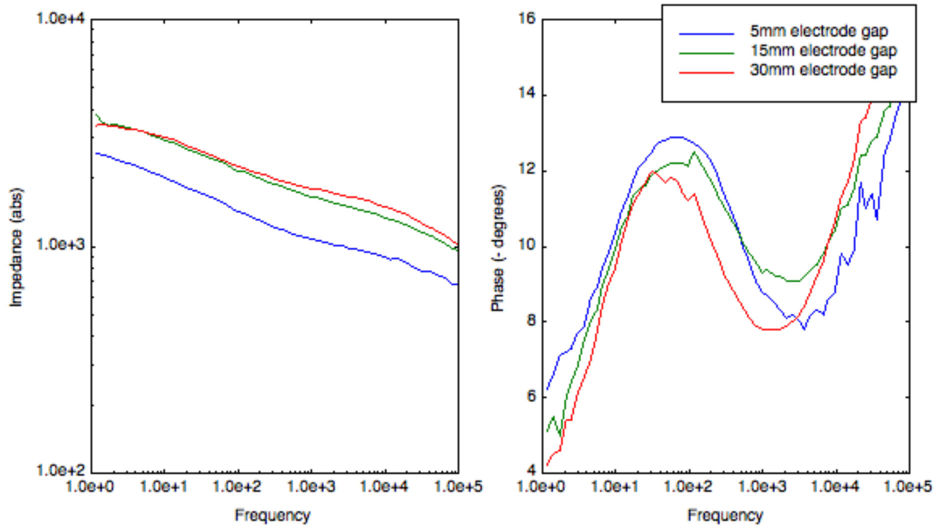

Figure 10: Bode plots from preliminary in vivo EIS data collection in deceased mouse.

2.3.2. Implants in mouse 'alpha'

The first live mouse, dubbed mouse 'alpha', was tested with a pair of implanted magnesium electrodes. The second electrode was chosen to also be magnesium instead of a more conventional selection of the counter electrode (like platinum) to minimize the number of variables in the system and ensure that all changes observed in impedance spectra are caused by corrosion or biofouling of the electrode material of interest. The electrodes were implanted subcutaneously in the mouse by Zongqing Tan in the procedure room of the Vontz Center animal facility. In this subject, the electrodes were implanted with a gap of 15mm in the lower back, about 20mm above the tail. Two different electrodes were used: a round Mg electrode with 3.84mm diameter and magnet wire was implanted on one side, and a square Mg electrode with 4mm sides and thin hook-up wire on the other. The use of different shaped electrodes was selected for this experiment to help determine the optimal implant geometry to standardize for future experiments. The insulation of the hookup wire was left for the portion expected to be beneath or in direct contact with the mouse's skin. Both electrodes were sterilized by UV exposure prior to the procedure. The wounds were closed with surgical clips. These clips, which have very high conductivity, came into contact with the exposed wire of the electrodes. This is not ideal, and a problem to be anticipated in future repeats of the experiment.

1 day after the implantation, the first EIS measurement was collected with the CH potentiostat. Relevant plots can be found in Figure 11. Very little phase change is observed, resulting in a noisy Nyquist plot. Comparing the data to that obtained from trial experimentation in the dead mouse validated the data, reducing concern of the measurements being excessively affected by the conductive surgical clips.

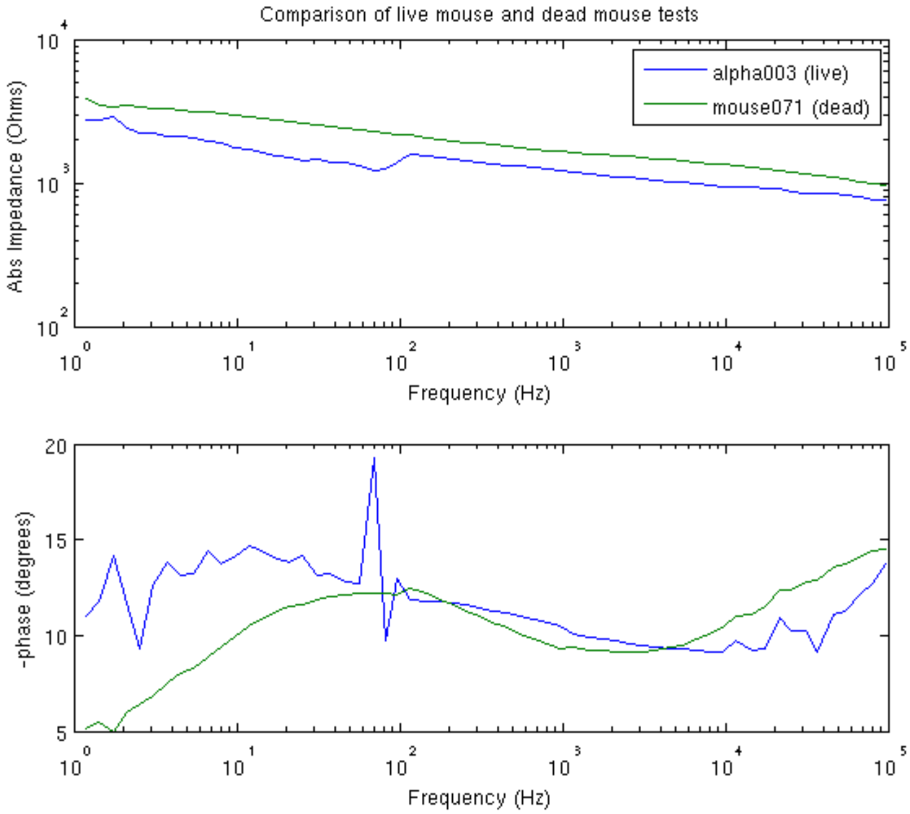

Figure 11: Comparison of Bode plots 1 day after implant in mouse 'alpha' and implants in deceased mouse

5 days after the procedure, the mouse was transported to Dr. Dong's lab for the second data measurement. Inspection of the mouse revealed that the wire connecting to the right hand side implant was missing. The mouse was observed to be able to bend all the way around and chew on this area of its back. It was concluded that the mouse chewed off the wire in response to irritation. On this day, significant gas buildup was observed in the mouse, suggesting either rapid corrosion. The gas buildup was concentrated on the RHS, with an easily deformable bulge unlikely to be inflammation. It was decided to keep the mouse alive to provide endpoint data on the corrosion of the implanted electrodes. The exposed wire on the left hand side of the mouse was trimmed as shortly as possible to avoid concern from the LAMS staff.

5 weeks after the implantation procedure, the electrodes were surgically removed from the mouse. The mouse was sacrificed by gas. An X-ray picture was taken of the mouse, blood was

removed from the body cavity, and the implants were removed as well as surrounding tissue. At this point, the right hand side electrode was located in the same location as the left hand side electrode. It appears that this electrode, without an exposed wire, was able to shift position subcutaneously. This may have been enabled by loose skin caused by the observed gas buildup. The excised local tissue was sent to Cincinnati Children's Hospital for histology by HE staining. No significant stiffness in the local tissue observed during dissection.

One of the two removed electrodes had approximately 3mm of exposed metal attached. The second had no visible wire exposed. The former, with the wire attached, was visibly more corroded, with no traces of the magnesium pellet visible. It is unlikely that the magnesium portion of this pellet simply became detached in the tissue, as the X-ray images only showed 1 pellet. The second electrode, while showing signs of corrosion and biofouling, was still intact. 2 potential causes for the variance in corrosion rates between the two electrodes were identified. First, the square shape of the one electrode might cause significant irritation to the surrounding tissue, yielding reduced tissue encapsulation and increased exposure to the environment, potentially increasing the corrosion rate. More likely, the electrode with exposed wire that was pulled into the conductive tissue formed a battery resulting in high corrosion rate. This was verified with in vitro experimentation conducted later and discussed in section 2.3.3.

The removed Mg samples were observed by EDAX. For comparison, Figure 13 provides EDAX data from a new Mg electrode. The identified elements are dominated by magnesium, as expected. Figure 15 shows the EDAX data from the Mg face of the heavily corroded electrode. As suspected, the magnesium appears to be completely corroded, and silver dominates the composition spectrum (recall that the wire was attached with a silver conductive epoxy). Figure 16 shows EDAX data from the back of the heavily corroded electrode. This sample shows signs of biofouling, with primary elements of carbon, oxygen, nitrogen, and calcium. Figure 18 shows EDAX data from the face of the other electrode, characterized by a high magnesium content and other elements characteristic of biofouling. Figure 20 - Figure 22 show the results from HE staining, with limited macrophage presence and visible debris from the electrodes.

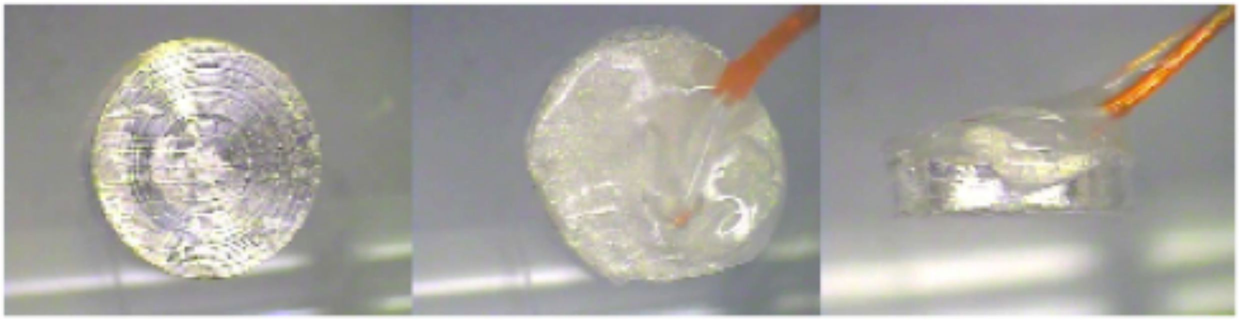

Figure 12: Images of new Mg electrode connected by magnet wire

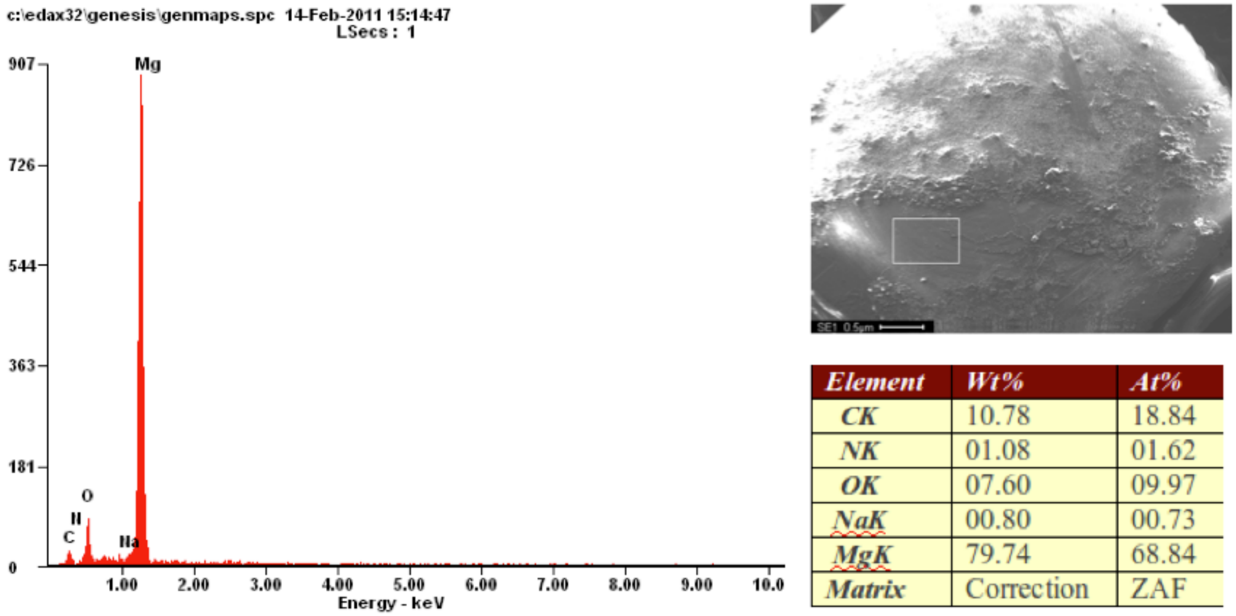

Element	*Wt%*	*At%*
CK	10.78	18.84
NK	01.08	01.62
OK	07.60	09.97
NaK	00.80	00.73
MgK	79.74	68.84
Matrix	Correction	ZAF

Figure 13: EDAX from Mg face of new Mg electrode

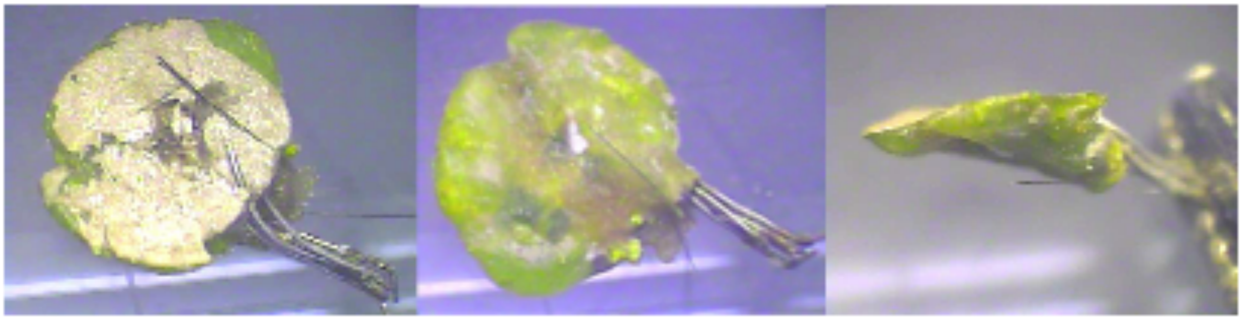

Figure 14: Electrode 1 removed from mouse 'alpha'

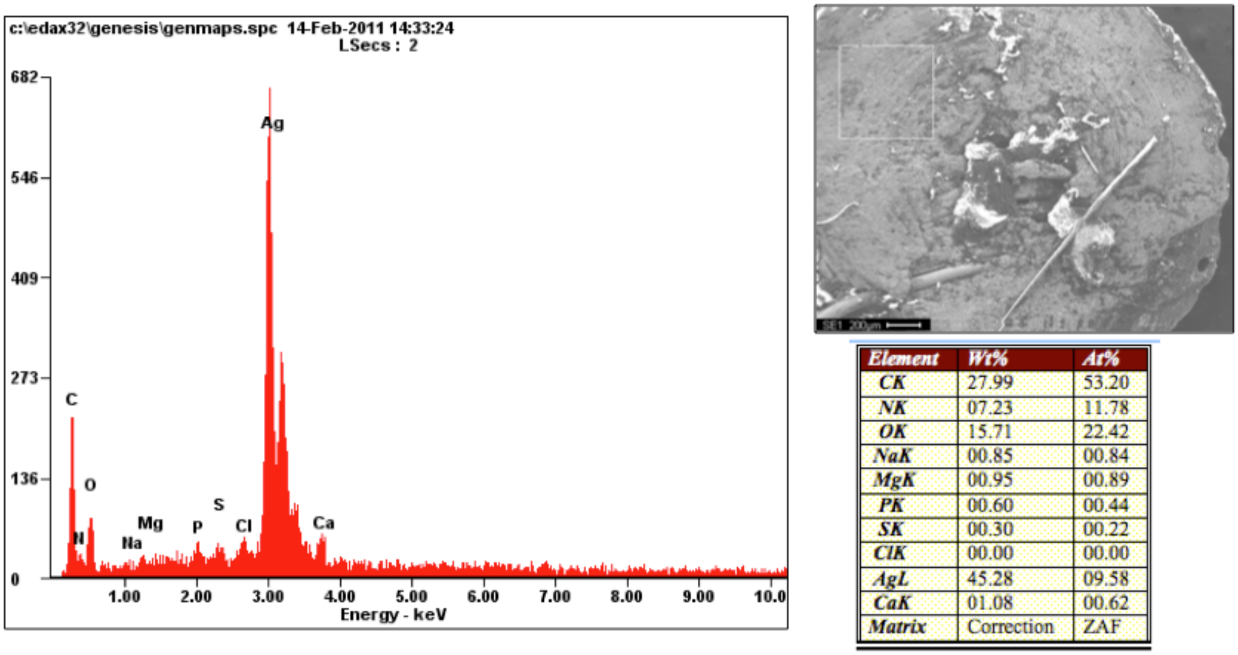

Element	Wt%	At%
CK	27.99	53.20
NK	07.23	11.78
OK	15.71	22.42
NaK	00.85	00.84
MgK	00.95	00.89
PK	00.60	00.44
SK	00.30	00.22
ClK	00.00	00.00
AgL	45.28	09.58
CaK	01.08	00.62
Matrix	Correction	ZAF

Figure 15: EDAX from face of Mg electrode 1

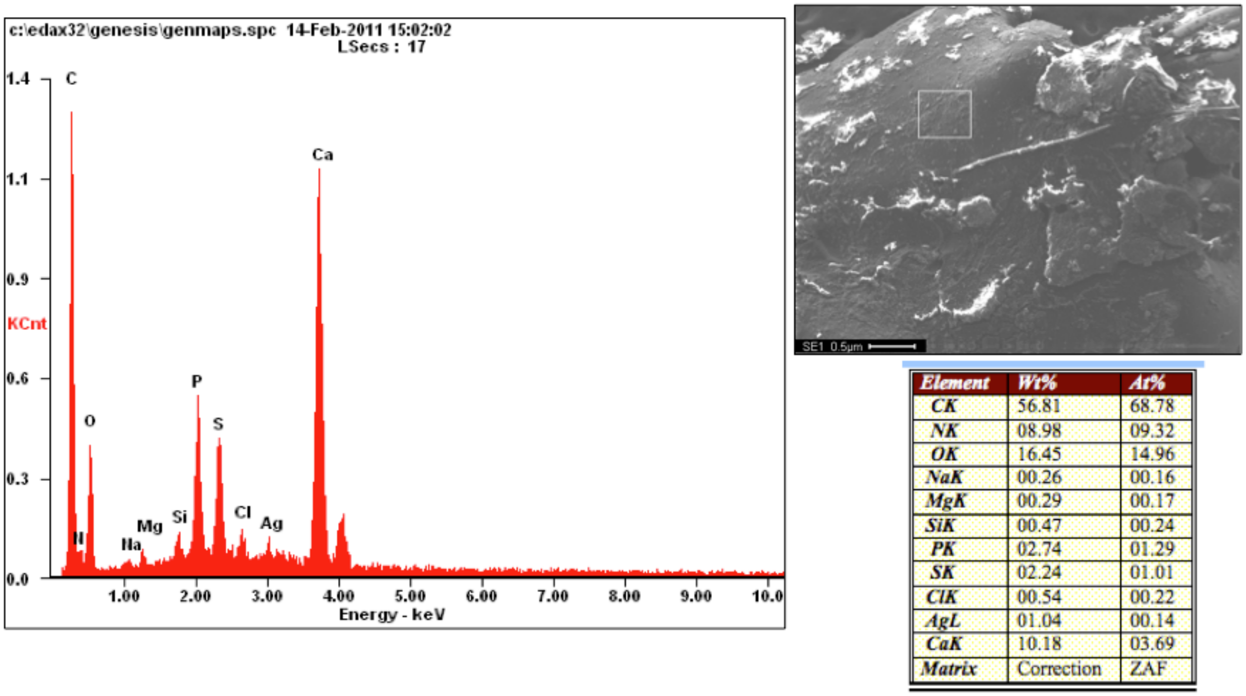

Element	*Wt%*	*At%*
CK	56.81	68.78
NK	08.98	09.32
OK	16.45	14.96
NaK	00.26	00.16
MgK	00.29	00.17
SiK	00.47	00.24
PK	02.74	01.29
SK	02.24	01.01
ClK	00.54	00.22
AgL	01.04	00.14
CaK	10.18	03.69
Matrix	Correction	ZAF

Figure 16: EDAX from epoxy on back of Mg electrode 1

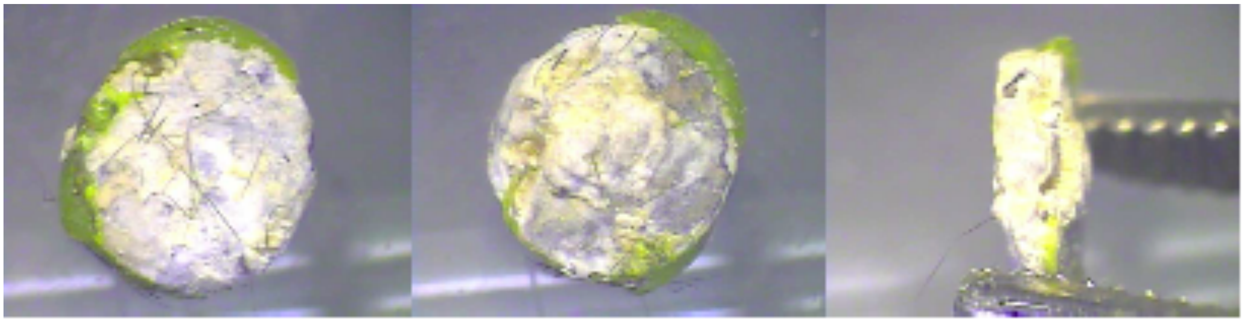

Figure 17: Electrode 2 removed from mouse 'alpha'

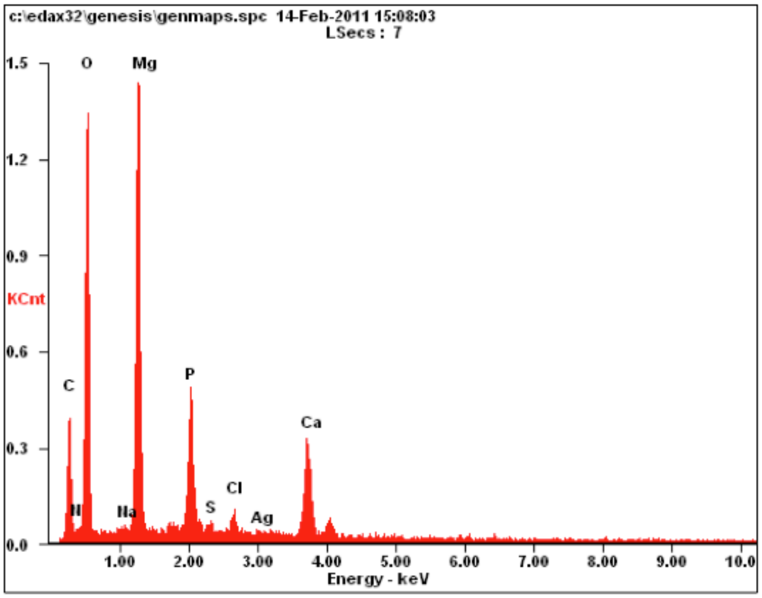

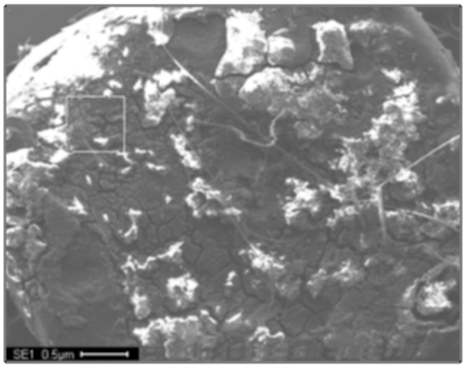

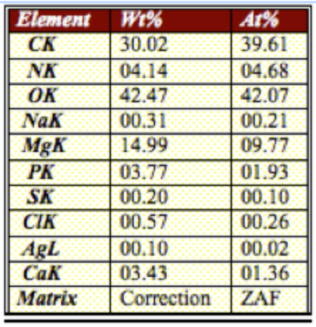

Element	Wt%	At%
CK	30.02	39.61
NK	04.14	04.68
OK	42.47	42.07
NaK	00.31	00.21
MgK	14.99	09.77
PK	03.77	01.93
SK	00.20	00.10
ClK	00.57	00.26
AgL	00.10	00.02
CaK	03.43	01.36
Matrix	Correction	ZAF

Figure 18: EDAX from Mg face of Mg electrode 2

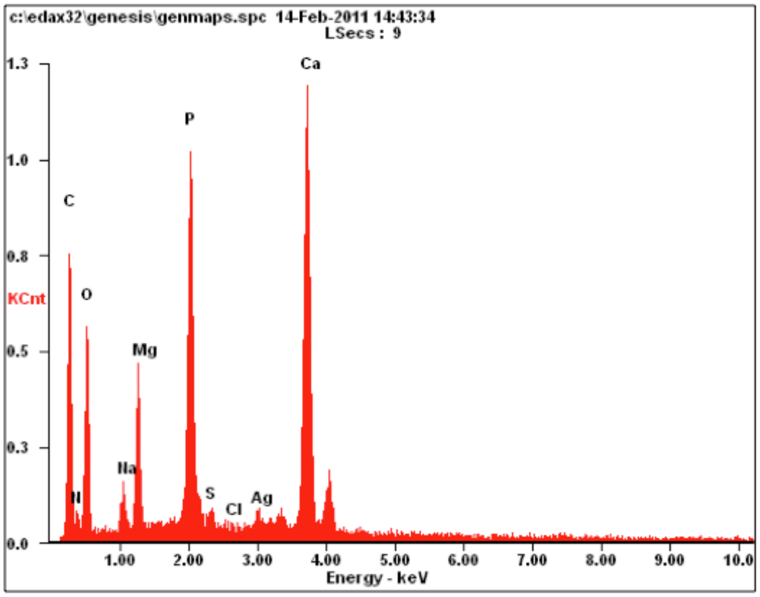

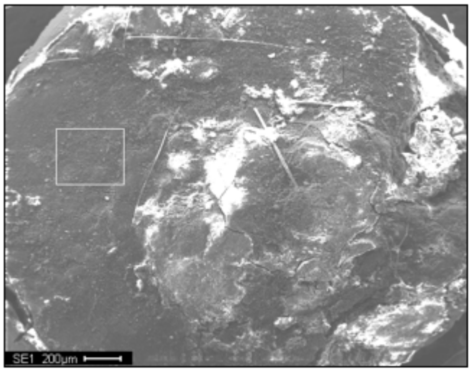

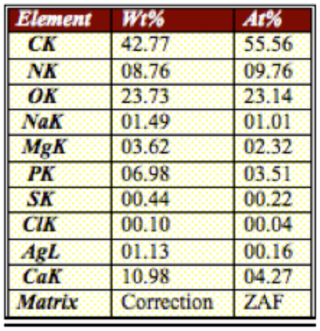

Element	Wt%	At%
CK	42.77	55.56
NK	08.76	09.76
OK	23.73	23.14
NaK	01.49	01.01
MgK	03.62	02.32
PK	06.98	03.51
SK	00.44	00.22
ClK	00.10	00.04
AgL	01.13	00.16
CaK	10.98	04.27
Matrix	Correction	ZAF

Figure 19: EDAX from epoxy on back of Mg electrode 2

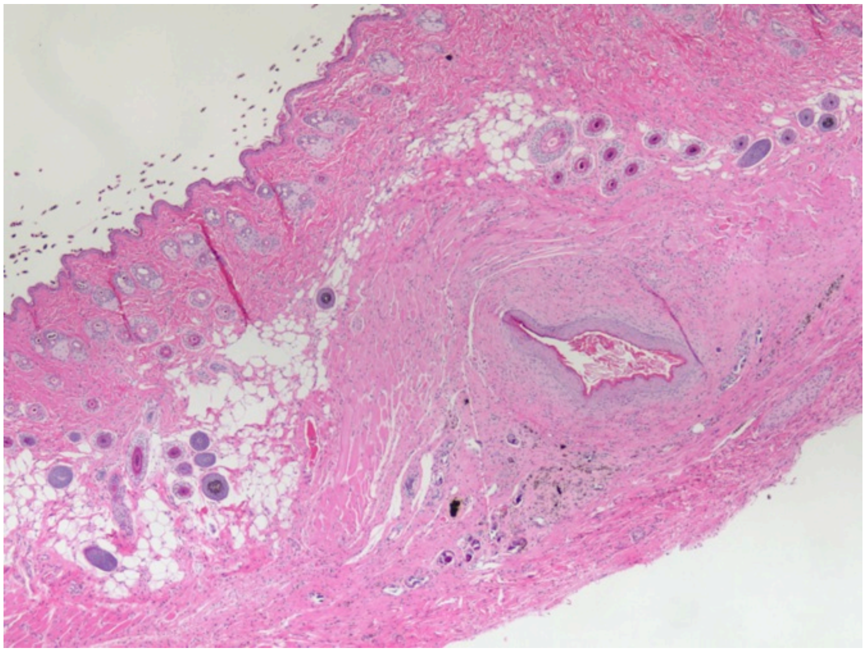

Figure 20: 4x optical image of HE staining from mouse 'alpha’

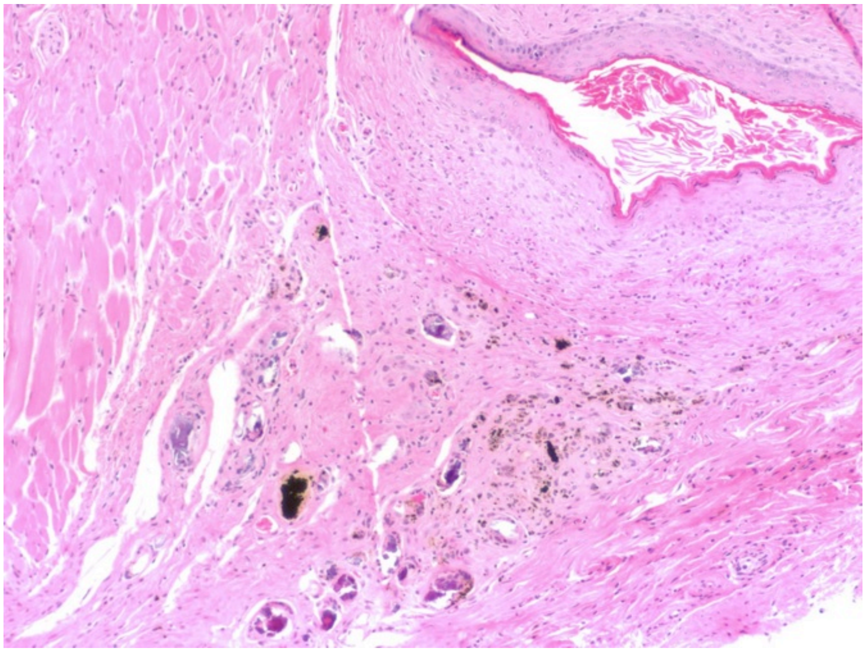

Figure 21: 10x optical image of HE staining from mouse 'alpha'

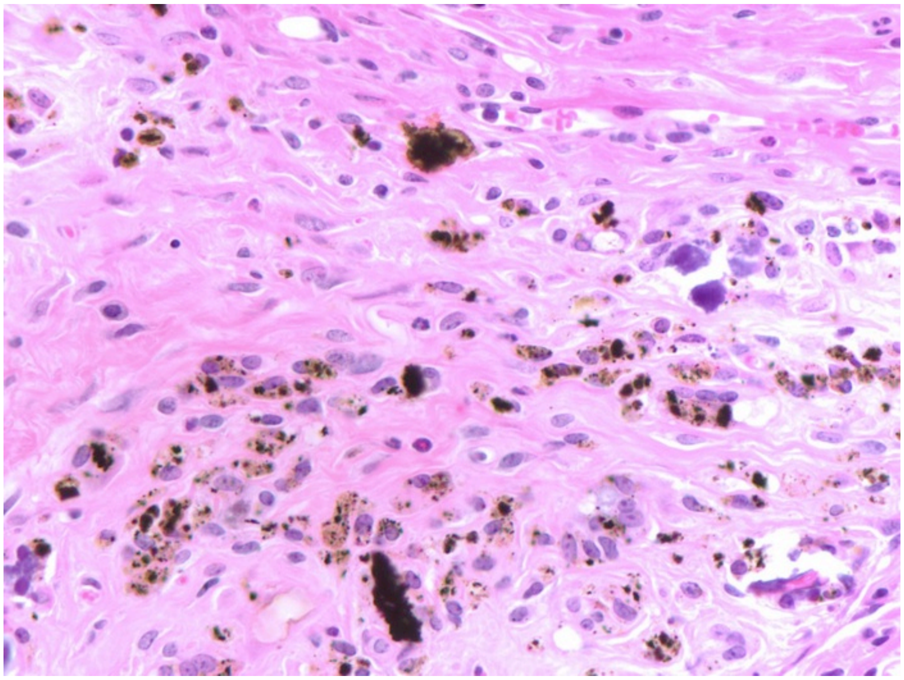

Figure 22: 40x optical microscope image showing loose magnesium debris and macrophage encapsulated debris

2.3.3. In vitro test on Mg pellet with exposed Cu wire

To verify if the large variance observed in the corrosion of the two electrodes implanted in mouse 'alpha' was caused by the formation of a battery between the exposed copper wire and the exposed Mg, an in vitro experiment was conducted in the lab. Several samples were prepared and submerged in a salt solution. Weight was monitored to observe corrosion rates. Set 1 consisted of 2 electrodes: a magnesium pellet with a copper wire attached (denoted electrode 1A), and a magnesium pellet with no wire (denoted 1B). Set 2 consisted of a magnesium pellet with a section of magnet wire attached (2A), and a bare magnesium pellet (2B). Electrode 2A was fabricated such that a small 2mm section of the magnet wire was uninsulated and attached to the magnesium pellet with conductive epoxy. This epoxy was coated with insulating epoxy in a fashion to ensure that no copper surfaces would be exposed to the solution. Set 3 consisted of just a magnesium pellet with a copper wire attached (3A). Set 4 consisted of 2 bare, identically sized magnesium pellets (4A and 4B). Set

5 consisted of a magnesium pellet with a layer of silver based conductive epoxy (5A) and a bare magnesium pellet (5B).

All sets were submerged in their own Pyrex beaker in a 0.85M NaCl solution. Attempts were made to maintain a separation between electrodes of 2 cm, however, these distances shifted slightly during the course of the experiment. Electrode 2A was suspended from the side of the beaker to ensure that the exposed copper end of the magnet wire (the end not attached to the magnesium pellet) would not be in contact with the solution. Immediate qualitative observations were made after initiating the experiment. Electrodes 1A, 3A, and 5A exhibited rapid bubbling. Each of these electrodes was composed of two unique metals (copper and magnesium for 1A and 3A, silver and magnesium for 5A). Electrode 2A displayed a small amount of bubbling.

The next day, after 19 hours of run time, the individual electrodes were massed to determine material loss due to corrosion. Before weighing, each electrode was dried on a KimWipe to eliminate solution mass and remove any loose oxide material from the surface. Unfortunately, the magnesium pellet separated from the epoxy and wire in samples 1A, 2A, and 3A. Furthermore, the Ag portion of electrode 5A was extremely fragile and flaked off from the magnesium pellet upon attempts to dry.

From our expectations prior to the experiment, we expected any sample that formed a small galvanic cell with two unique metals exposed to the solution to exhibit the highest corrosion rates. The observed data confirmed these expectations, with large weight losses for electrodes 1A and 3A (with exposed copper attached to the magnesium pellet). Because electrode 5A crumbled, no mass data was obtained. However the qualitative observations of rapid bubbling and significant deterioration of the electrode indicate that the corrosion rate was similarly high for this sample. This data provided supporting evidence that the source for the disparity in the corrosion rates in the two electrodes implanted in mouse 'alpha' was the formation of a galvanic cell by the exposure of a portion of the copper wire to the underlying tissue. This realization emphasized the importance of properly insulating the portion of the connecting wire that is exposed to tissue for this line of experimentation.

Table 1: Data from in vitro verification of source of corrosion in mouse 'alpha'

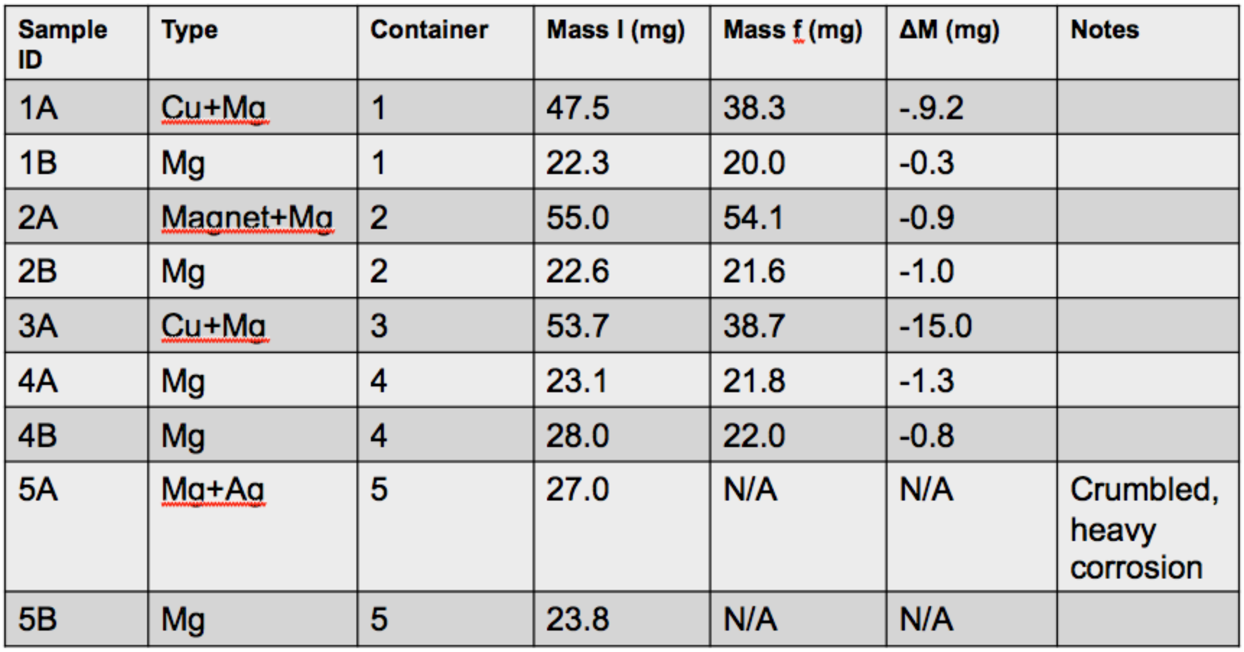

Sample ID	Type	Container	Mass I (mg)	Mass f (mg)	ΔM (mg)	Notes
1A	Cu+Mg	1	47.5	38.3	-.9.2	
1B	Mg	1	22.3	20.0	-0.3	
2A	Magnet+Mg	2	55.0	54.1	-0.9	
2B	Mg	2	22.6	21.6	-1.0	
3A	Cu+Mg	3	53.7	38.7	-15.0	
4A	Mg	4	23.1	21.8	-1.3	
4B	Mg	4	28.0	22.0	-0.8	
5A	Mg+Ag	5	27.0	N/A	N/A	Crumbled, heavy corrosion
5B	Mg	5	23.8	N/A	N/A	

2.3.4. Implants in mouse 'beta'

A new set of magnesium electrodes was implanted in a new black haired mouse, denoted mouse 'beta', in the Vontz center procedure room. Both electrodes had identical cylindrical geometries illustrated in Figure 24 and were electrically attached to magnet wire. The electrodes were inserted subcutaneously in the back of the mouse, moved significantly higher up on the shoulders to eliminate the possibility of the mouse chewing on the wires, as illustrated in Figure 23. The wires were cut by Zongqing Tan to approximately 1.5 cm. Staples were used once again to close the incision. Before the procedure, each electrode was weighed to facilitate comparison at the end of the experiment. The cut pieces of wire were collected and weighed to determine the final weight of the electrode and wire left in the mouse.

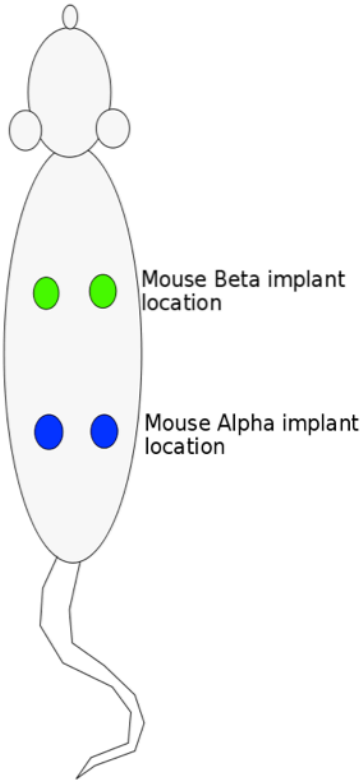

Figure 23: Modified implant location in mouse 'beta'

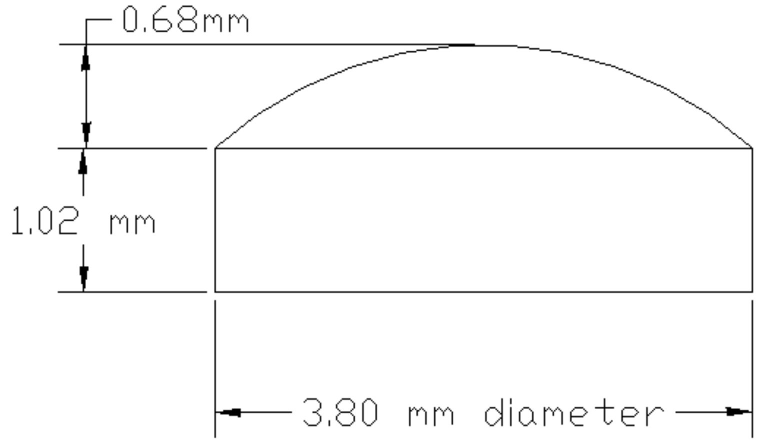

Figure 24: Dimensions of cylindrical Mg pellets with epoxy layer implanted in mouse 'beta'

Attempts were made to install the electrodes in this experiment in a fashion that would avoid interference caused by wire contact with the staples used to close the incision. Unfortunately, upon inspection on the following day, the wires still came into extremely close proximity to the staples. It was essential to trim the wires down to 5mm in response to concern by the animal facilities staff; an AHR was established after a vet tech observed the wire protruding from the mouse. As a result, it became very difficult to properly manipulate the exposed electrode wire to consistently avoid contact with the staples in mouse 'beta'. Despite this difficulty, with caution, a proper separation could be achieved for measurements. It was decided to proceed with this experiment and determine the significance of the interference caused by interaction with the staples by comparing readings after the removal of the staples. Staples are scheduled for removal 2 weeks after the procedure.

EIS measurements were taken in the same fashion as mouse 'alpha' by immobilizing the mouse in a modified plastic vial and attaching the appropriate alligator clips. Figure 25 plots the initial EIS measurements taken on the dead mouse, mouse 'alpha', and mouse 'beta'. Despite variance in the implant geometry, implant location, and implant specimen, the data is remarkably similar. A consistent variation in the magnitude of the impedance is observed, likely attributable to variation in implant separation. The phase plots show shifts in location of relative minima and maxima, but both show consistent low phase angles with values typically less than -15 degrees, demonstrating a dominantly resistive system.

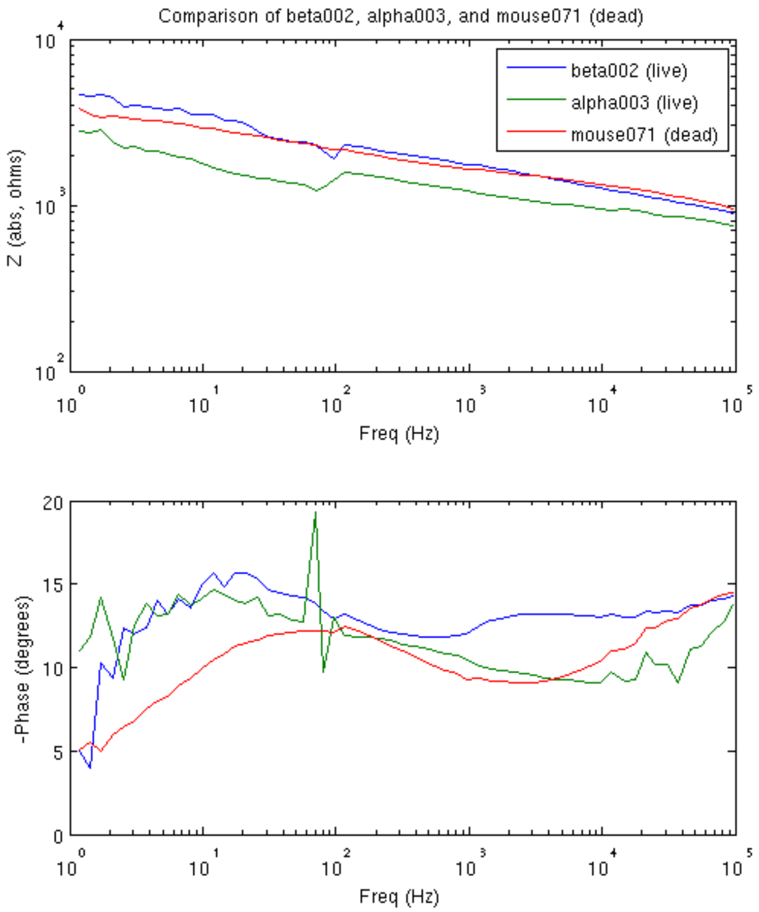

Figure 25: Initial EIS measurements taken on dead mouse (red), mouse 'alpha' (green), and mouse 'beta' (blue)

Data is taken every 2 to 3 days from mouse ‘beta’. Figure 26 plots the EIS data from days 1 through 11. The phase behavior immediately starts displaying increased capacitive properties at lower frequencies, associated with an increase in the magnitude of the impedance in the same frequency range. Observing the phase diagram in greater detail, the relative maxima observed on day 1 at approximately 20 Hz appears to become a knee at approximately the same frequency on

Day 3. As time progresses, this knee is shifted to lower frequencies, becoming a potential quantitatively relevant variable. It is likely that measurements with increased frequency range will be required to use this criteria. Analysis of the impedance magnitude shows remarkably consistent behavior over time, as the magnitude is reliably shifted higher between each measurement. At this point, the sources for the change in the impedance spectrum were believed to be biofouling, changes in local tissue, or corrosion. However, previous in vivo experiments conducted without EIS found that pure magnesium corroded very little when implanted subcutaneously. As such, it is likely that a biological response in the local tissue is the dominant source of the impedance shift, as rigid tissue forms around the electrode to protect the surrounding tissue and inflammation occurs in response to tissue injury.

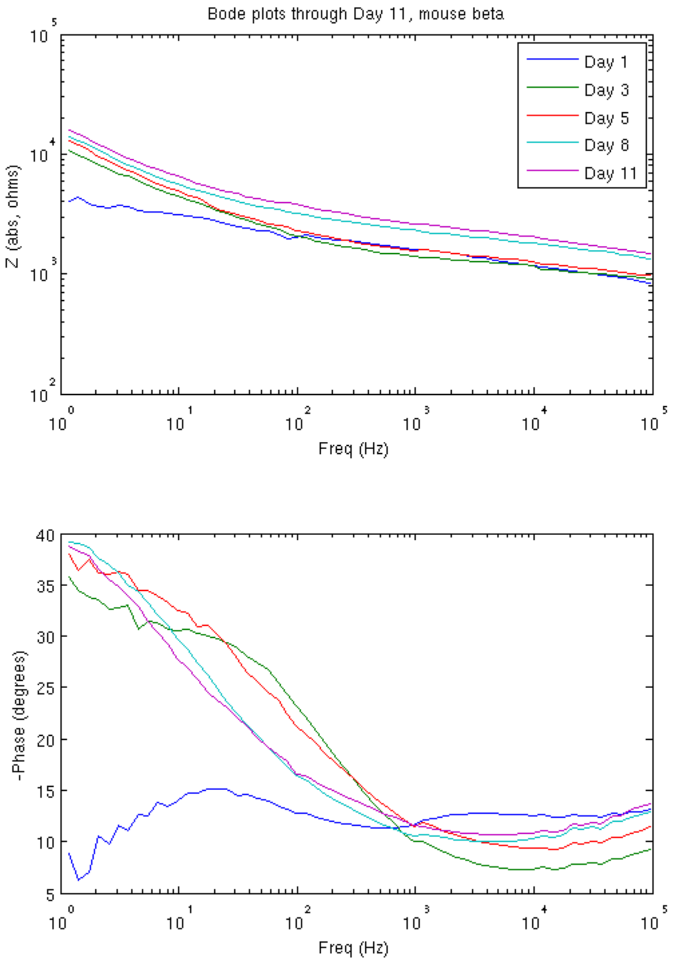

Figure 26: Bode plots for days 1-11 for mouse 'beta'

On Day 14, Tan removed the surgical staples per standard procedures. Subsequent EIS measurement contained a surprising shift in the data, illustrated in Figure 27. In particular, the phase dropped to consistent low values less than 20 degrees at low frequency, and the magnitude of the impedance dropped significantly, particularly at low frequency. This EIS behavior is very similar to what was observed on Day 1 for all experiments, as shown in Figure 28.

The immediate response to this sudden change is the speculation that the presence of the staples was significantly affecting the measured impedance spectrum. Considering the details of the experiment in greater detail, however, led to a different conclusion. Recall that there were instances that it was extremely difficult to ensure that the exposed magnet wire did not come into electrical contact with the surgical staples, which are highly conductive. The author is confident that the back of the electrode and subcutaneous portion of the magnet wire was adequately insulated that it would be unable to come into conductive contact with the staple. Furthermore, in most trials, it was possible to collect data while ensuring that the portion of the magnet wire outside of the mouse did not come into contact with the staples. Next, the location of the staples did not appear to be applying a shield in between the current path of the two electrodes. Finally, if the electrodes were in electrical contact with the staples, one would expect this to effectively increase the surface area of the electrodes and reduce the magnitude of the observed impedance. Because the magnitude of the observed impedance dropped significantly with the removal of the staples, the author is reasonably confident that the absence of the staples did not directly cause the sudden change in the impedance.

If the source of the change in impedance spectrum was corrosion, one would expect this to be a generally irreversible process. However, if the source was biofouling or acute inflammation, the detachment of the electrode from the surrounding tissue and subsequent contact with injured tissue would conceivably cause the observed impedance spectra to revert to what was observed immediately after the implant procedure. Injured tissue is likely to have a higher concentration of blood resulting in a significantly modified impedance spectrum. Because of the significant amounts of strain and pulling that are applied to the skin near the implant location during the removal of the surgical staples, it is highly likely that the electrodes were forcibly detached from their position during the process of the staple removal, reinjuring the local tissue. If this is the case, one would expect the evolution of the impedance spectra to behave in a similar fashion to that in the first 10 days of the experiment for measurements taken after staple removal.

Figure 29 shows the measured EIS data from days 14 through 21, and Figure 30 shows the measure EIS data from days 14 through 33. Through day 29, the EIS data evolved very similarly as what was observed between Day 1 and Day 11. If the assumption that the primary source of the change in the impedance spectrum is biofouling and other biological responses, it would make sense that the local tissue was forming a new protective barrier around the implanted electrodes and undergoing acute inflammation once again. On Day 33, both the Gamry and CH potentiostats were used to collect data from the mouse. A pair of Gamry experiments were taken first, over a period of approximately 30 minutes. Generally, the mouse would resist it's immobilized position more and more during the period of an experiment. This resistance was independent of whether or not the potentiostat was connected, evidence that any applied current was not causing discomfort resulting in the observed resistance. Compared to the typical trial times of 5-10 minutes when measuring with the CH potentiostat, the mouse resisted it's immobilization for an extended period of time, applying significant strain to the tissue surrounding the implanted locations. By the time data was collected with the CH potentiostat, the EIS data took the same form as observed on days 1 and 14, with the sudden drop in magnitude of impedance in low frequency and consistent low phase throughout the measured frequency range.

Figure 31 plots the EIS data collected on Day 33 with the Gamry potentiostat. The phase behavior matches what was observed with the CH potentiostat through Day 29, with phase angle approaching -30 degrees at 1Hz. The Gamry collected more stable data than the CH through 0.1 Hz. The Gamry was also able to collect data though .01 Hz, but showed some instability in this range due to the long times required to make a measurement combined with the resistance of the mouse in the immobilization tube. The Gamry takes significantly longer than the CH to take a measurement (approximately 5 minutes for 0.1 Hz to 100kHz). Nevertheless, the increased quality and range of the data warrants the replacement of the CH potentiostat with the Gamry if possible.

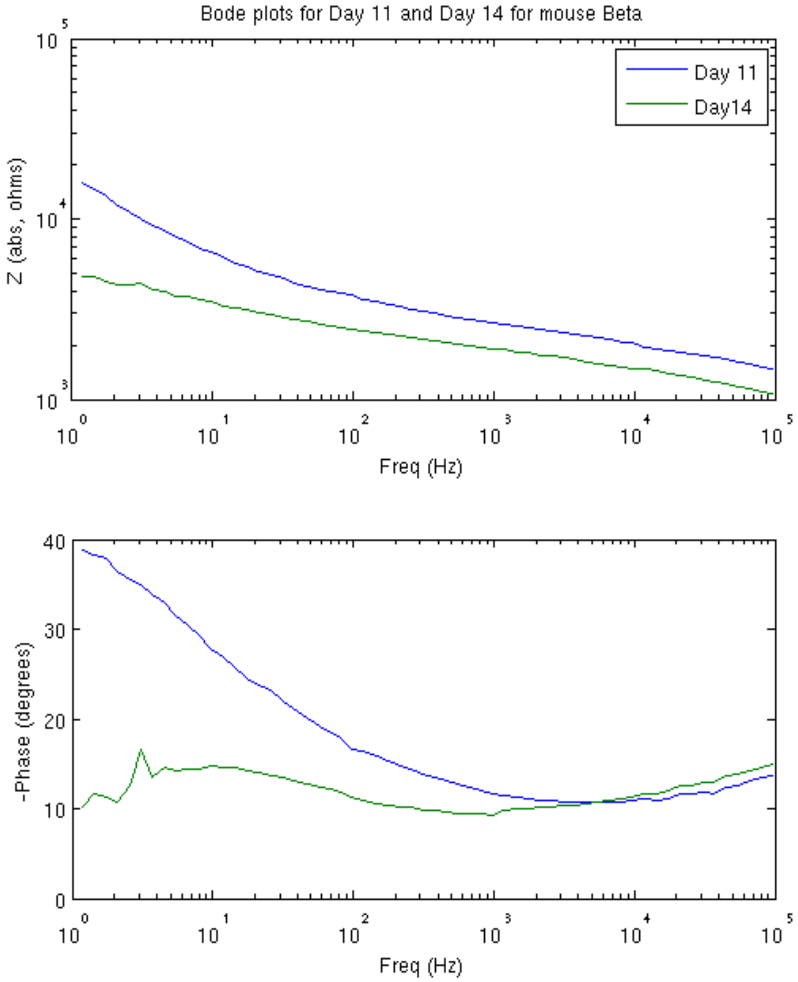

Figure 27: Bode plots comparing day 11 and day 14 for mouse 'beta'

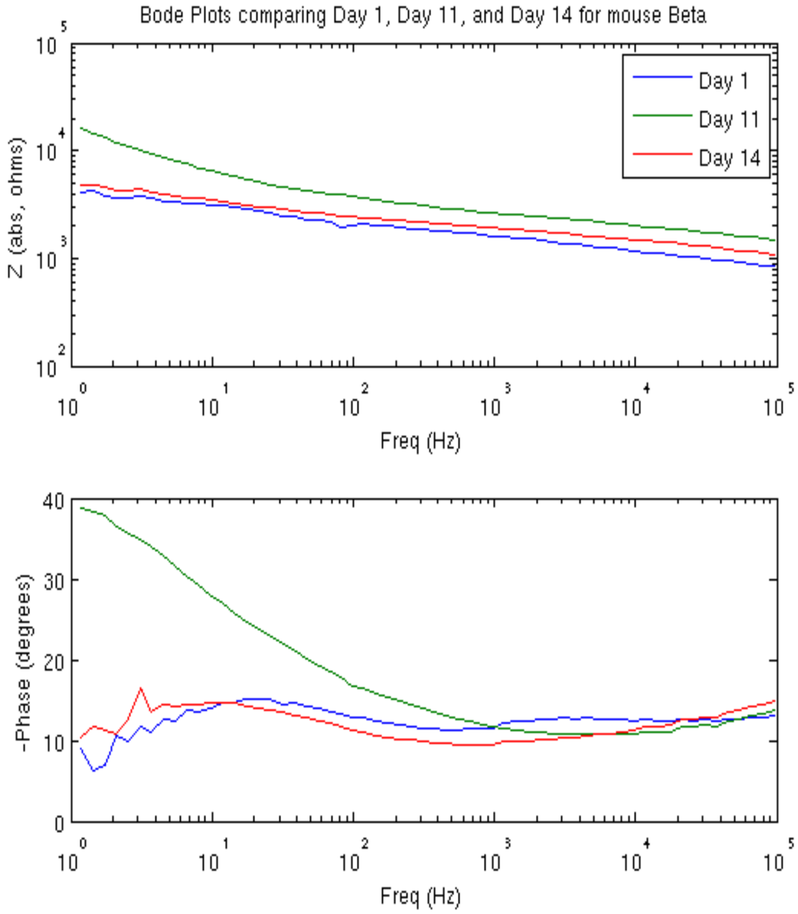

Figure 28: Bode plots showing similarity between day 1 and day 14 for mouse 'beta'

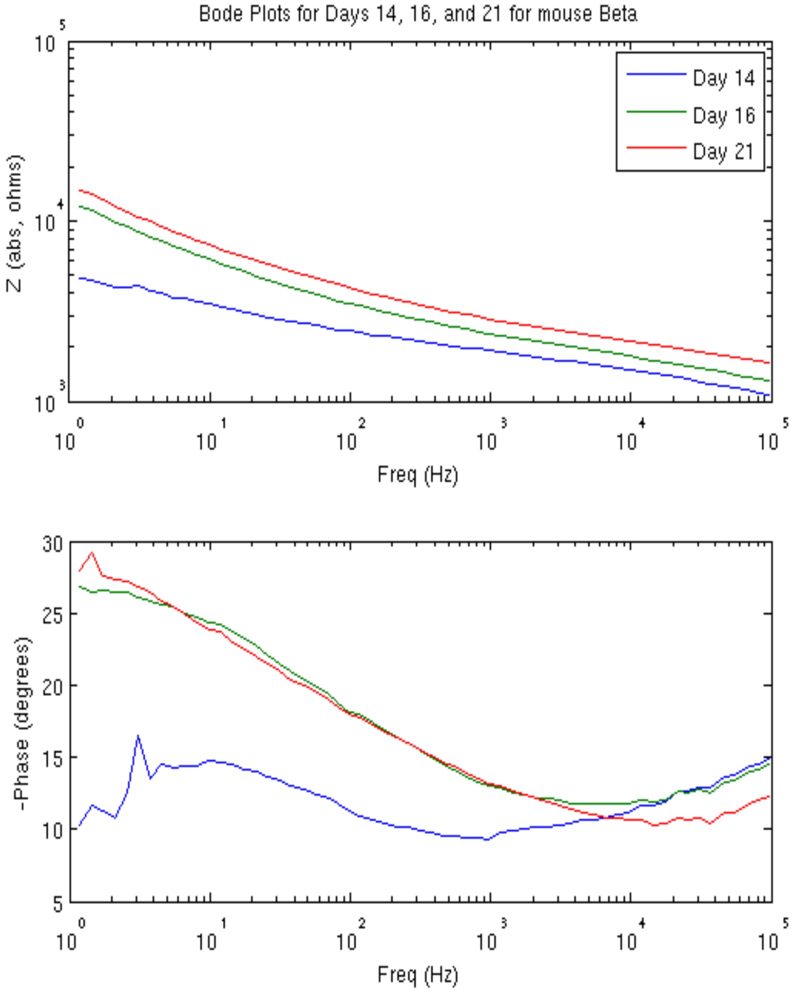

Figure 29: Bode plots for days 14, 16, and 21 for mouse 'beta'

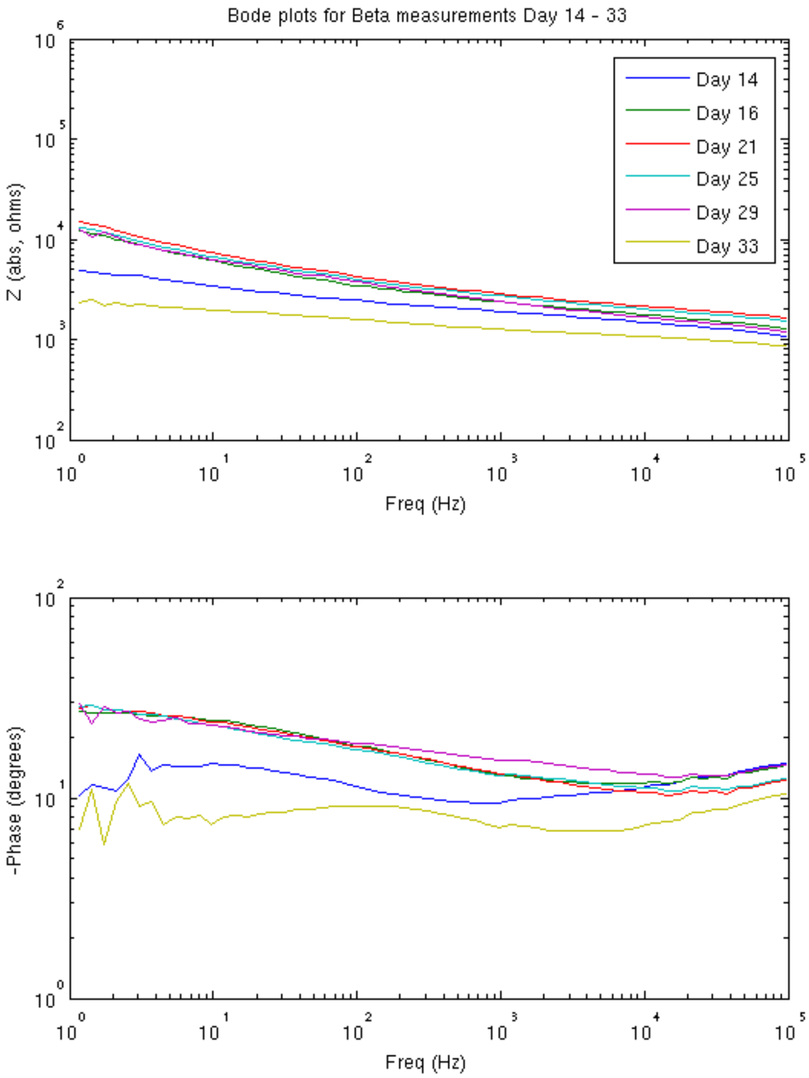

Figure 30: Bode plots for days 14-33 for mouse 'beta'

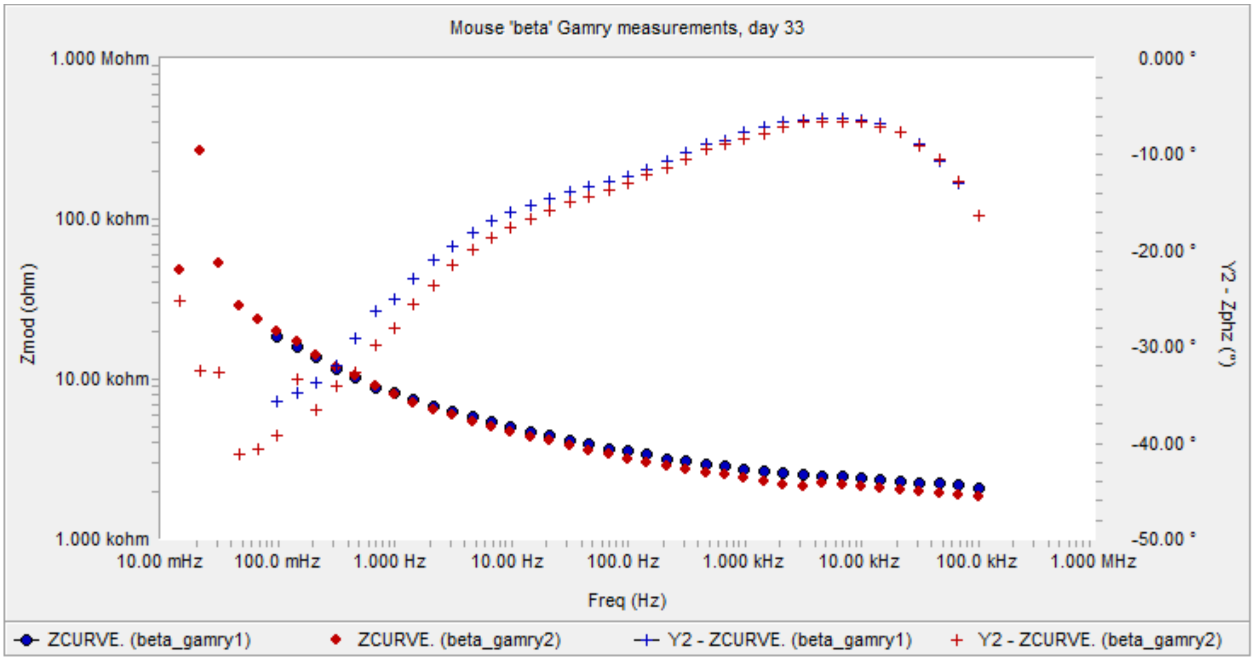

Figure 31: Bode plots for mouse 'beta' on day 33

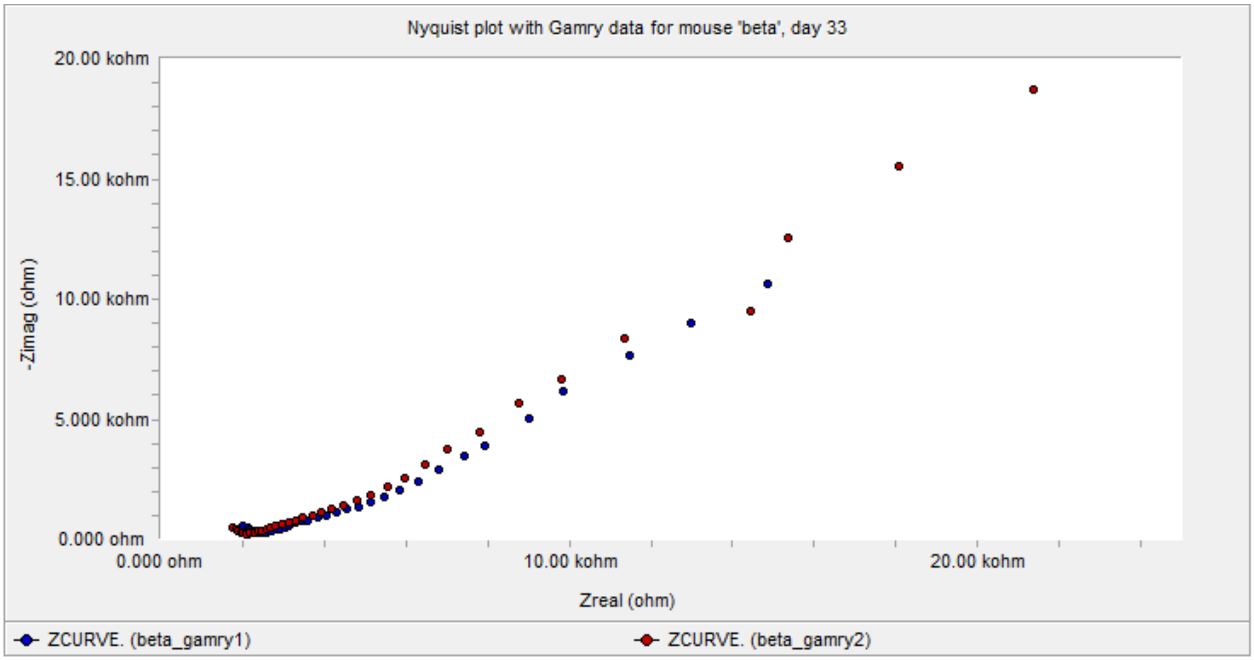

Figure 32: Nyquist plot for pair of EIS scans taken on mouse 'beta' on day 33

After the sacrifice of the mouse, the electrodes were removed and weighed to determine weight loss from the beginning of the experiment. There were noticeable quantities of biofouling present on the electrodes that could not be removed without damaging the electrodes. As a result, the calculated weight loss is most likely less than the actual weight loss. EDAX, SEM, and HE staining were conducted on these electrodes.

Table 2: Mass comparison after removal of electrodes from mouse 'beta'

Electrode	Initial (mg)	Final (mg)	Weight Loss (mg)
1	27.1	23.1	4.0
2	30.6	25.6	5.0

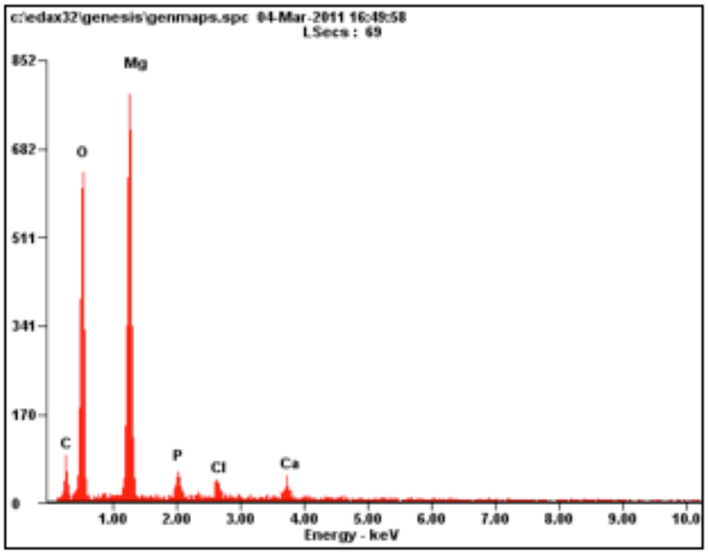

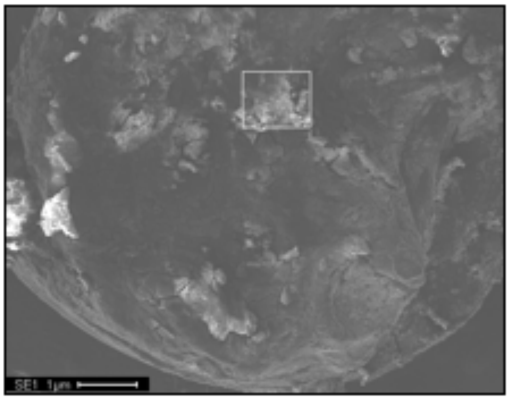

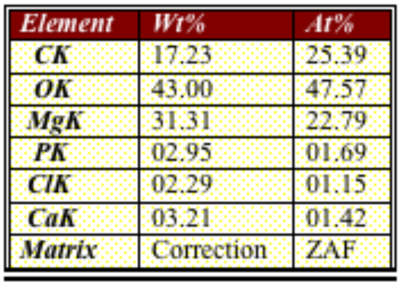

Element	Wt%	At%
CK	17.23	25.39
OK	43.00	47.57
MgK	31.31	22.79
PK	02.95	01.69
ClK	02.29	01.15
CaK	03.21	01.42
Matrix	Correction	ZAF

Figure 33: EDAX from left electrode from mouse 'beta'

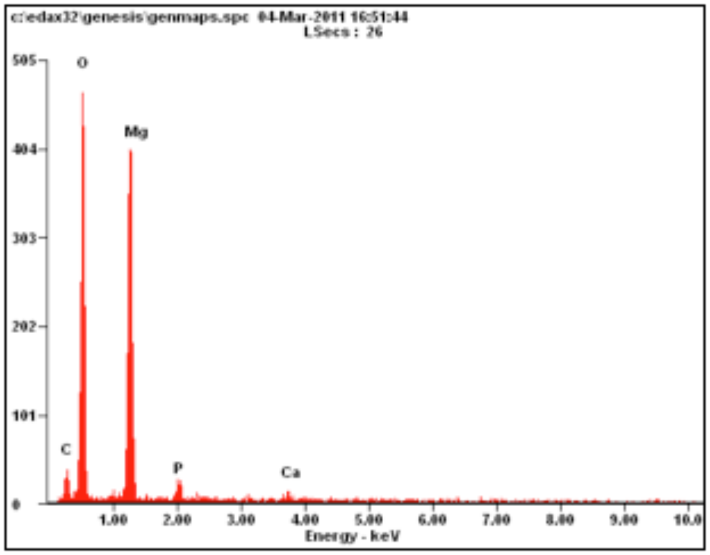

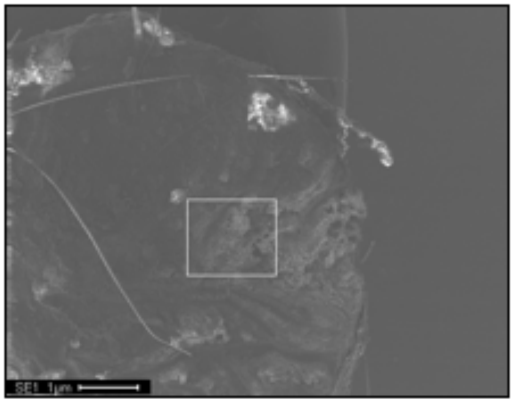

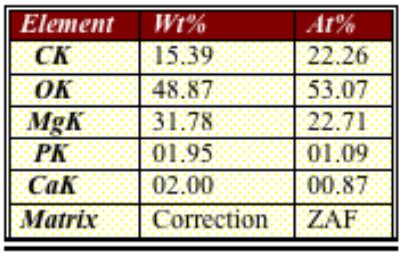

Element	Wt%	At%
CK	15.39	22.26
OK	48.87	53.07
MgK	31.78	22.71
PK	01.95	01.09
CaK	02.00	00.87
Matrix	Correction	ZAF

Figure 34: EDAX spectrum from right electrode from mouse 'beta'

2.3.5. Graphite electrode characterization

For future in vivo experiments, a different counter electrode was selected to model conventional EIS corrosion monitoring in which only the working electrode was magnesium. Graphite was selected for the new electrode because it is cheap, stable, and easy to fabricate. The fabrication process for this electrode was identical to that for the magnesium electrode, except that a shop-vac was mounted near the cutting tool on the lathe to minimize harmful inhalation of graphite particulates. After observing the premature detachment of samples from the epoxy in previous experiments, wires were attached to the newest set of electrodes using Buehler Epo-kwik at the recommendation of other lab members. Before curing, this epoxy exhibited lower viscosity, making application to the electrode more difficult.

To verify that the graphite electrode was a suitable counter-electrode, a quick in vitro experiment was conducted. Two potentiostatic electrochemical impedance spectroscopy scans were taken with the Gamry in 0.85 M NaCl. Both scans used the same magnesium working electrode and Ag/AgCl reference electrode. The first scan used a platinum counter electrode, and the second scan used a graphite counter electrode. Exposed counter electrode surface area and separation between electrodes differed in the two scans. Nevertheless, resultant impedance profiles were very similar in shape and magnitude, as shown in Figure 35, justifying the suitability of graphite as a counter electrode.

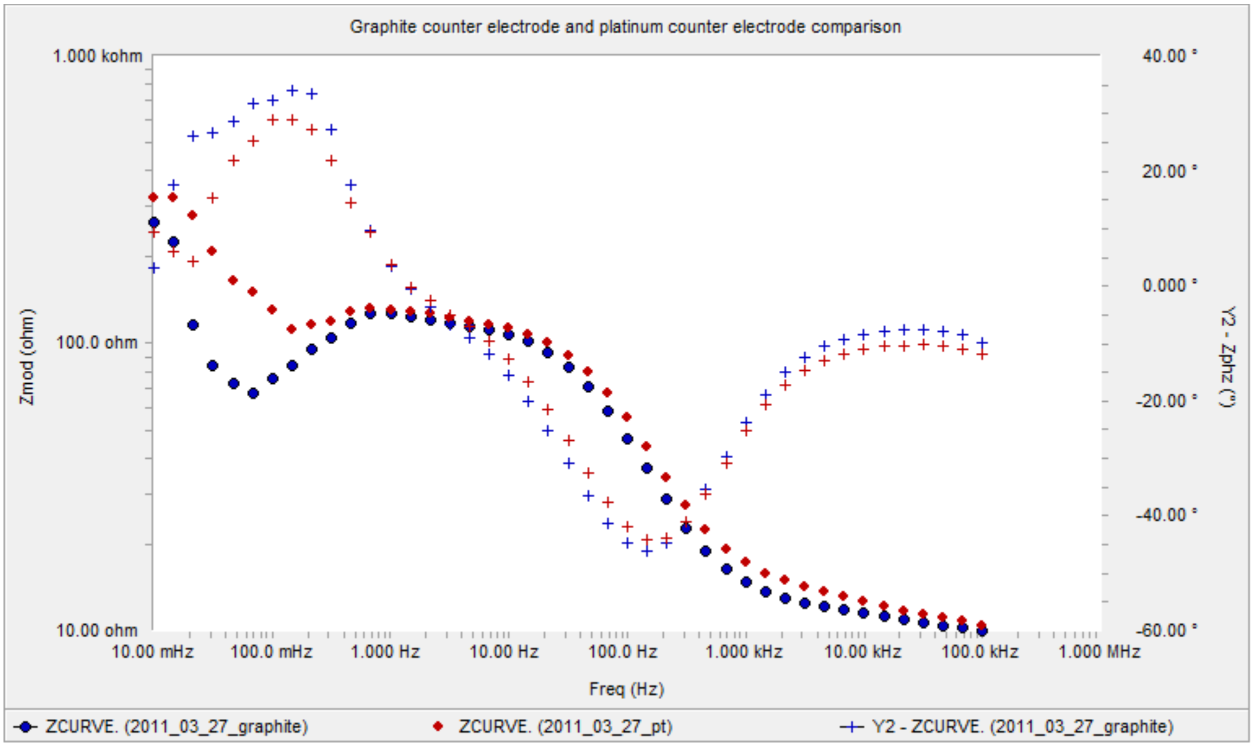

Figure 35: Comparison of graphite and platinum counter electrodes

2.3.6. Implants in mouse 'gamma'

PVC coated CNT thread was used for the connecting wire for the electrodes for mouse 'gamma'. A 4-ply sample produced on 03/24/2011 was used for this experiment. PVC was selectively removed from the thread by submersion in THF for 30 seconds. More detail regarding the characterization of the electrical and mechanical properties of this CNT thread can be found in Chapter 3. In summary, PVC coated thread is found to be a potential replacement for insulated wire when applying power to implanted electrodes. To ensure that the electrode wires would be visible and easy to connect to, small copper tabs with a diameter of approximately 2mm are attached to the exposed ends of each CNT wire.

The electrodes connected with CNT wire are implanted in mouse 'gamma' in the same subcutaneous location as mouse 'beta'. One electrode is graphite, and the other is magnesium. Extreme caution is executed in handling the electrodes, as the CNT thread is extremely susceptible to mechanical failure. Prior to implantation, the electrodes are rinsed in sterile HBSS and exposed to UV light for sterilization. Alcohol exposure is intentionally avoided due to the potential chemical effects on the PVC coated CNT thread.

The electrodes are implanted in a hairless mouse. Upon visual inspection 1 day after the implantation, only 1 copper connection point is remaining (on the right hand side of the mouse). The mouse demonstrated a high level of physical activity in the cage, which likely caused the left hand side copper connection point to get caught and detach at some point during the preceding day. Nevertheless, close inspection revealed that a small section of the CNT thread on the left hand side was still exposed and accessible to the copper alligator clips attached to the Gamry potentiostat. In fact, when implanted in hairless mice, the copper connection point is not necessary to make the CNT wire visible because of the contrast between the black wire and the pale skin of the mouse. The copper connection point is still useful for providing a reliable electrical connection.

Even when immobilized in a tube, the mice are still able to move enough to cause significant mechanical force on the electrodes. Because of the extreme fragility of the CNT thread, the mouse was knocked unconscious by injection with Nembutal prior to EIS measurement. The first potentiostatic scan (denoted gamma001) collected by the Gamry potentiostat showed inconsistent data of an excessively large magnitude. This indicated a poor connection to the system, most likely on the left hand side where the condition of the PVC insulation and the contact between the alligator clip and CNT thread was unknown. A second scan (denoted gamma002) was collected after reattaching the electrodes, exhibiting an extremely smooth EIS curve of a magnitude typical from other experiments. Datasets 'gamma001' and 'gamma002' are both plotted in Figure 36.

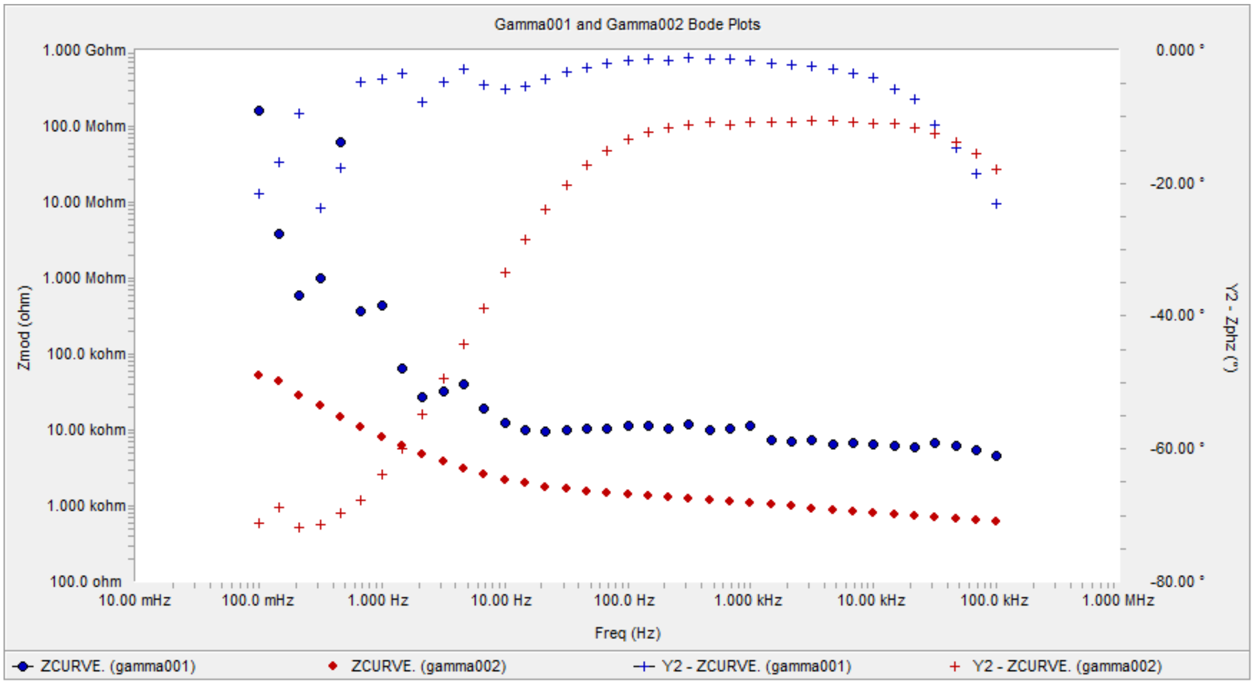

Figure 36: Two potentiostatic EIS scans, 'gamma001' in blue and 'gamma002' in red, taken with Gamry on mouse 'gamma' with CNT attached electrodes implanted

To demonstrate the validity of the data in 'gamry002,' Figure 37 plots both the this scan and the first set of data taken from mouse 'delta.' Mouse 'delta', to be discussed in the next section, has an identical set of electrodes but with copper magnet wire instead of CNT thread. The two sets of data show extremely similar properties, justifying the electrical properties of the CNT thread for use in this application. Figure 38 plots the Nyquist plots of the same two datasets. The CNT data shows lower impedance magnitude at low frequencies and similar impedance magnitude at high frequencies.

As the magnesium and graphite electrodes were fabricated to the same specs with the same exposed surface area, and the separations between implanted electrodes were very similar, the only significant source for the change in impedance is the resistance in the CNT wire itself and the potential for current leakage through the PVC coating. Leakage through the PVC coating will reduce the impedance magnitude, while the higher resistivity of CNT thread will increase it. The higher observed impedance in the CNT attached samples at high frequencies is likely due to the increased resistivity of the CNT thread, which prior characterization showed to be dominantly resistive. Figure 39 shows an electrical model for the CNT connected electrode in tissue. The branch on the right shows the complex impedance of the tissue with the additional resistive contribution of the CNT thread (Chapter 3 characterized the electrical properties of the thread alone). The branch on the left, in parallel with the former, shows the contribution of current that leaks though the PVC coating, and consists of a modified complex impedance of tissue, a reduced resistance contributed by the CNT thread (accounting for travel through only part of the CNT wire), and a capacitance contributed by the PVC coating.

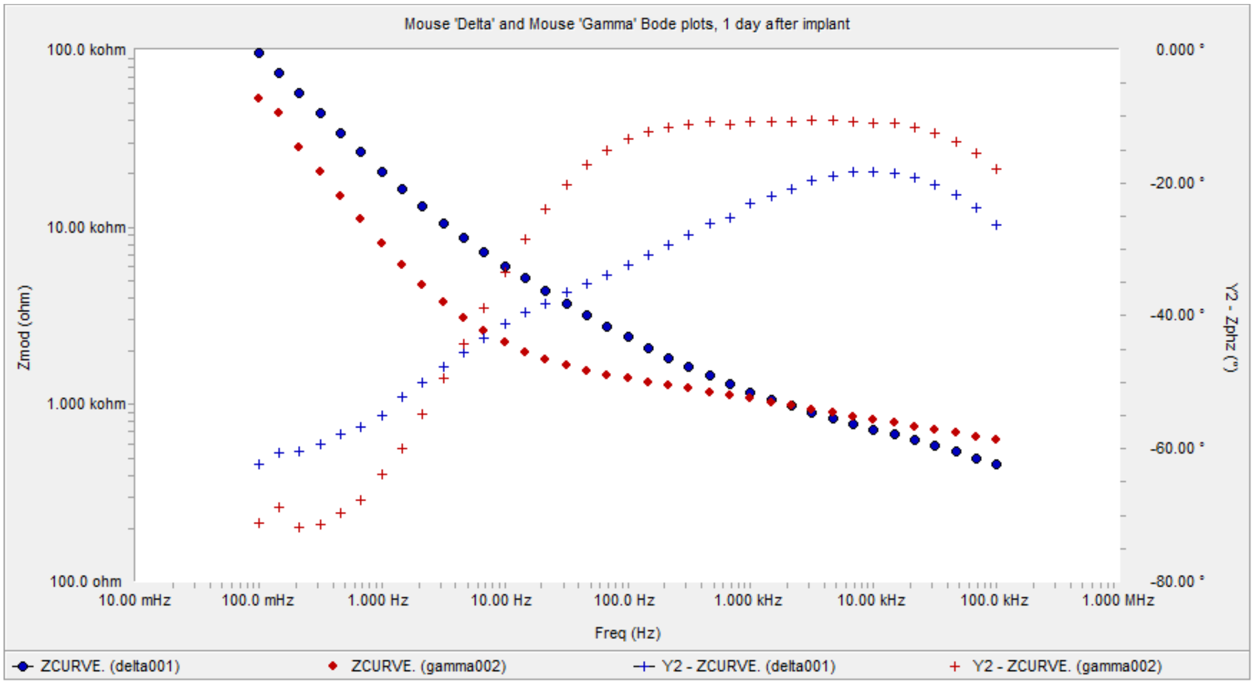

Figure 37: Bode plots from mouse with CNT attached electrodes (gamma002) and copper attached electrodes (delta001)

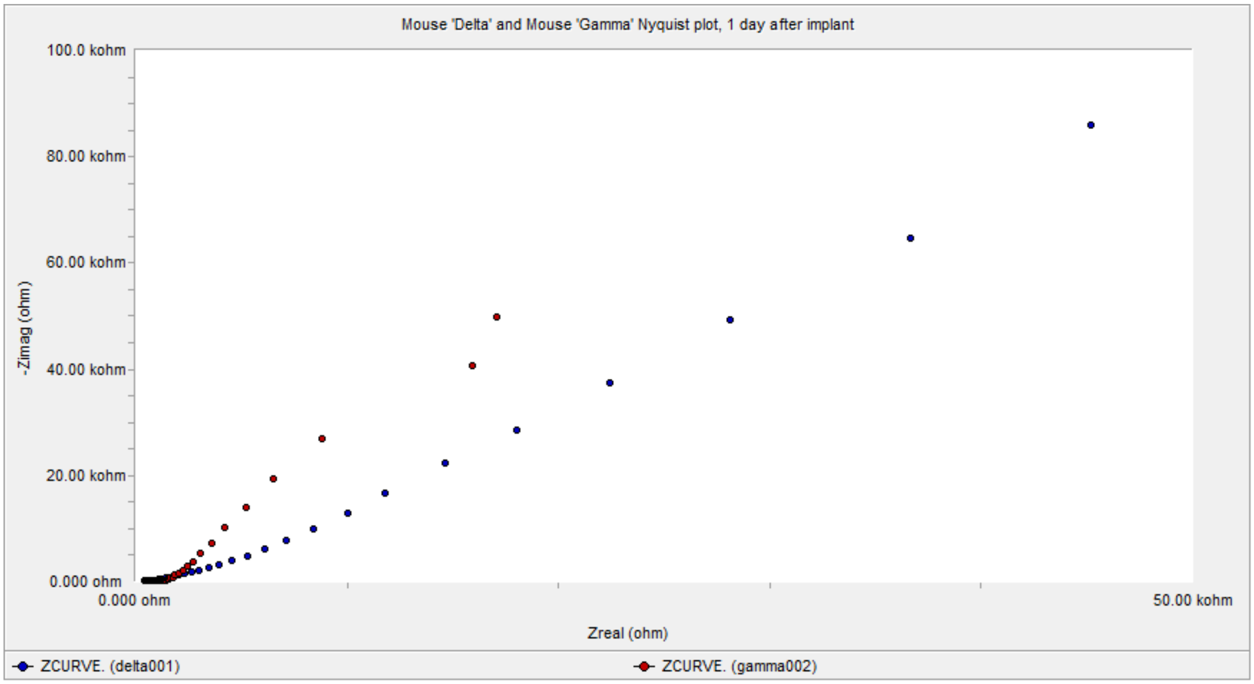

Figure 38: Nyquist plots from mouse with CNT attached electrodes (gamma002) and copper attached electrodes (delta001)

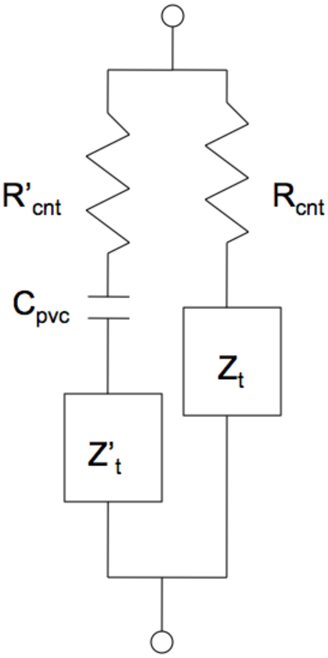

Figure 39: Electrical model for CNT connected magnesium electrode in tissue. Z_t represents complex impedance of tissue, R_{cnt} is resistance of CNT thread, C_{pvc} is capacitance of PVC coating, R'_{cnt} is partial impedance of CNT thread for current that leaks through PVC coating, and Z'_t is complex impedance of tissue for current that leaks through PVC coating.

Because of the extreme fragility of this system, only the first set of EIS data was collected from this mouse as a proof of concept experiment demonstrating the function of CNT thread in this role.

2.3.7. Implants in mouse 'delta'

The forth set of implants were implanted with the goal of maximizing the quality of data collected in comparison to that collected from mouse 'beta,' while working with the same basic system. Instead of using 2 magnesium electrodes, 1 graphite and 1 magnesium electrode are used. The electrodes are connected by magnet wire prepared in the same fashion as for mouse 'beta.' The second major change is that the Gamry potentiostat is used instead of the CH, which has been demonstrated to give higher quality data with less noise. To further improve data, the mouse is knocked unconscious by injection with Nembutal prior to each measurement. Nembutal is composed of pentobarbital sodium and is a barbiturate commonly used as an anesthetic in veterinary applications. During previous measurements where the mouse was immobilized in a tube, irregularities in data were commonly observed when the mouse would resist its immobilization in the modified vial, justifying the use of anesthesia.

Data collected was of high quality, and relevant Bode plots and Nyquist plots are shown in Figure 40 through Figure 43. The evolution of the EIS data over time, however, exhibited traits significantly different then any preceding trials. In particular, the phase 1 day after the implantation showed a significantly higher range of phase, with maximum magnitude of phase exceeding 60 degrees at low frequency. During previous trials, this range of phase wasn't observed for several days. Furthermore, the evolution of the magnitude was inconsistent. Between day 1 and day 3, the magnitude of impedance dropped significantly. It then increased for day 7, decreased for day 10, and increased again for day 13. This oscillation in magnitude could have been caused by shifting in the relative location of the electrodes, irregular inflammatory response, or some other influence not yet identified. The lack of steady buildup in magnitude previously associated with tissue formation may be a result in small difference in implant location or a different response to the implantation of graphite. Further trials will be conducted to understand this effect further.

Despite this odd behavior, another metric became evident. On day 1 the phase was relatively linear with respect to the log of the frequency between 10 and 1000 Hz. As time progressed, a curvature in this region developed, becoming more distinct with every trial. The source of this evolution has not been identified as corrosion or biological, and further experimentation will be conducted. However, the observation of easily trackable evolution in the data is critical for the application of this process in in vivo corrosion monitoring.

Before sacrificing this mouse, a DC potential was applied between the two electrodes in a proof of concept for in vivo cathodic protection. More of this experiment is discussed in Chapter 4.

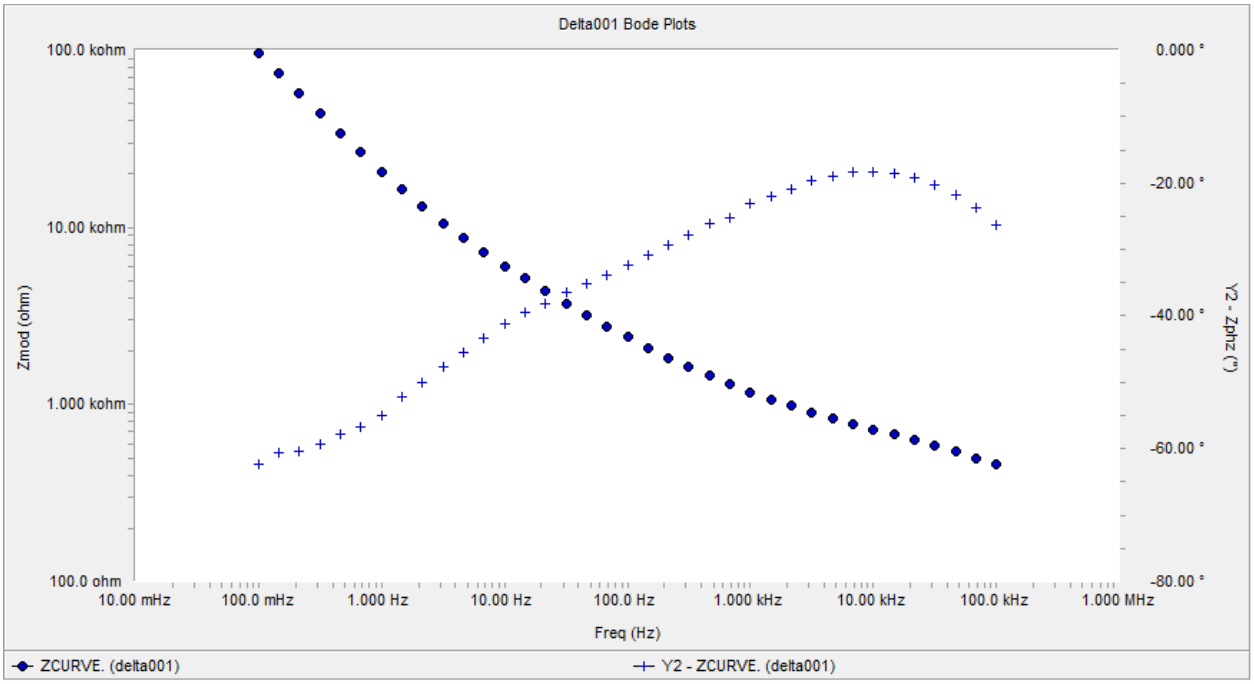

Figure 40: Bode plots for trial 'Delta001' taken 1 day after implant procedure

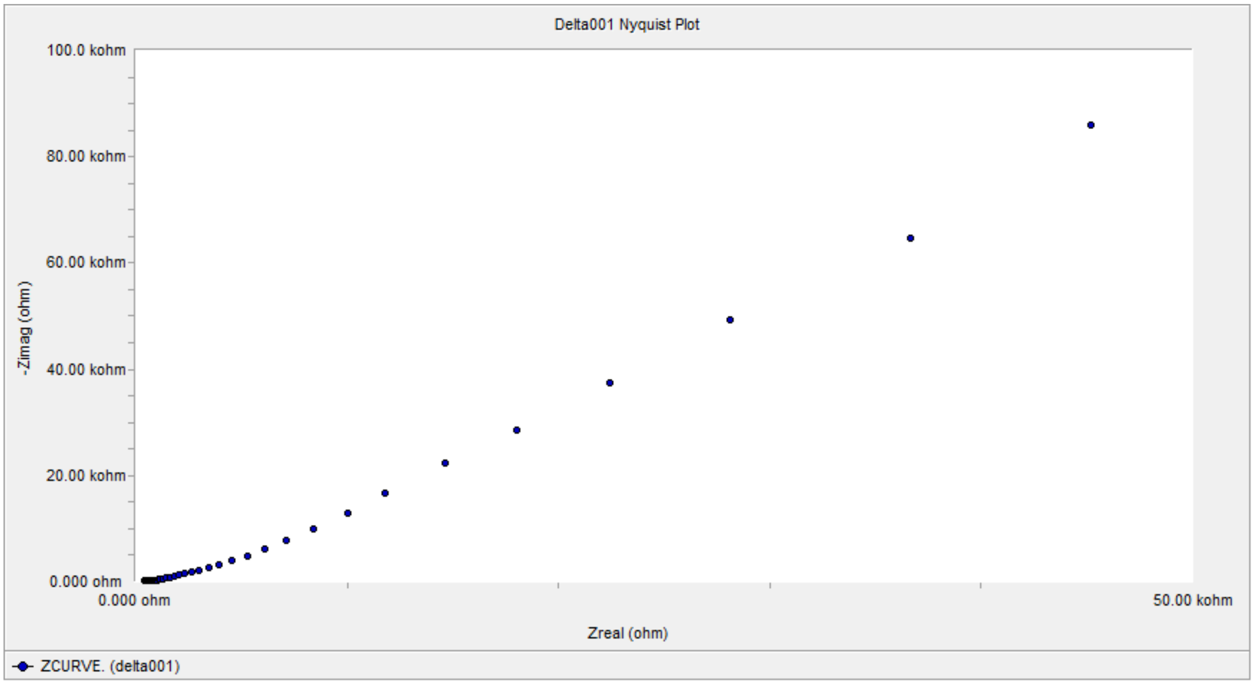

Figure 41: Nyquist plot for tiral 'Delta001' taken 1 day after implant procedure

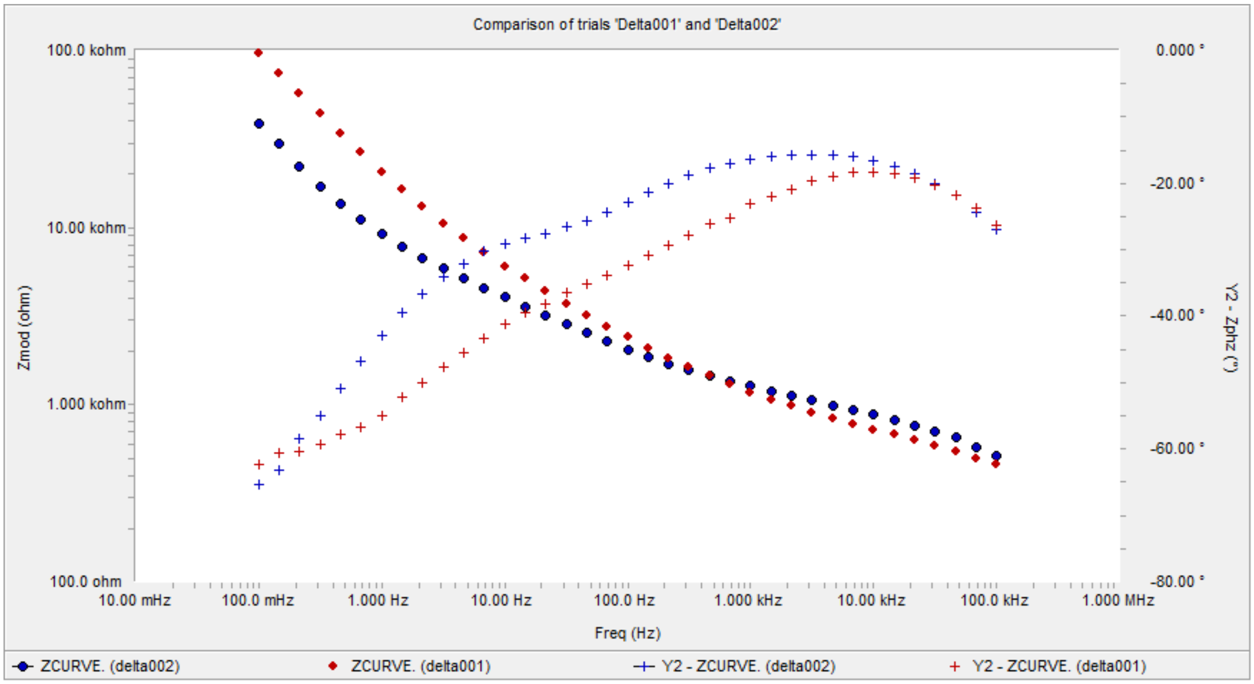

Figure 42: Comparison of Bode plots for trials 'Delta001' and 'Delta002' taken 1 and 3 days after implant procedure, respectively

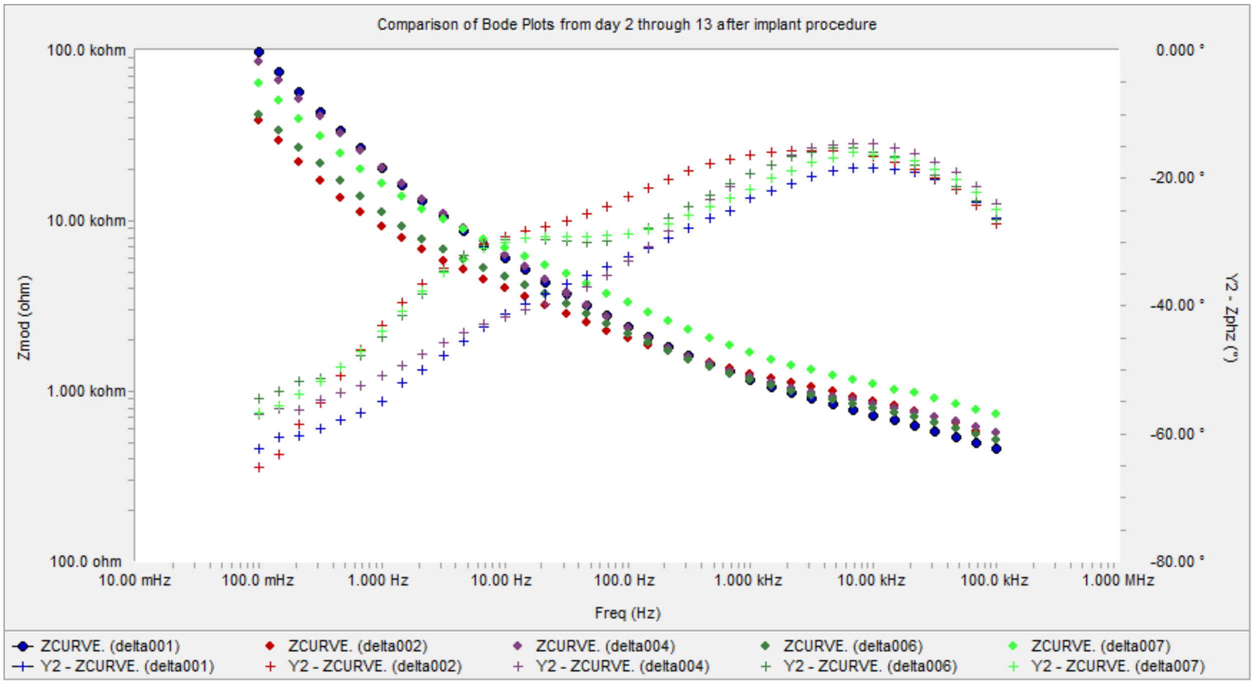

Figure 43: Comparison of Bode plots from day 1, 3, 7, 10, and 13 after implant procedure

3. Preparation and Characterization of Coated CNT Thread

3.1. Materials

Significant interest exists in employing CNT thread as a substitute wire for transmitting power and data across the skin. Substituting CNT should provide a more flexible medium that will likely reduce irritation from flexing and bending of metal wires. A properly selected polymer coating has potential to provide a surface more suitable for cellular adhesion, potentially reducing the risk of bacterial infection through the gap in the skin produced by the wire.

The CNT wire must have a coating to ensure that all current flowing between electrodes is flowing through the working electrode and not directly from the transmission wire through the tissue. Atkins & Pearce has developed a process to coat CNT based thread with polyvinyl chloride (PVC). PVC has a high electrical resistance and thus satisfies electrical requirements. To be usable, it must be possible to selectively remove the coating from the CNT thread at necessary points, in particular, at the terminals of the wire. PVC dissolves in tetrahydrofuran (THF). The lab received the PVC coated CNT thread completed by Atkins & Pearce on January 26, 2011. 2.5m were allocated for implementation in EIS corrosion monitoring. Provided information from Atkins Pearce can be found in Table 3.

Atkins and Pearce CNT Batch 1	
Turns per mm	6
Nominal Diameter	40 μm
Break Strength	97 gf
Coating	PVC
CNT Lot	8/26/2010

Table 3: Properties of 40 micron PVC coated CNT thread

3.2. Optimization of PVC Coating Removal Technique

Currently, CNT based thread has a resistivity orders of magnitude larger than individual carbon nanotubes due to the high resistance occurring at junctions between nanotubes. Before implementing the Atkins & Pearce thread, detailed characterization must be conducted to verify that consistent electrical properties in an acceptable range for the application are observed. Several tests were conducted on the sample thread after removing the PVC coating under varying conditions to determine if the sample was acceptable and to determine the optimal PVC coating removal procedure.

First, 6 samples, each approximately 4cm long, were submerged in THF for varying times, ranging from no THF exposure to 3 minutes THF exposure. The resistance was measured by contacting the CNT thread at 2 points directly with the test leads of an Agilent 34401A benchtop multimeter. Slight variation in test lead separation occurred, and is controlled for better in later experimentation. Resultant data is plotted in Figure 44. The zero second THF exposure yielded a resistance of 23 kΩ, and is not included on the plot because of the huge change in magnitude.

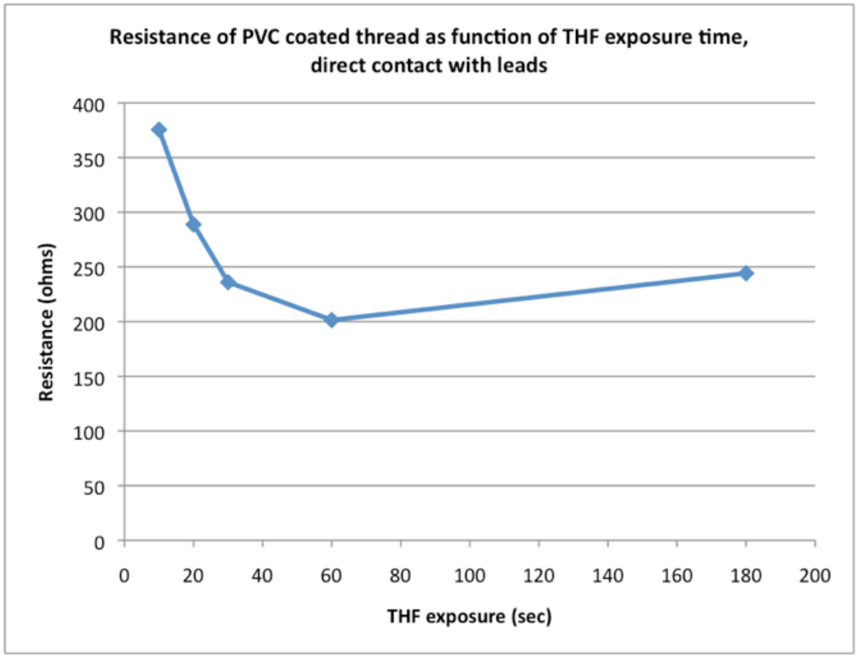

Figure 44: Variation in impedance as function of THF exposure for PVC coated CNT thread. Contact made directly with multimeter leads. Resistance of sample not exposed to THF is 23.06 kΩ

The electrical connection between the CNT thread and multimeter leads was very unstable. To address this, a second set of measurements was taken on CNT thread samples soaked in THF for varying times and mounted on a glass slide. Terminals were constructed by applying small quantities of conductive silver epoxy at the desired separations on the thread. Multimeter leads in contact with the silver epoxy yielded significantly more stable measurements, which are plotted in Figure 45. The zero second THF exposure sample measured a resistance of 2.4MΩ/m, and is not included due to the huge change in magnitude.

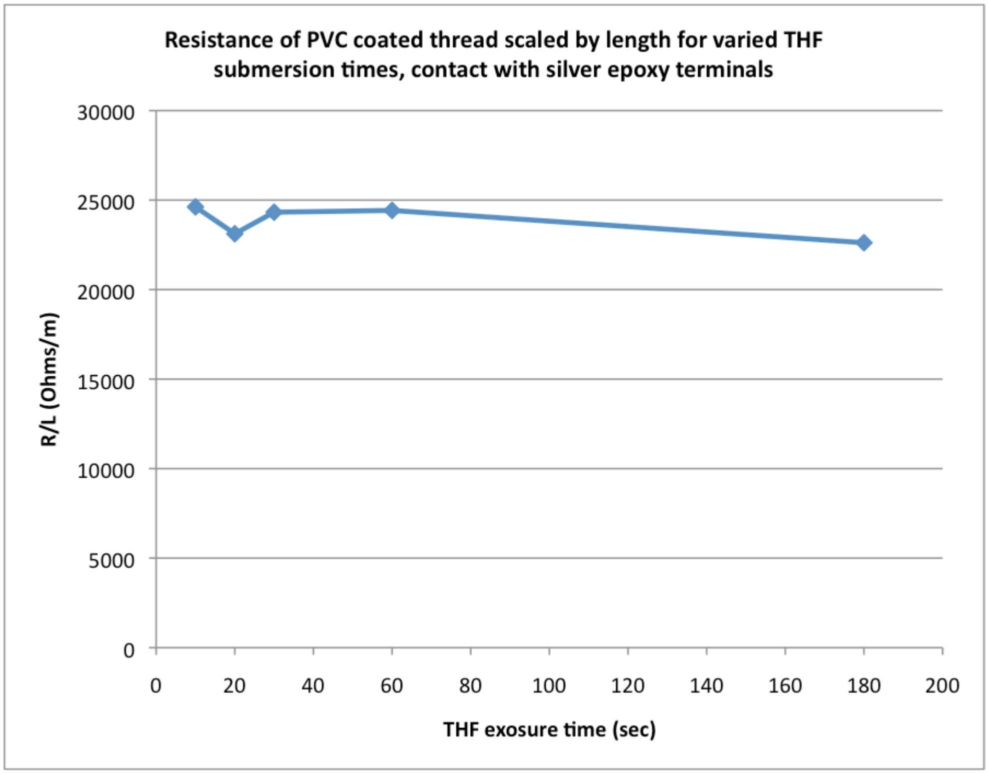

Figure 45: Variation in resistance scaled by length as function of THF exposure time for PVC coated CNT thread. Contact made with silver epoxy at terminals of thread. Resistance of thread before THF exposure is 2.42 MΩ per meter.

In summary, any THF exposure decreased the resistance by orders of magnitude, indicating a high resistance of the PVC layer. Increased exposure generally lowered the resistance further, however by a limited amount. The sensitivity to the THF exposure time was greater when contacting the sample directly with multimeter leads compared to samples with terminals made of silver epoxy. As a result, for applications where manual contact will be made directly to the CNT thread, care should be taken to optimize the THF exposure time accordingly.

Next, multiple DC resistance measurements were taken on the same samples of thread, varying the electrode separation in attempt to estimate resistivity and contact resistance. Figure 46 and Figure 47 show this relationship for samples submerged in THF for 30 and 180 seconds, respectively. Both plots suggest that the contact resistance is very small, and the strong linear relationship suggests that the measured slope accurately represents the resistivity of the thread. The limiting factor of the accuracy of this experiment was the accuracy of the distance measured for electrode separation. This limited accuracy, coupled with a very small quantity of measurements, is likely the cause of the unrealistic y-intercept depicted in Figure 46 for the case of 30 seconds THF exposure, which suggests a negative contact resistance.

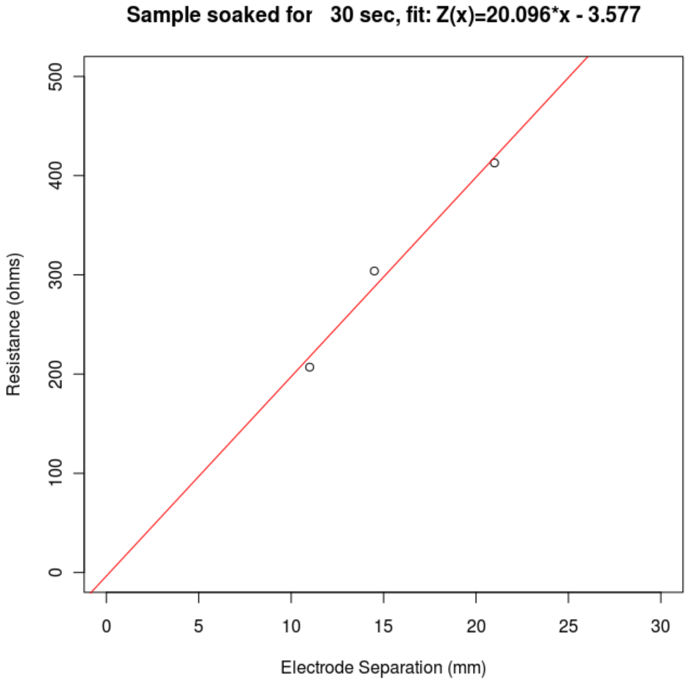

Figure 46: DC resistance as function of electrode separation for PVC coated thread submerged in THF for 30 seconds

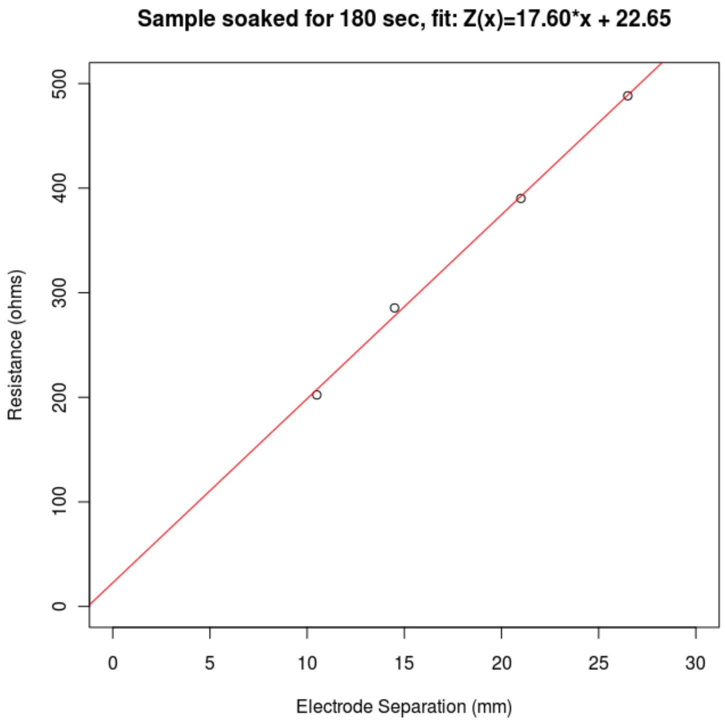

Figure 47: DC resistance as function of electrode separation for PVC coated thread submerged in THF for 180 seconds

Next, samples exposed to THF for varying durations were examined via SEM. Figure 48 shows images for no THF exposure, 10 seconds, 45 seconds, and 180 seconds of THF exposure. A drastic visual change to the appearance of the sample becomes evident even after just 10 seconds of THF exposure, as many large surface irregularities are removed and a highly organized twisted thread is observed. Increasing the exposure time appears to give the THF opportunity to attack material in between individual fibers, as the gaps between fibers seem to gain more definition. Finally, after 3 minutes the structure of the thread appears to start deteriorating. It is likely that the thread is absorbing the THF at this time point. This evidence warrants analysis of the effect of duration of THF exposure on the mechanical properties of the CNT thread.

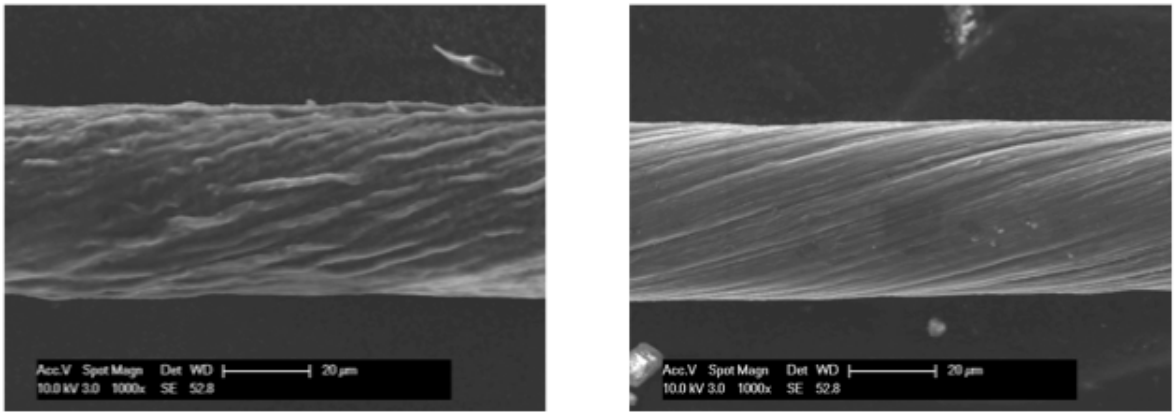

PVC coated

10 sec THF exposure

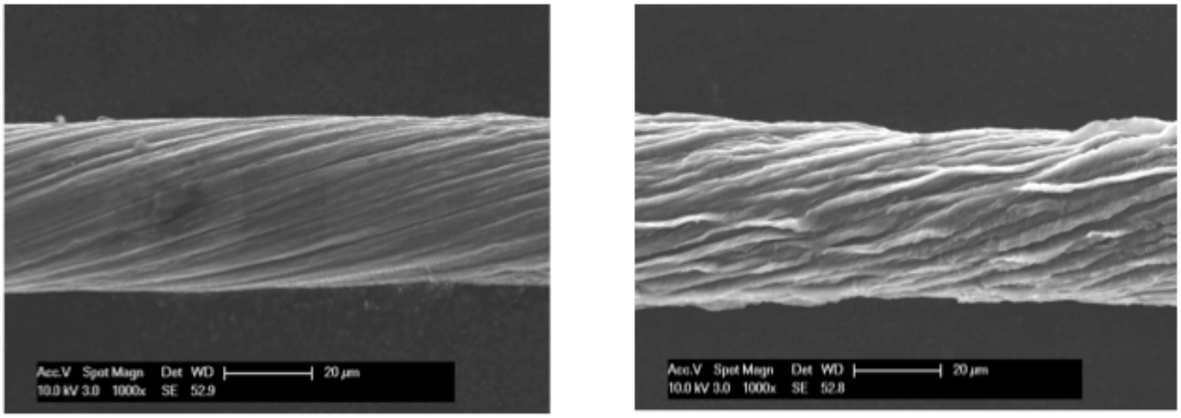

45 sec THF exposure

180 sec THF exposure

Figure 48: SEM images of PVC coated CNT thread after varying duration of THF submersion

Mechanical testing was conducted on the samples. Due to the limited trials conducted on the mechanical testing apparatus, the error bars in Figure 49 allow for no conclusions to be drawn regarding the effect of THF exposure on mechanical strength. This shifts the deciding factor for THF exposure during the preparation of samples to be decided exclusively by electrical properties and SEM imagery. A clear increase in electrical properties was observed when increasing the submersion time up to 45 seconds, and a visible deterioration of the thread was observed at 180 seconds. As a result, 30 seconds was chosen as the ideal THF exposure time for samples used in future experiments.

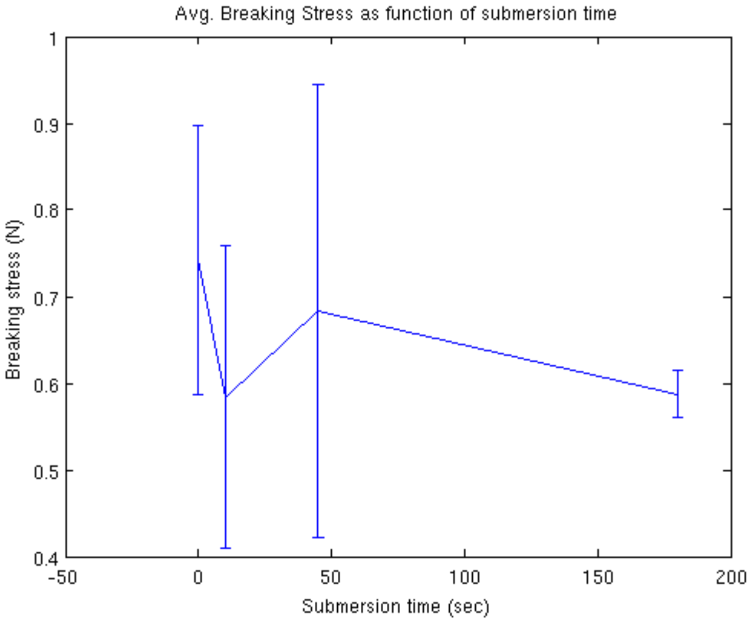

Figure 49: Breaking strength of PVC coated CNT thread as function of THF exposure time. Error bars represent 2 standard errors

The extreme fragility of the CNT thread is a limiting factor for applying it in mouse tests as intended. Increasing the thickness of the CNT composition of the thread would have the added effect of reducing the impedance of the thread by providing additional current paths in parallel. As such, attempts were made to increase the strength by plying 3 plys of the 40-micron thread together on the available spinning apparatus in the Nanoworld lab. After several attempts, the author had no success getting a stable thread to spin and stay twisted together without breaking. This may be a result of the PVC coating interfering with the CNT's ability to stay twisted together or may be a user error due to the author's lack of experience with the equipment.

Instead of increasing the strength by spinning multiple threads together in the Nanoworld lab, a new set of 4-ply PVC coated thread was provide by Atkins and Pearce. This thicker thread proved to be significantly easier to work with. Unfortunately, only a very small sample was provided, leaving inadequate material to conduct a thorough analysis on to determine the exact mechanical and electrical properties. A single comparison was conducted comparing the 4-ply thread to the smaller 40 micron thread, where each sample was exposed to THF for 30 seconds and mounted to a glass slide with low-temp curing conductive epoxy. The 40 micron thread had a resistance of 191.89 Ω across a 8mm sample, and the 4-ply sample had a resistance of 155.6 Ω across a 14.5 mm sample. Because it was observed earlier that the contact resistance was very low, particularly when contact is made with silver epoxy, it is appropriate to compare the resistance divided by the electrode gap. The 40 micron thread displayed a resistance of 23.99 Ω/mm, and the 4-ply thread displayed a resistance of 10.73 Ω/mm. As a result, the 4-ply thread led to a reduction in resistance by over a half.

Multiple attempts were made to measure the mechanical properties of the 4-ply thread. Unfortunately, these attempts were unsuccessful in getting the PVC coated sample to stick in the taped mount. Joe Kluener, who has significant experience working with this equipment, has encountered this problem frequently when working with coated CNT samples. Because of the extremely small quantity of available thread, attempts to measure mechanical properties were abandoned to ensure that enough was left over for mouse experiments.

3.3. Characterization of 40 micron CNT thread connected electrodes

Full electrical characterization of the CNT connected electrodes requires analysis of the complex impedance. In this set of experiments, a completely fabricated Mg electrode is used, as this is the end product of interest for in vivo experimentation. The fabrication of this electrode is discussed in full detail in Chapter 2. Briefly, the PVC coating is removed from the distal 2mm of the CNT thread. This end is connected to one face of the Mg pellet with low temperature curing conductive epoxy (curing epoxy in the oven would damage the PVC coating). This top face of the Mg pellet is then coated with an insulating epoxy. Approximately 1 cm of the unattached end of the CNT thread is submerged in THF to remove the PVC coating, resulting in a connecting wire that is insulated in all regions expected to come in contact with the solution. A piece of copper tape is adhered to this exposed face with conductive epoxy to provide a suitable location to clip an alligator clip to.

First, a potentiostatic EIS sweep is conducted over the dry electrode with the Gamry potentiostat. For a dry measurement, the Ag/AgCl is unusable. Instead, the working electrode is connected to 1 side of the system (the Mg sample) and both the counter and working electrodes are clipped to the other (the copper tape), as shown in Figure 50. The standard potentiostatic AC impedance configuration is used on the Gamry. The resultant Bode plots are presented in Figure 51. Notably, low phase is observed at low frequencies, with a dominant real portion of the impedance at approximately 315 ohms. The phase starts shifting rapidly at higher frequencies (greater than 1.0 kHz), but even at 100 kHz, the phase does not go beyond -10 degrees. As a result, we can approximate the electrode as a pure resistor at low frequencies with small capacitive contributions at high frequencies, and a relatively consistent impedance magnitude of approximately 315 ohms.

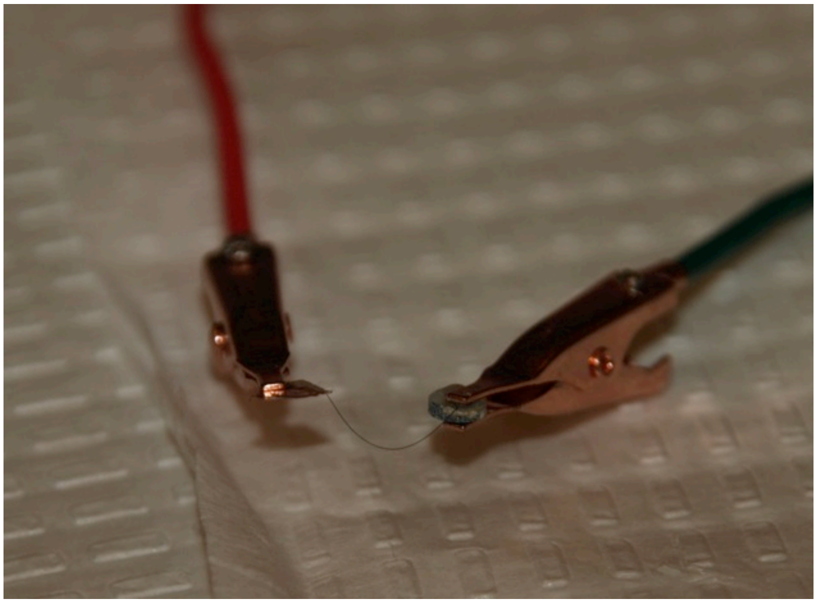

Figure 50: Setup for EIS across dry CNT connected electrode

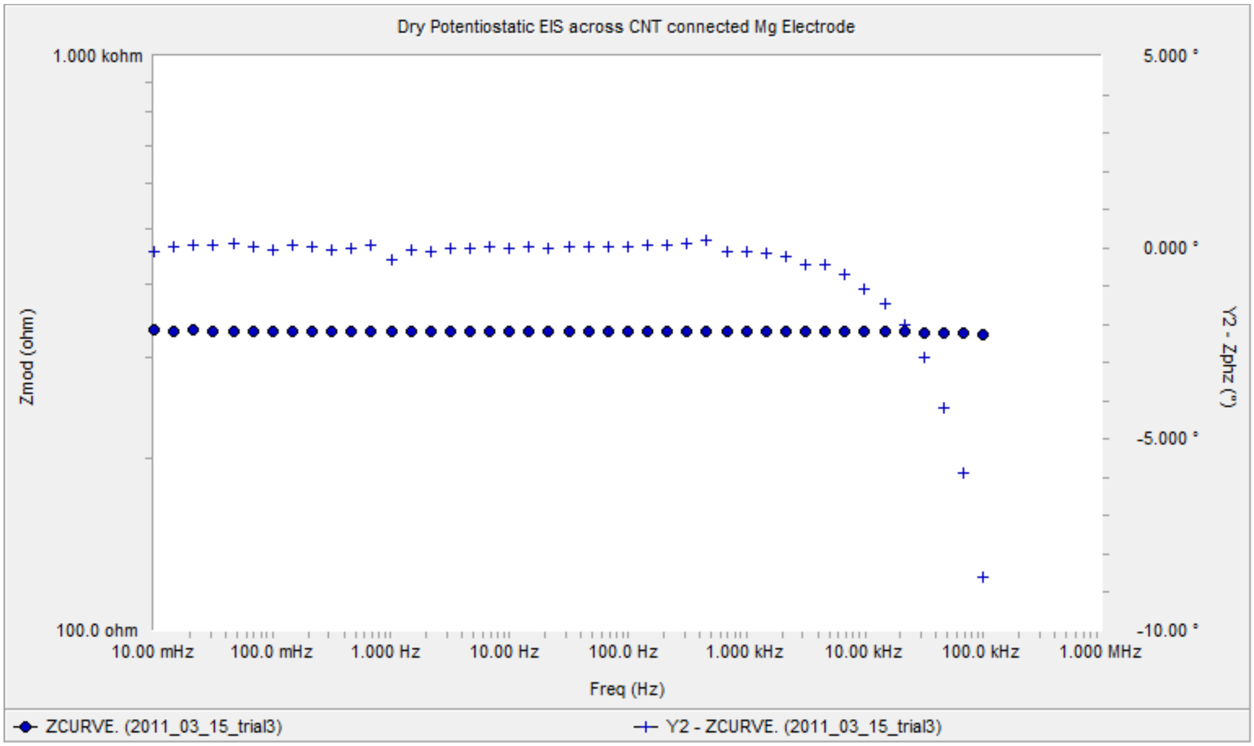

Figure 51: Bode plots for EIS across dry CNT connected electrode

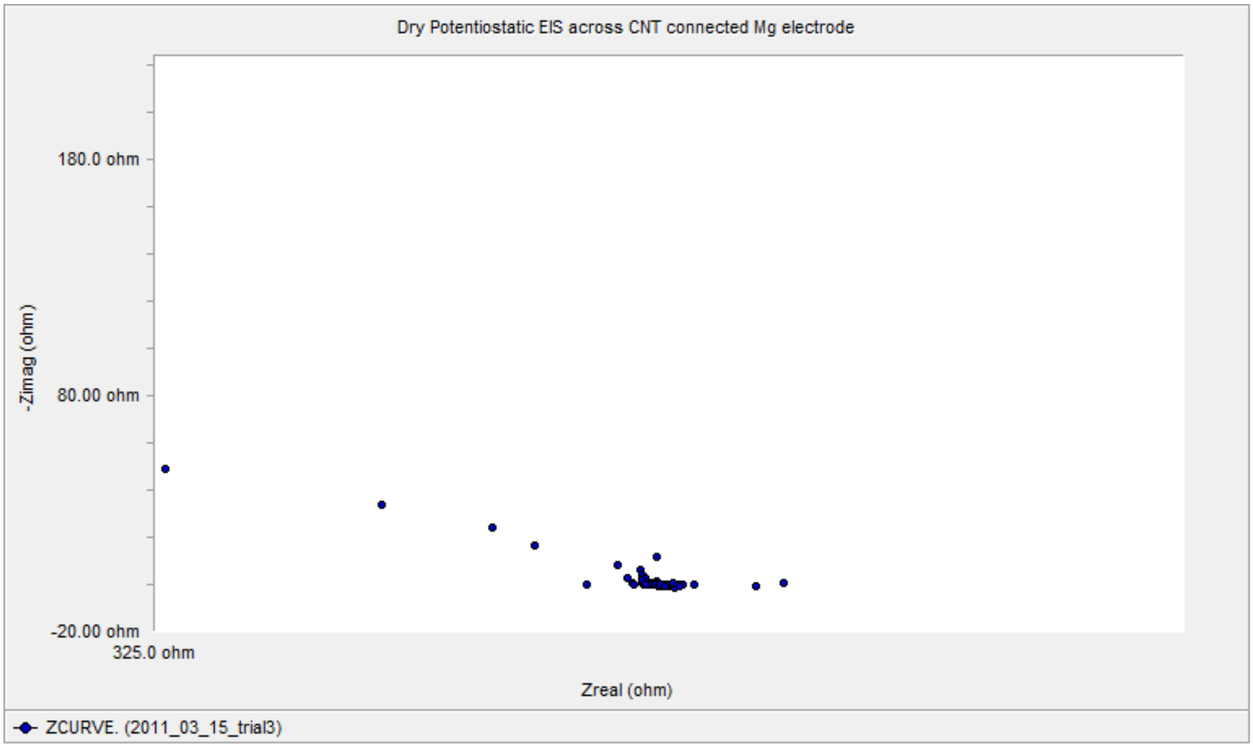

Figure 52: Nyquist plot for EIS data across dry CNT connected electrode

Next, EIS data is collected for the CNT connected electrode in an electrolyte. The electrode is suspended such that the magnesium pellet and a portion of the insulated section of the CNT thread are submerged in 0.85 M NaCl. A platinum counter electrode and Ag/AgCl reference electrode are employed. Potentiostatic AC impedance data is recorded. For comparison, the same data collection is conducted for an identically dimensioned magnesium pellet connected by insulated copper wire. Resultant Bode plots are presented in Figure 53, and Nyquist plots are presented in Figure 54. Analyzing the Bode plots, the CNT electrodes exhibit higher impedance at high frequencies, indicating a higher resistive contribution. As the dry EIS data showed the CNT thread could be modeled as a predominantly resistive component, this is to be expected. However, at low frequencies, the magnitude of impedance of the CNT connected electrode is significantly smaller. The electrode separation was relatively consistent for both trials. As a result, it appears that some current must be leaking through the insulated sidewalls of the CNT thread. This would open ionic current pathways in parallel to those forced through the magnesium pellet, leading to a reduction in impedance.

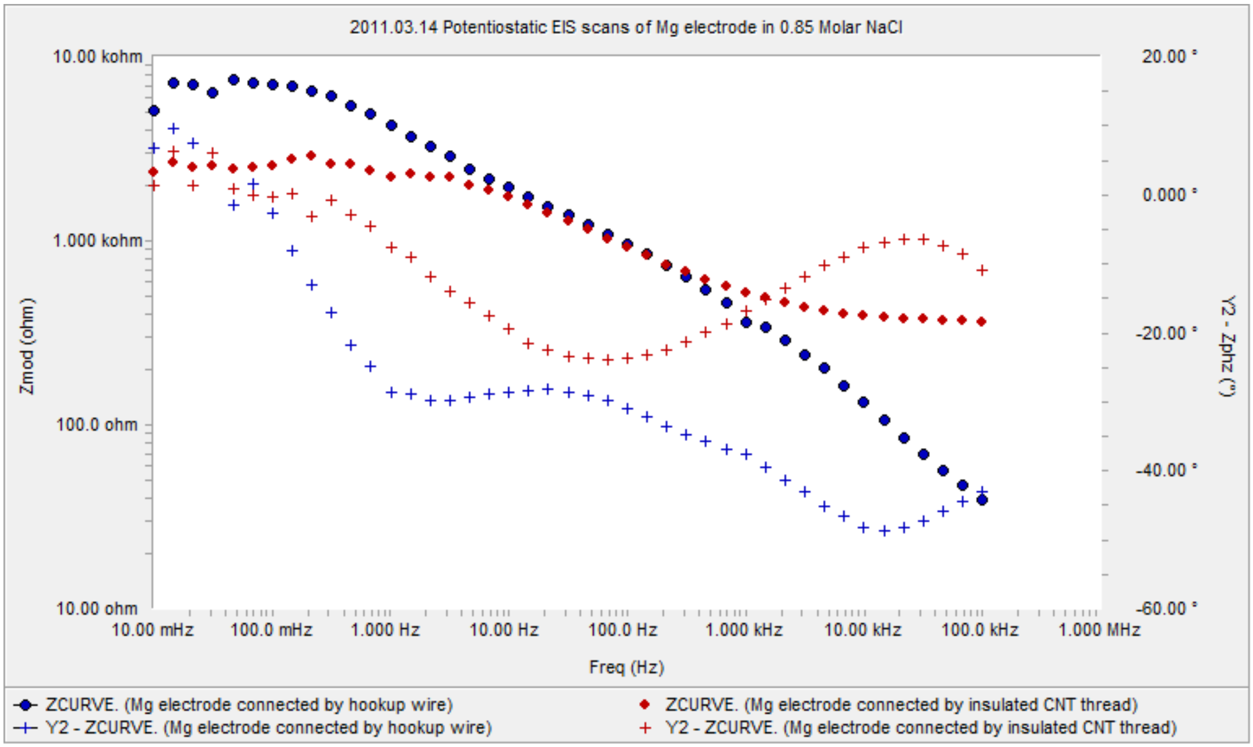

Figure 53: Bode plots for CNT connected electrode (red) and the copper wire connected electrode (blue) in NaCl solution

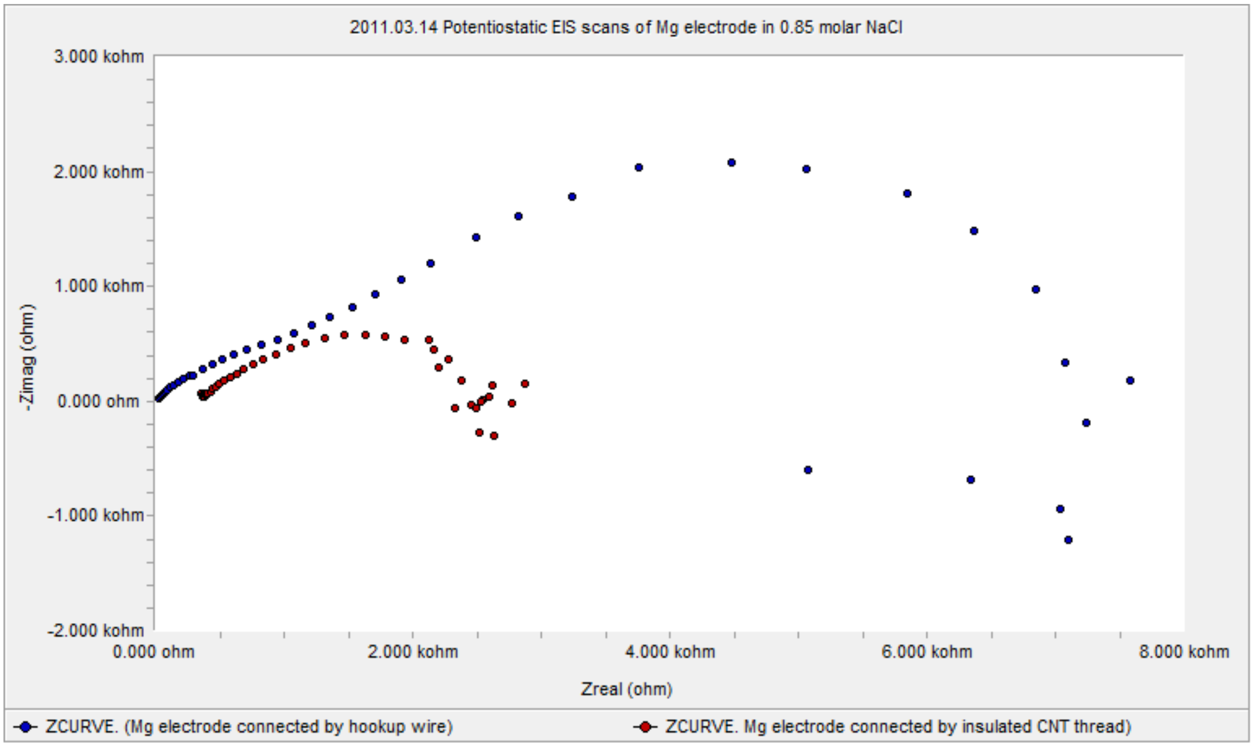

Figure 54: Nyquist plots for CNT connected electrode (red) and copper wire connected electrode (blue) in 0.85 M NaCl solution

4. In Vivo Corrosion Control by Cathodic Protection

4.1. Summary

Cathodic protection is a common method of corrosion control where corrosion is controlled by suppressing anodic reactions by applying an external voltage or a sacrificial anode. This method can be potentially used in implanted devices to achieve greater control over the biodegradation of the device. Preliminary research is covered in this section demonstrating the potential for the application of this technique on implanted devices.

First, a test case is conducted on 2 electrodes inserted into raw chicken. Raw chicken is commonly used as an experimental replacement for living tissue. Next, as a proof of concept demonstration, a DC voltage is applied between a pair of electrodes implanted in a mouse, and the resultant current is recorded.

4.2. Raw Chicken Preliminary Experiment

The equipment setup for this experiment is shown in Figure 55. Frozen raw chicken breast is thawed for this experiment. 1 graphite and 1 magnesium electrode, connected by hookup wire, are inserted into incisions in the chicken with a separation of approximately 2 cm, as shown in Figure 56.

Figure 55: Experimental setup for applying corrosion control in raw chicken

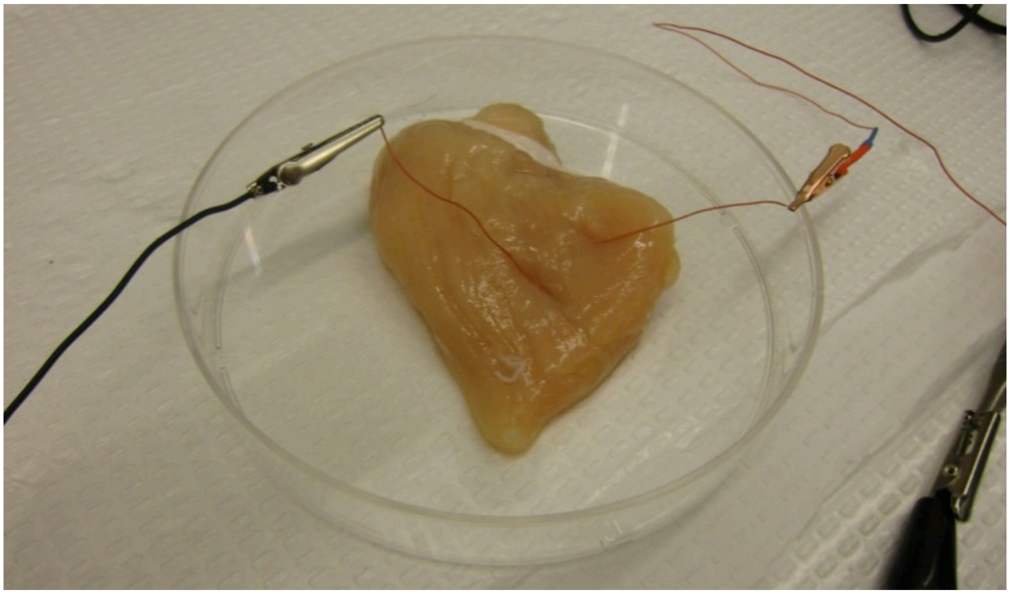

Figure 56: Magnesium and graphite electrodes inserted into raw chicken sample

A set of potentiostatic EIS data is collected on the Gamry potentiostat to demonstrate raw chicken's suitability as a tissue replacement. The resultant data is plotted in Figure 57, and a coplot of data collected in raw chicken and data collected in mouse 'delta' is shown in Figure 58.

Differences in magnitude are present, but the general properties are very similar, justifying the use of raw chicken in this experiment.

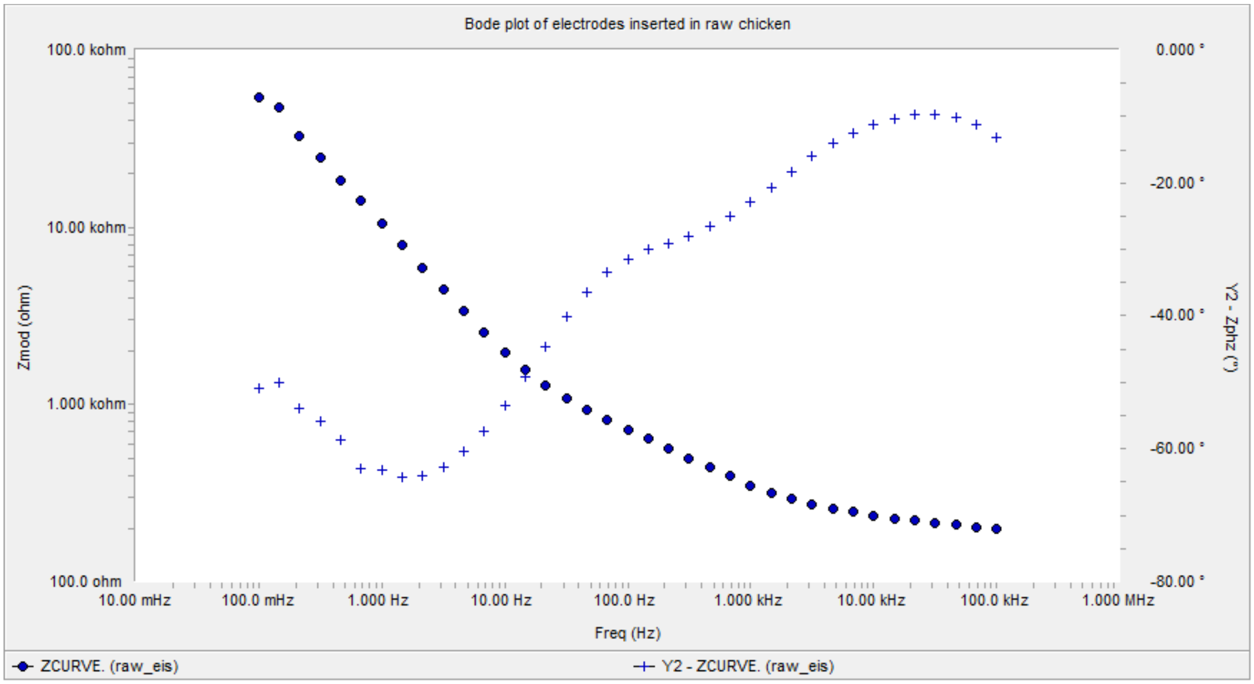

Figure 57: Potentiostatic EIS data for Mg/graphite electrode pair in raw chicken

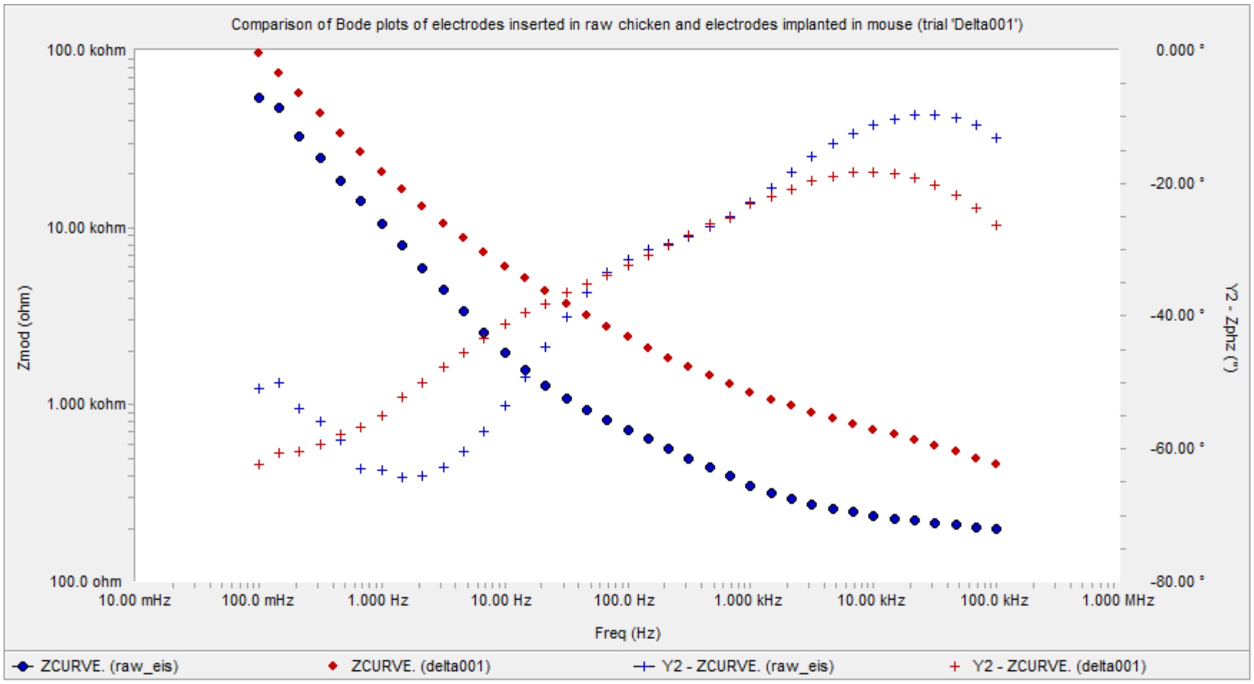

Figure 58: Potentiostatic EIS data for Mg/graphite electrodes implanted in raw chicken (blue) compared to electrodes in mouse 'delta' (red)

The open circuit potential is collected for 200 seconds, and the resultant data is shown in Figure 59. Recorded potential is in the range of 1.6-1.7 V. For verification, the open circuit potential is also measured with an Agilent benchtop multimeter, with recorded potential of 1.62V. The same multimeter is used to measure the current for the completed electrochemical cell in tissue. An observed current of 0.130 mA is observed initially. This current decayed steadily to 0.0930 mA after 60 sec.

Next, an offsetting external potential of 1.7 V is applied by a BK Precision 1667 DC regulated power supply. The benchtop multimeter is wired in series, and a current of .0005 - .001 mA is measured in the opposite direction as the completed cell. As a result, the anode of the cell is turned into the cathode, and cathodic protection is achieved.

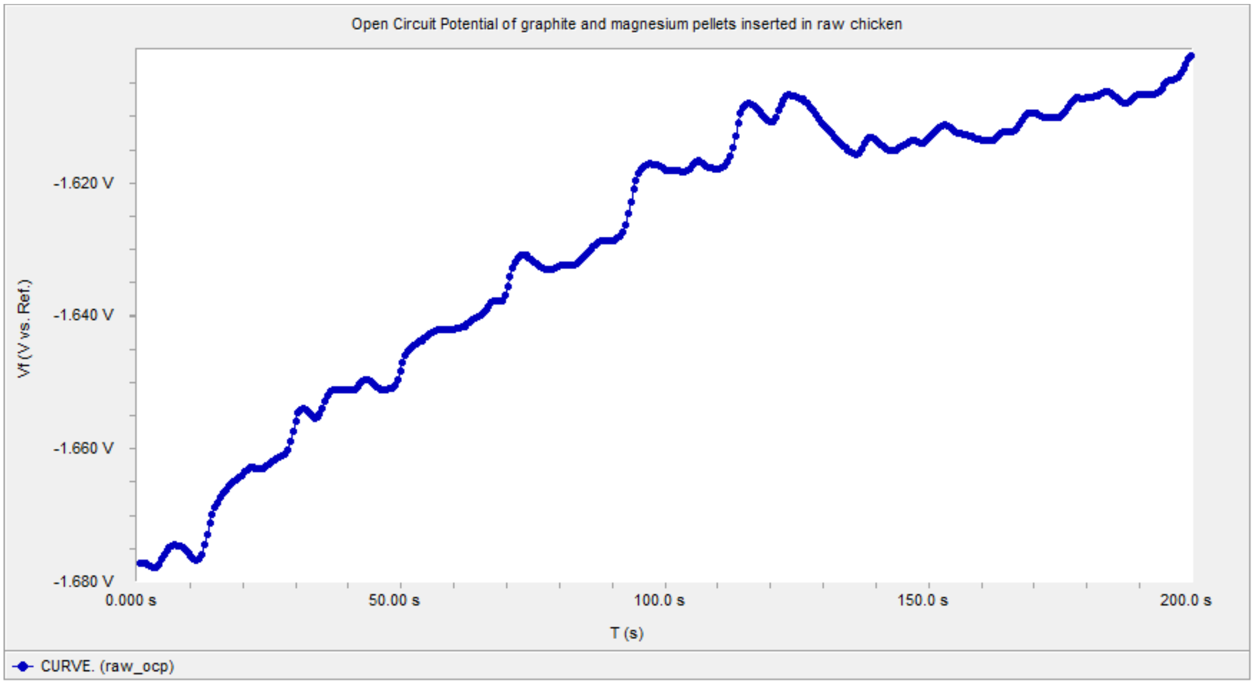

Figure 59: Open circuit potential for graphite and Mg electrodes inserted in to raw chicken

4.3. Corrosion Control in Mouse Delta

Next, attempts are made to demonstrate cathodic protection in mouse ‘delta’, which had a magnesium and a graphite electrode implanted in its upper back. The mouse was knocked unconscious by an injection with Nembutal prior to measurement. Attempts to measure the open circuit potential failed to record a stable potential. However, the observed range of potentials were significantly lower than what was measured in the raw chicken experiment. The DC power supply was wired into the system to apply an external voltage. The resultant measured currents as a function of applied voltage are plotted in Figure 60.

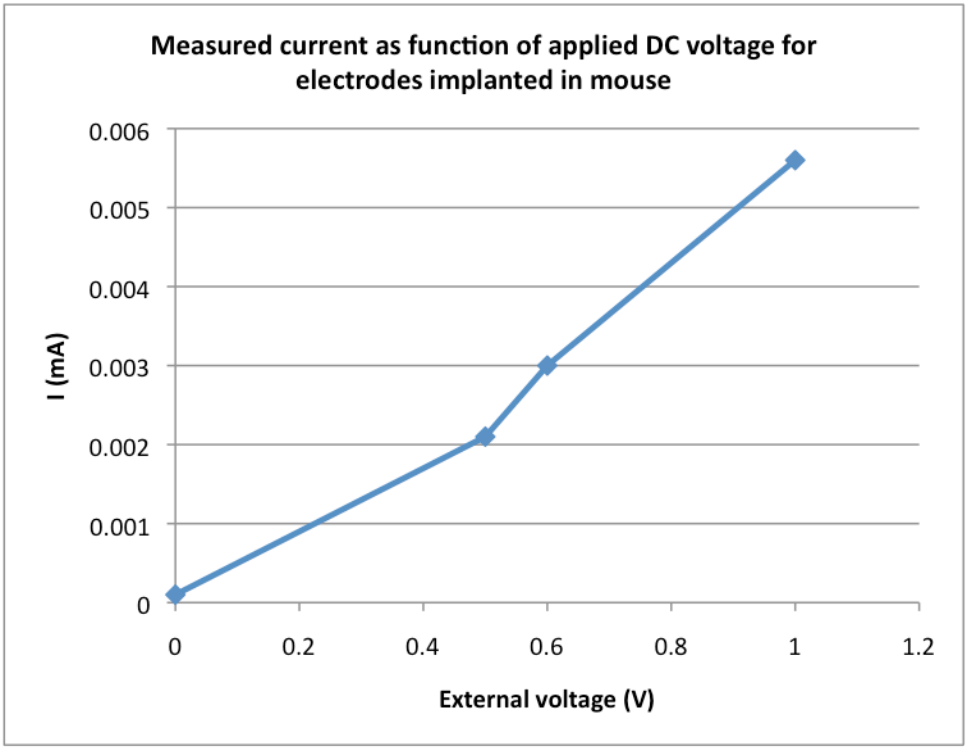

Figure 60: Current as function of voltage for external potential applied across implanted electrodes in mouse 'delta'

At the time of this experiment, the electrodes had been implanted in the mouse for 13 days. The measured open circuit potential was significantly lower than measured in the raw chicken experiment, likely indicated significant surface chemistry changes since the time of implantation. With respect to the effect of the applied current to the health of the mouse, the magnitude of electrical current was too small to cause any harm to the mouse.

5. Electrochemical Impedance Spectroscopy analysis of cancerous tissue

5.1. Summary

EIS is a promising tool for discriminating between tissue types. With the assistance of lung specialists at UC, preliminary experimentation has been conducted investigating the potential for applying EIS to discriminate between benign lung nodules and malignant lung cancer. First, the development of techniques and preliminary testing on deceased mice is discussed. Next, data collected on human tissue removed from patients at University Hospital is presented. At the completion of this document, 4 samples have been evaluated.

5.2. Preliminary Experimentation

Preliminary experimentation was conducted on mouse tissue to develop experimental techniques, determine appropriate equipment, and determine the feasibility of collecting usable data with the available equipment. Analysis of the impedance spectrum through tissue required a set of electrodes that would measure a constant volume of tissue with a constant electrode gap while minimizing damage to the tissue.

The electrodes could either measure impedance by just contacting the surface of the tissue, or by penetrating the tissue and measuring in the internal region. It is likely that the surface of the tissue would be subject to greater variation in properties that would affect the measured impedance, with sources of change including hydration level, temperature differences, and the presence of thin films. As such, small diameter needle type electrodes were chosen to penetrate the tissue while minimizing damage to the tissue.

The author was unable to find a reliable method of employing a reference electrode in measurements that penetrated the tissue. Common reference electrodes employ a glass tube with an open bottom exposing the solution contained in the glass tube to the solution of interest. Such a configuration would not properly penetrate tissue, would be subject to clogging, and would be extremely difficult to disinfect. It was decided to use a 2-electrode configuration in this experiment, similar to what was used in experiments conducted by other research groups.

A constant surface area of the needle electrodes must be exposed to the tissue to ensure comparable measurements. Variation in the exposed surface area would, stated simply, vary the available current pathways and scale the observed impedance accordingly. There was no reliable method found to accurately control the penetration depth of the electrodes, particularly given the unpredictable displacement of the tissue surface during penetration. As a result, the best method for controlling the exposed surface area was to mask all but the distal measurement region of the needle electrodes with an electrically insulating material. Materials tried for this include epoxy, Plasti Dip, and aluminum oxide applied by sputtering.

Initial experimentation employed a pair of GGB tungsten electrodes (Picoprobe model # PT-20-1661-2) separated by 1.5mm and mounted in thin blocks of 0.25" thick acrylic glass to ensure a constant electrode gap. A number 75 drill bit was used to drill the mounting holes for the tungsten electrode. A precision drill press was provided by the UC CEAS machine shop to accomplish this. The needles were held in place by epoxy. The needles were not insulated to provide a constant measurement volume for the first set of measurements. This reduction of experimental consistency was considered acceptable as the experiment was intended to verify the ability to obtain usable data with the available equipment. This electrode configuration is shown in Figure 61.

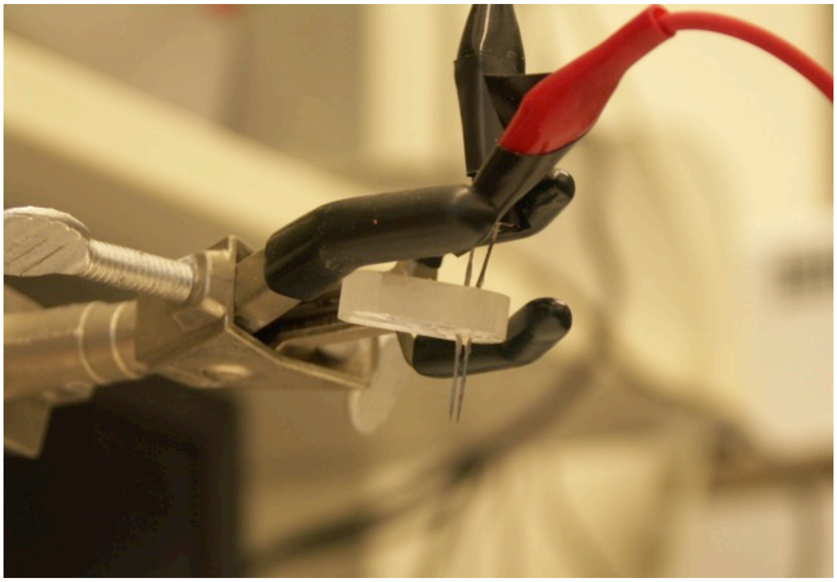

Figure 61: Tungsten electrode configuration for tissue EIS

For the first set of data, a black haired mouse was sacrificed and dissected. The CHI-660c potentiostat was used for this experiment, with the reference and counter leads hooked up to one electrode, and the working lead attached to the other. EIS scans were collected on liver, prostate, kidney, spleen, brain, intestine, heart, lung, and muscle tissue. A full set of data was taken on each of these tissue types while still in the body. A second set of data was taken on each of these tissue types after removing them from the mouse. Data proved to be consistent between scans. A sample pair of measurements is shown in Figure 62. The observed variation in magnitude of impedance is likely caused by variation in electrode penetration. The phase diagram has a characteristic minimum occurring around 500Hz. Figure 63 shows a pair of EIS scans taken from the same tissue sample after removing and reinserting the electrodes, demonstrating the consistency in the data for a given sample. Figure 64 compares the EIS data taken from all tissue samples after removal from the mouse. Certain tissue types appear to be distinguishable by unique phase behavior. Kidney, liver, and heart tissue all demonstrate relative maxima at around 20 kHz, and lung tissue demonstrates a relative minima at a significantly lower frequency than all other measured tissue types. Finally, Figure 65 shows EIS scans from 3 different tumor types, each removed from a mouse model and frozen prior to this data collection.

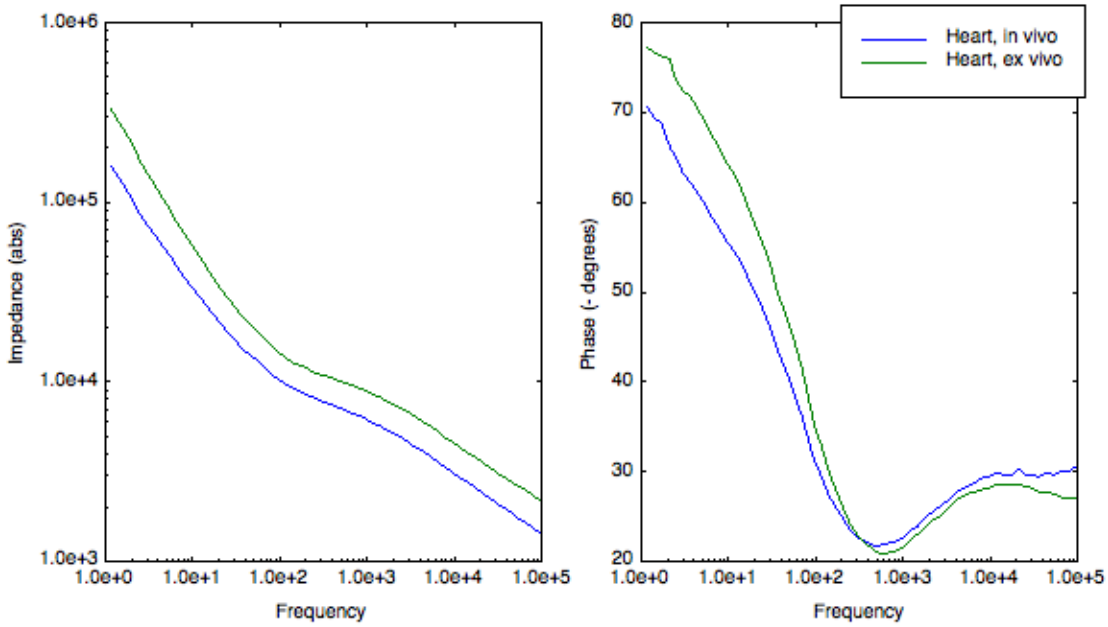

Figure 62: Pair of EIS scans taken on heart tissue with first set of tungsten electrodes

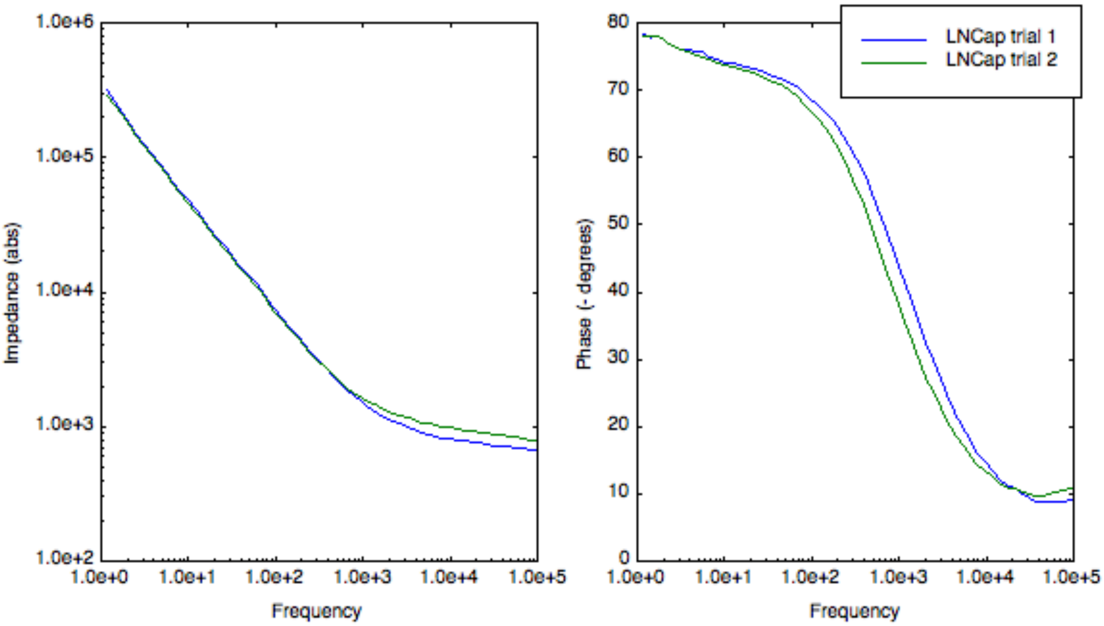

Figure 63: Pair of EIS scans taken from same tissue sample to demonstrate consistency in data. Some variation in electrode penetration occurred.

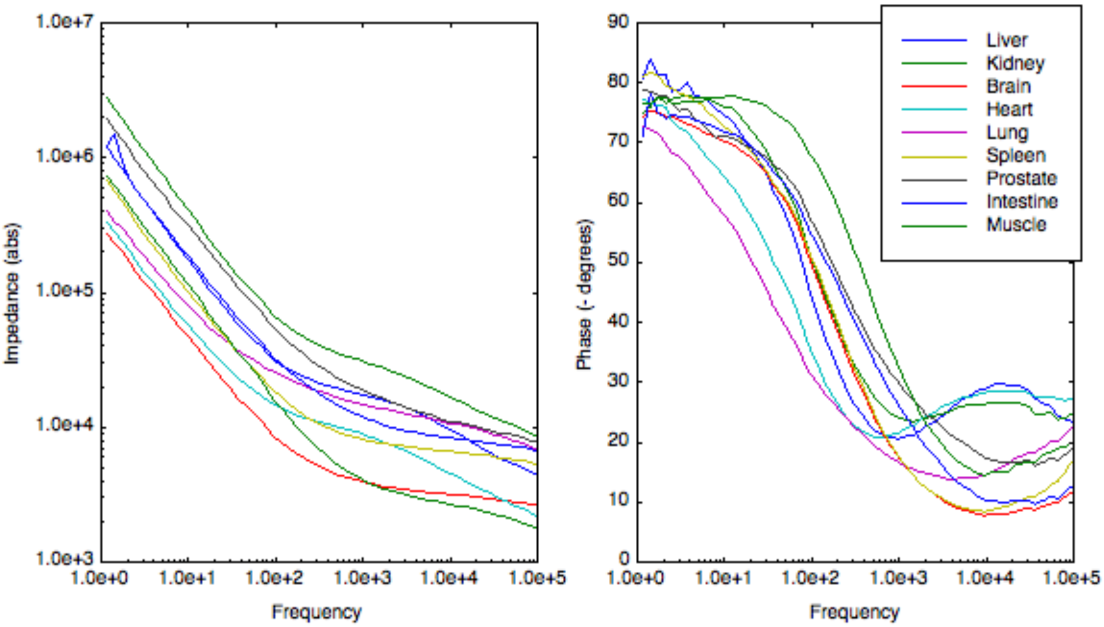

Figure 64: Comparison of all ex vivo measurements taken with first pair of tungsten electrodes

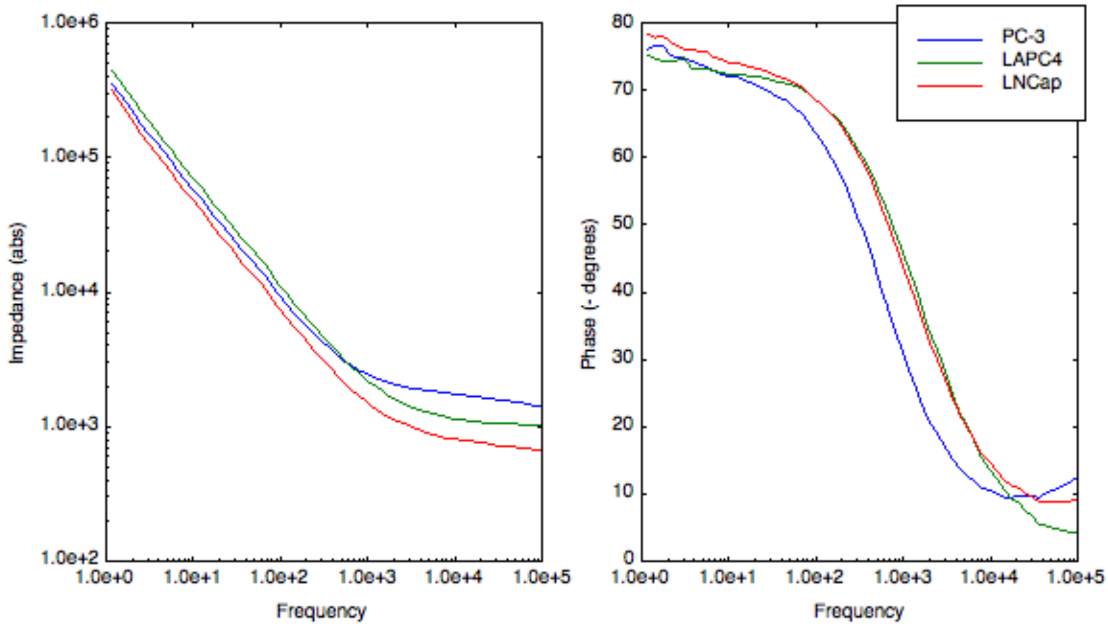

Figure 65: EIS data for cancer samples from mice. Samples were frozen prior to measurement

A single EIS scan took approximately 30 seconds with the CH potentiostat. For this first experiment, the needle electrodes were held by a test tube stand and lowered into the sample. It was extremely difficult to accurately place the needles and hold them perfectly still for the measurement. A stable position is critical to provide smooth EIS data. For future measurements, and alternative electrode insertion procedure was devised. A vertical lifting stage was used to hold the tissue sample. A drill was mounted to control the lift of the stage. The drill speed was tuned to a slow speed to ensure optimal control of the vertical placement of the sample. The tungsten electrodes were held by a test tube stand above the sample. The drill was used to move the sample up and down into the tungsten electrodes. The sample was moved laterally by hand to control where the electrodes penetrated the tissue sample. This provided an extremely stable method with a high level of control over the penetration depth, which became extremely important when working with small tissue samples. The final equipment setup is shown in Figure 66.

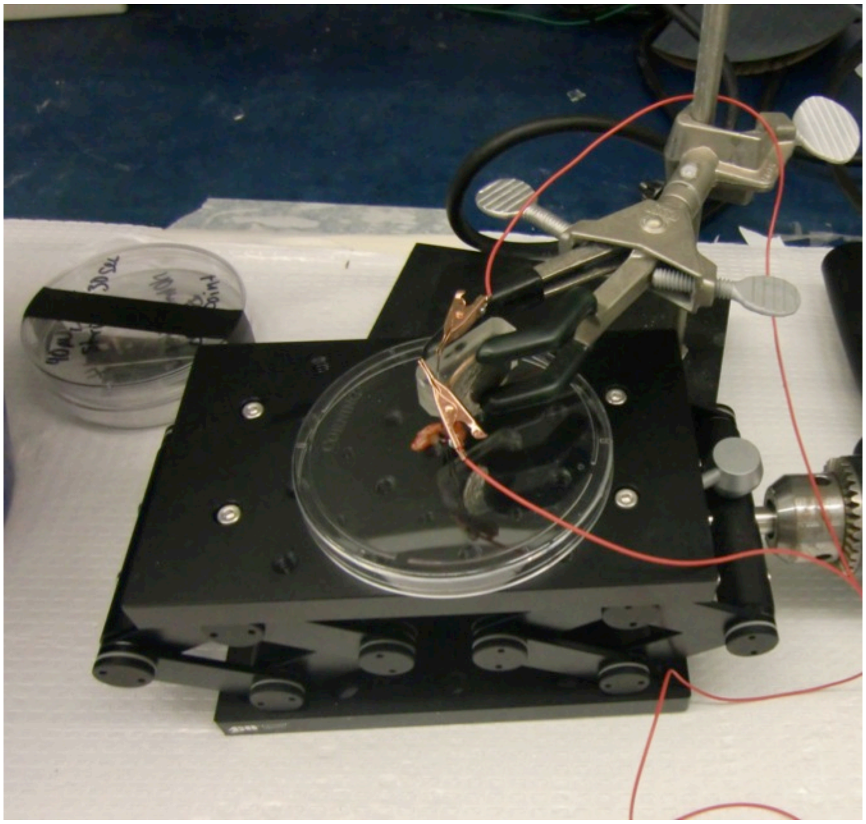

Figure 66: Equipment setup for controlled insertion of Tungsten electrodes into tissue sample

A second experiment was conducted with the improved mechanical setup and a pair of insulated electrodes to provide a better understanding of the procedure. The tungsten electrodes were coated with epoxy except for the distal 2.2mm region. Electrode separation was measured to be 1.3mm, as illustrated in Figure 67. A second black haired mouse was sacrificed, and the same set of tissue types were measured. Resultant data from this experiment can be found in the Appendix.

Several trials were conducted to develop a better understanding of the system. Most importantly, the electrode penetration depth was varied, as shown in Figure 68, where the 2.0 mm depth trial exhibits significantly lower magnitude of impedance than the 0.5 mm depth trial. This follow logic, as increasing the penetration depth exposes the system to additional pathways for current travel in parallel to that exposed to the reduced penetration depth trial. This trial demonstrated the sensitivity of impedance magnitude to penetration depth and the importance of establishing a method to achieve a consistent measurement volume between tests.

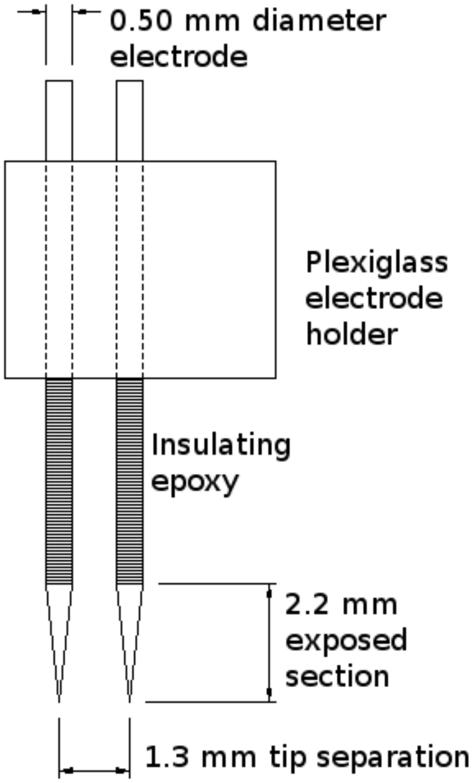

Figure 67: Schematic of insulated electrode for second preliminary dataset

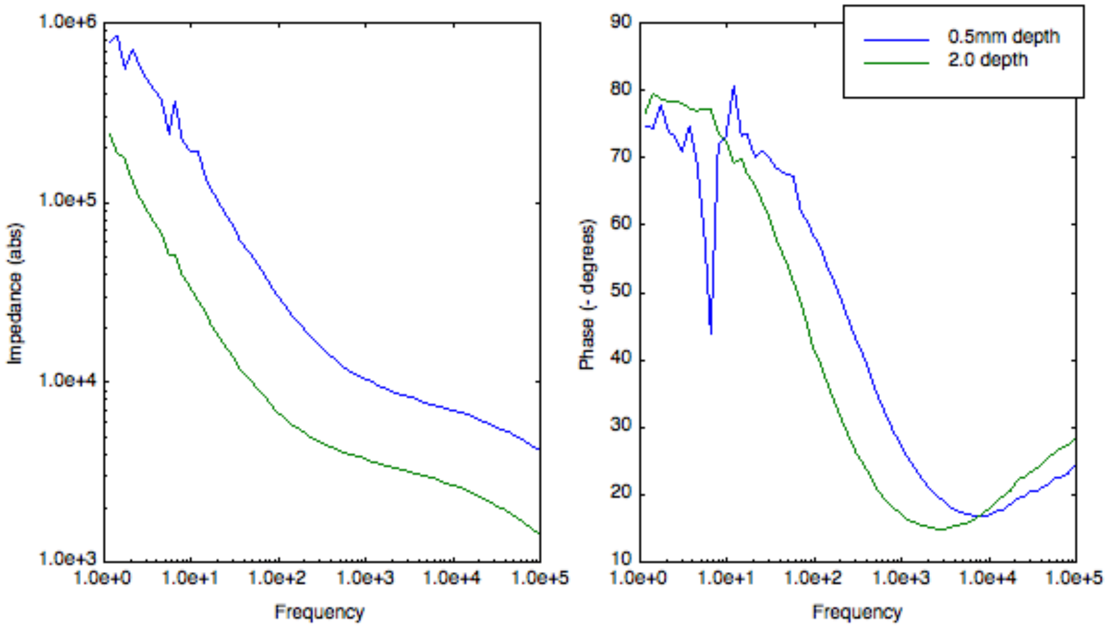

Figure 68: Manipulating electrode penetration depth

5.3. Final electrode fabrication and characterization

Significant noise was observed in EIS measurements taken in preliminary experimentation. One potential source of the noise is the irregular shape of the epoxy insulation used to create the control volume on the tungsten electrodes used. The irregular shape may induce unstable contact regions between the uninsulated portion of the tungsten electrode and the underlying tissue. To eliminate this effect, it is desirable to reduce the thickness of the insulation on the tungsten electrodes.

A new set of electrodes was fabricated to meet these requirements. A pair of GGB tungsten electrodes was prepared by masking the distal 1mm portion of the tip by dipping in Plastidip, as shown in Figure 69. This mask was verified to be stable at 200 degrees Celcius, as required for sputtering. A mounting stand was fabricated for the electrodes by drilling a pair of holes in a small block of aluminum. The dull end of the tungsten electrodes can be inserted into the holes, leaving the entire needle around the masked area exposed to the atmosphere in the sputtering chamber.

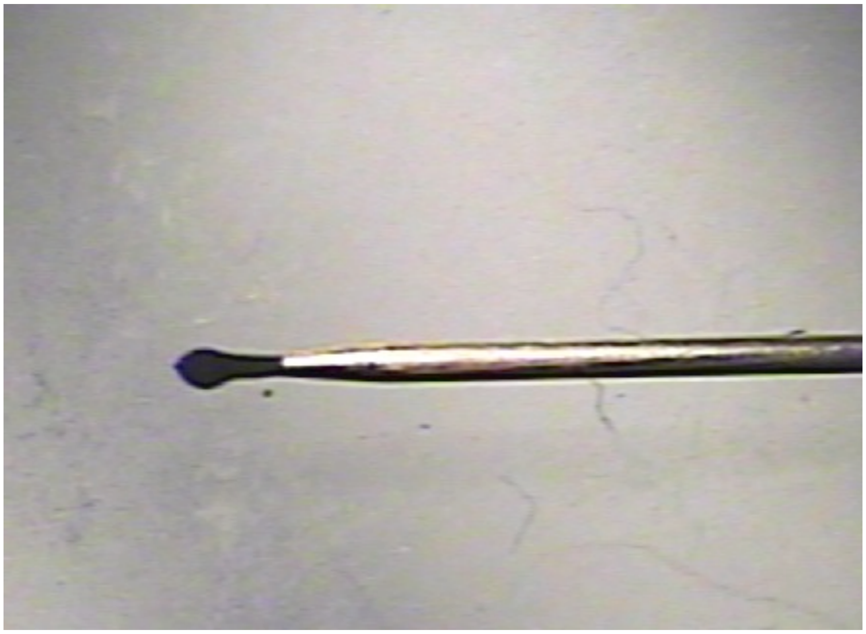

Figure 69: Tungsten electrode with tip masked in preparation for sputtering

This masked electrode was insulated by sputtering aluminum oxide in the clean room. Aluminum oxide is electrically insulating, making it suitable for this application. An estimated thickness of 500 angstroms was deposited. The finished electrodes were mounted in acrylic glass holders similar to previous models. Images of the finished electrodes can be found in Figure 70 and Figure 71.

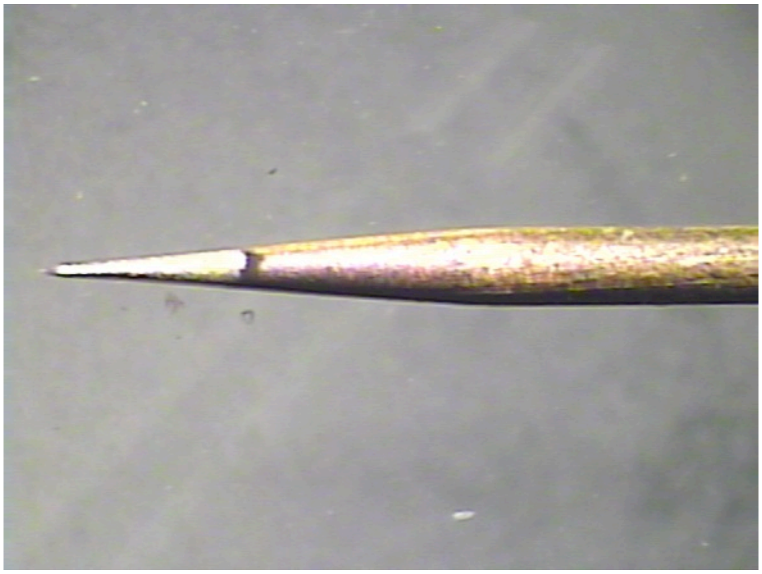

Figure 70: Tungsten electrode with aluminum oxide coating (dark region on right)

Figure 71: Tungsten electrodes insulated with aluminum oxide and mounted in acrylic glass block, showing final electrode separation

The first set of electrodes were characterized by testing for variation in the ac impedance associated with a variation in submersion depth in a 1.05 molar NaCl solution. A perfectly insulated electrode would show very little variance, particularly in the magnitude, for any measurement where the uninsulated portion of the electrode was completely submerged. Unfortunately, the first set of electrodes showed significant variation. In particular, increased submersion depth yielded a reduction in the magnitude of the observed impedance, as shown in Figure 72. As a result, this electrode set is not optimal for providing consistent, comparable data between measurements.

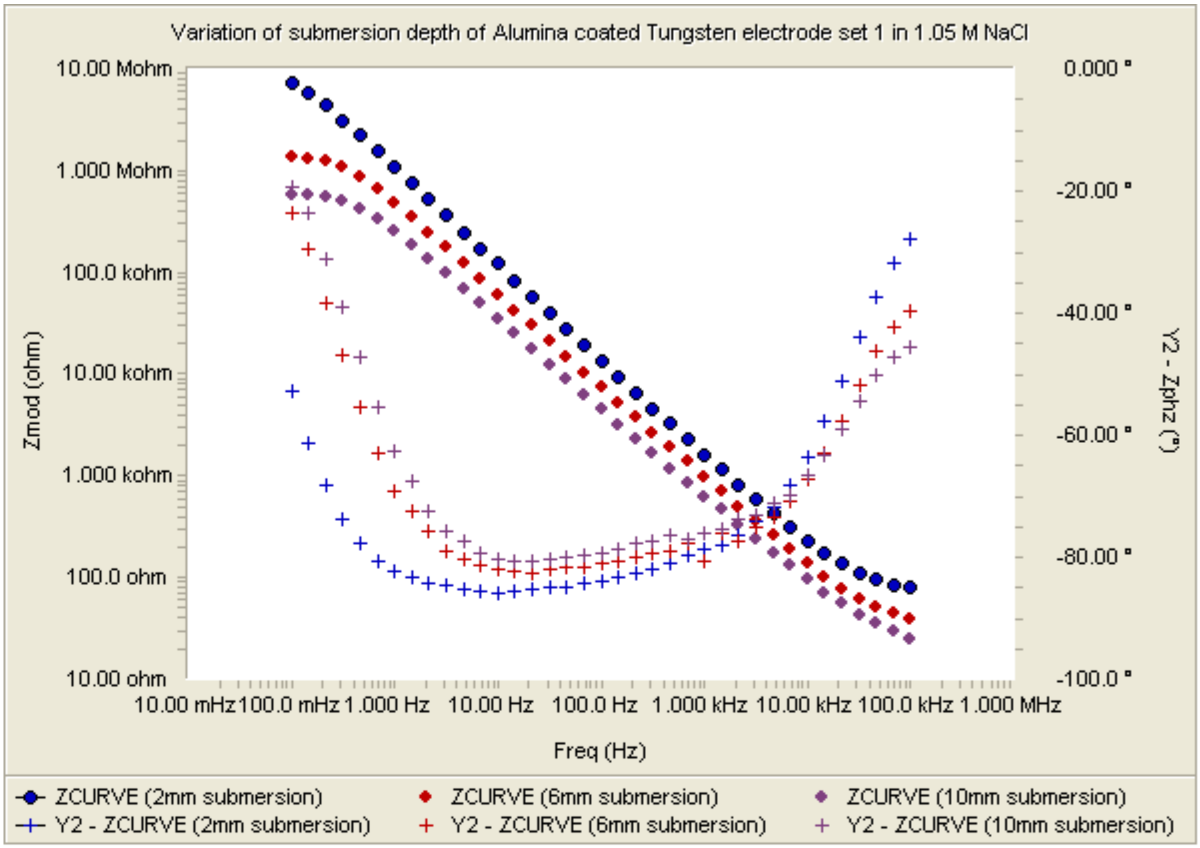

Figure 72: Variation in impedance with submersion depth in salt solution displaying inadequate alumina insulation thickness. Blue curve is 2mm submersion, red curve is 6mm submersion, and purple curve is 10mm submersion.

A second set of electrodes was fabricated with a new insulating coating in attempt to improve electrode quality. 1000 angstroms of Zinc oxide was deposited via sputtering in the clean room by Ron Flenniken. Zinc oxide is classified as a semiconductor, rather than an insulator, but showed a high DC resistance when coated on the tungsten electrodes. Figure 74 shows the EIS for 3 trials with varied submersion depth. While less sensitivity to submersion depth is observed, a significant shift is still observed, suggesting that the insulation is also inadequate for the application.

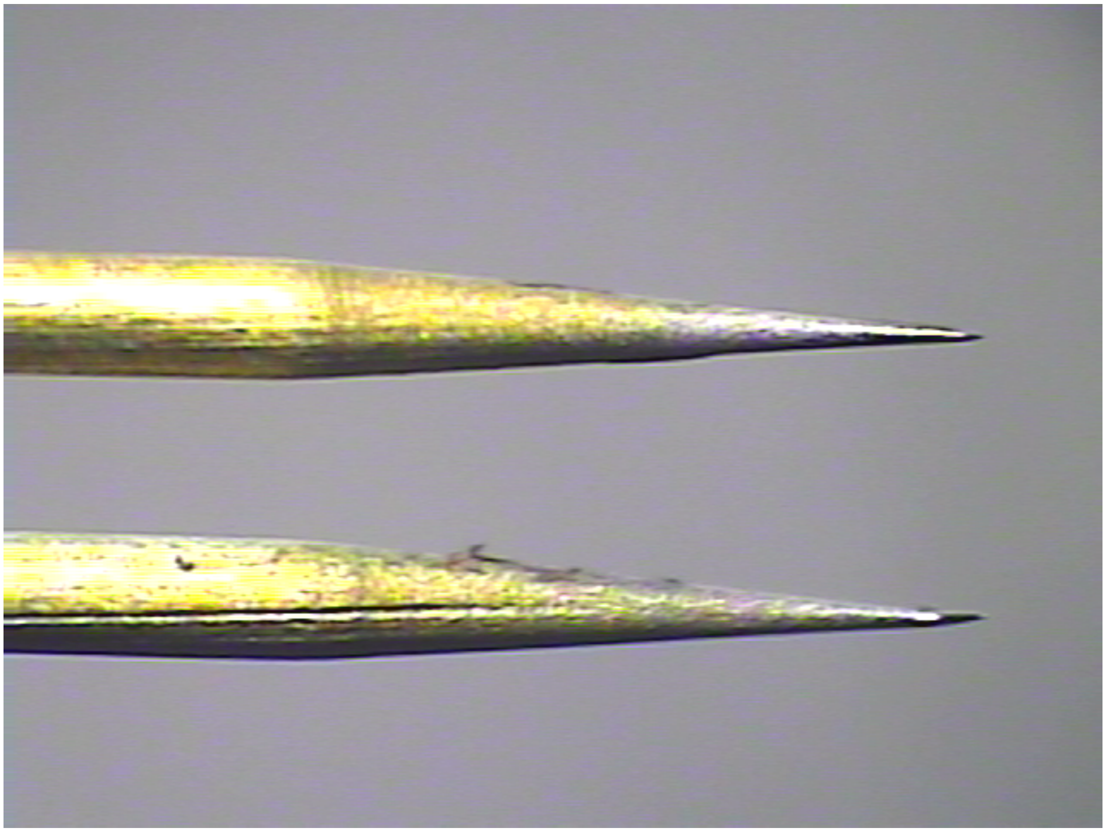

Figure 73: Zinc oxide coated tungsten electrodes, showing final electrode separation

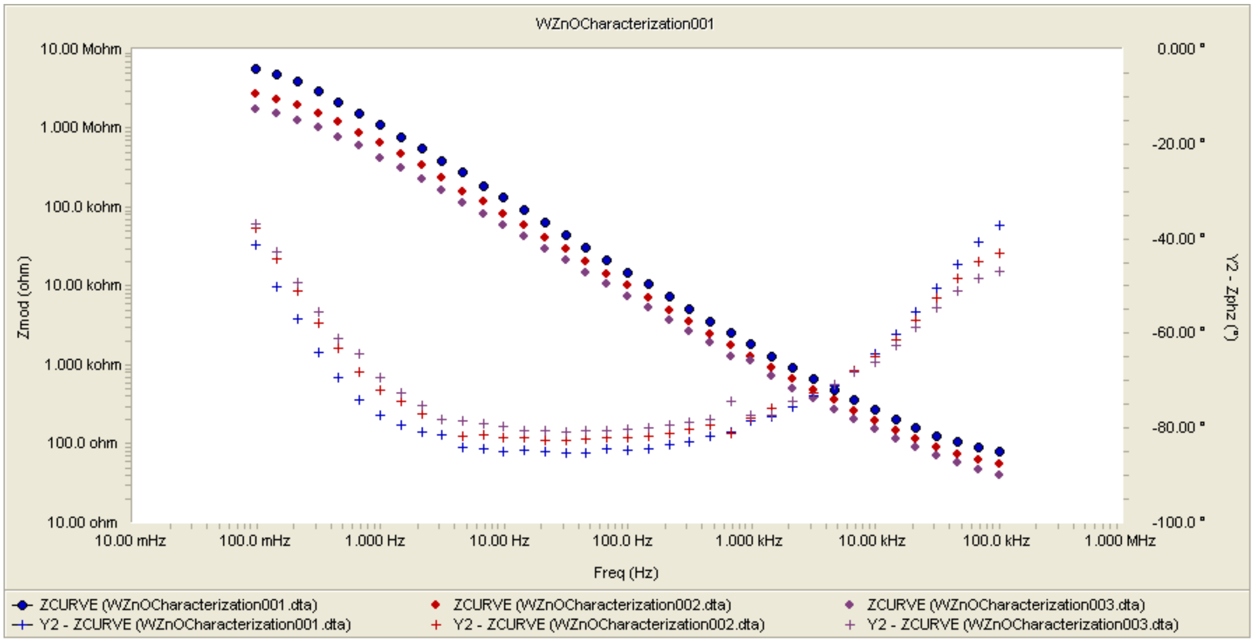

Figure 74: Variation in impedance with submersion depth variation for Zinc oxide coated electrodes. Blue curve is 2mm submersion, red curve is 5mm submersion, and purple curve is 10mm submersion

After multiple attempts to fabricate properly insulated electrodes in the clean room, epoxy coated electrodes were determined to be the best solution for this application. Experimentation suggests that submicron thick coatings are inadequate to control capacitive impedance at higher frequencies. With careful application of the epoxy coating, it was possible to make an insulating layer whose profile would provide limited interference with the underlying tissue. To achieve this profile, a drop of epoxy was placed on a smooth flat surface, and the electrode was gently rolled through the epoxy, achieving a very smooth transition between exposed tip and epoxy insulated regions. Figure 75 and Figure 76 show each epoxy insulated electrode. Figure 77 shows the EIS data for varied penetration depth. Little change in the magnitude is observed, suggesting that this insulation method is suitable for the application.

Figure 75: 1 of 2 epoxy insulated tungsten electrodes (epoxy is shiny region)

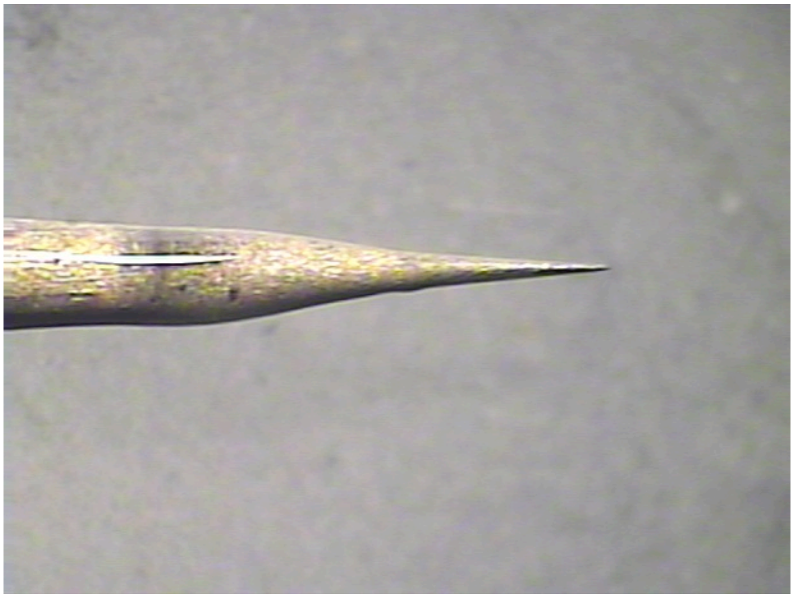

Figure 76: 2nd epoxy insulated tungsten electrode

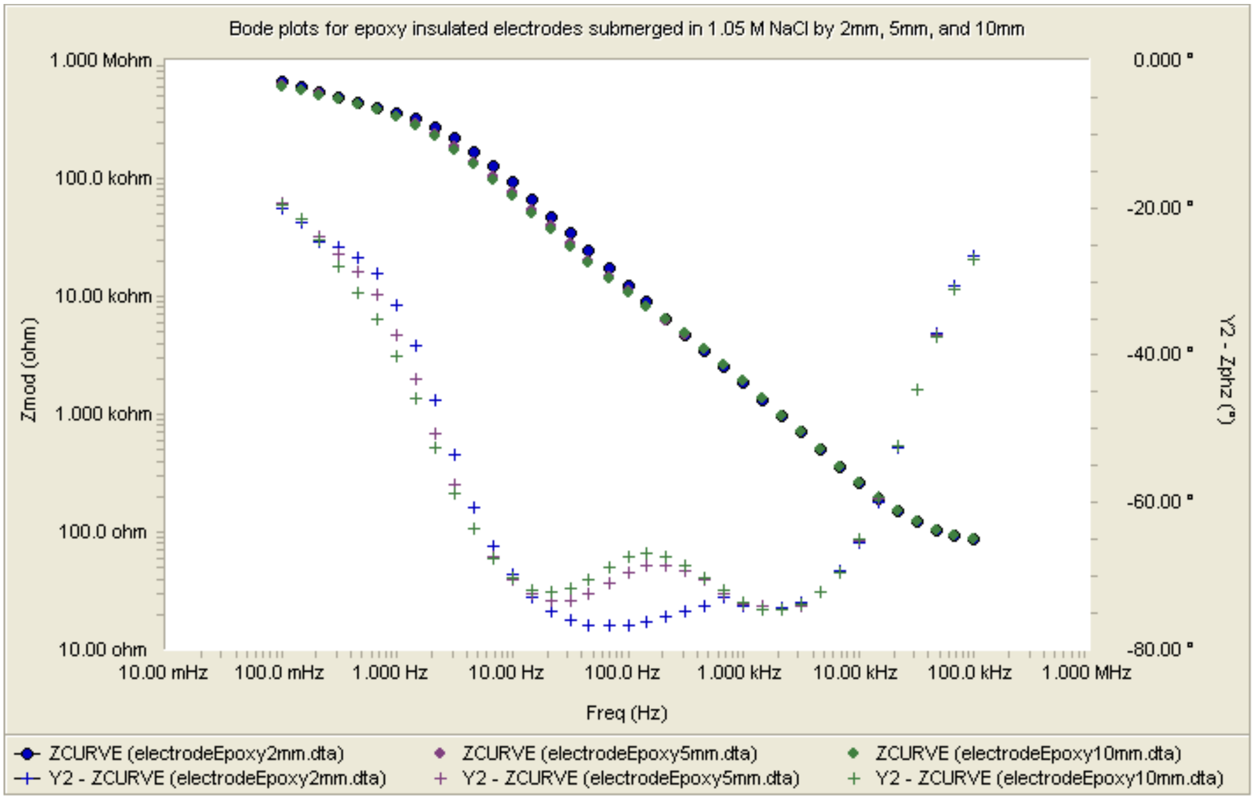

Figure 77: EIS curves for epoxy electrodes with varied penetration depth of 2mm (blue), 5mm (brown), and 10mm (green)

5.4. Experiment

The first sample was acquired and denoted lc001 (each tissue sample is identified in the format lc*xxx*). For each sample, pictures were taken or otherwise documented to show the location of each electrode penetration site and match this location with the corresponding data. This detailed organization of results is critical to collaborate the results with histology to determine if there is any association between the measured impedance spectrum and the presence of cancerous tissue, particularly in samples that contain both cancerous and healthy tissue. It is suggested by the surgeon that there will likely be healthy tissue near the periphery of certain provided samples, while the center will likely be cancerous. Figure 78, Figure 79, and Figure 80 demonstrate a sample set of measurement locations taken from a single sample. While it is important to collect data from the periphery region, it is also important to make sure that the uninsulated portion of the electrodes are fully inserted into the sample to keep the measurement volume consistent.

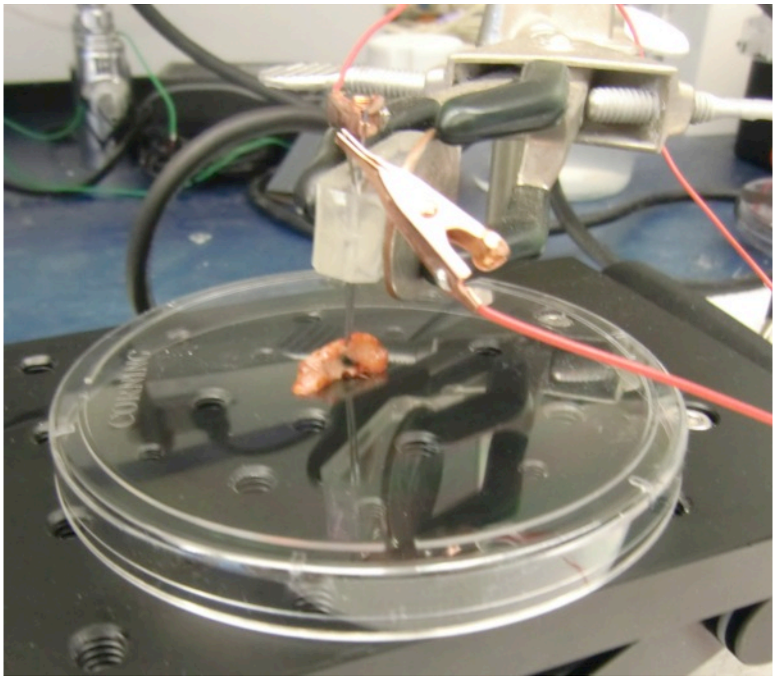

Figure 78: Measurement location 1 for sample lc001, taken from central area of sample

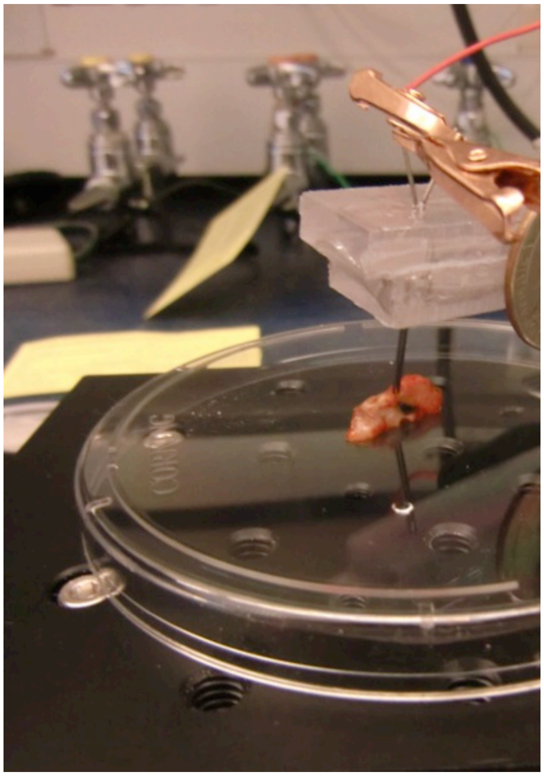

Figure 79: Location 2 for sample lc001, also taken in central region

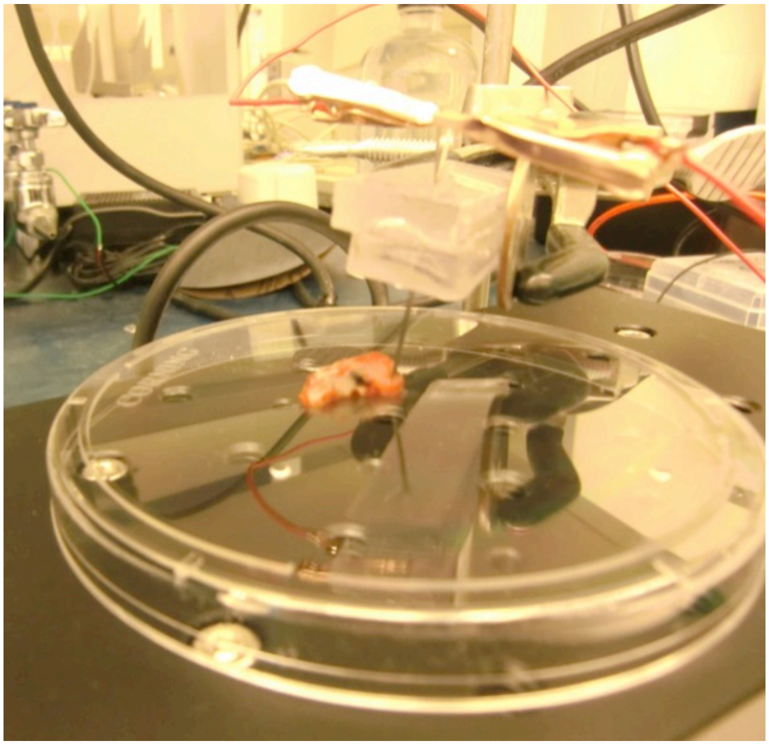

Figure 80: Location 3 for sample lc001, taken in periphery region where tissue may be healthy

5.5. Results

At the completion of this document, data has been collected from 4 samples. The available dataset permits no statistically significant conclusions regarding the potential for tissue discrimination by impedance, however, the data demonstrates a clear difference between healthy tissue and nodules of any type. Table 4 lists all collected EIS datasets, the sample it was collected from, and any relevant information about the tissue type known at this time. Further information regarding the histology of individual samples will be provided at a later date. In particular, histology has not been obtained to verify that the tissue measure in lc001_3 was actually healthy, and the tumor type is uncertain for datasets lc001_2, lc001_4, lc002_1, lc002_2, and lc002_3.

Table 4: List of datasets and samples for EIS cancer analysis

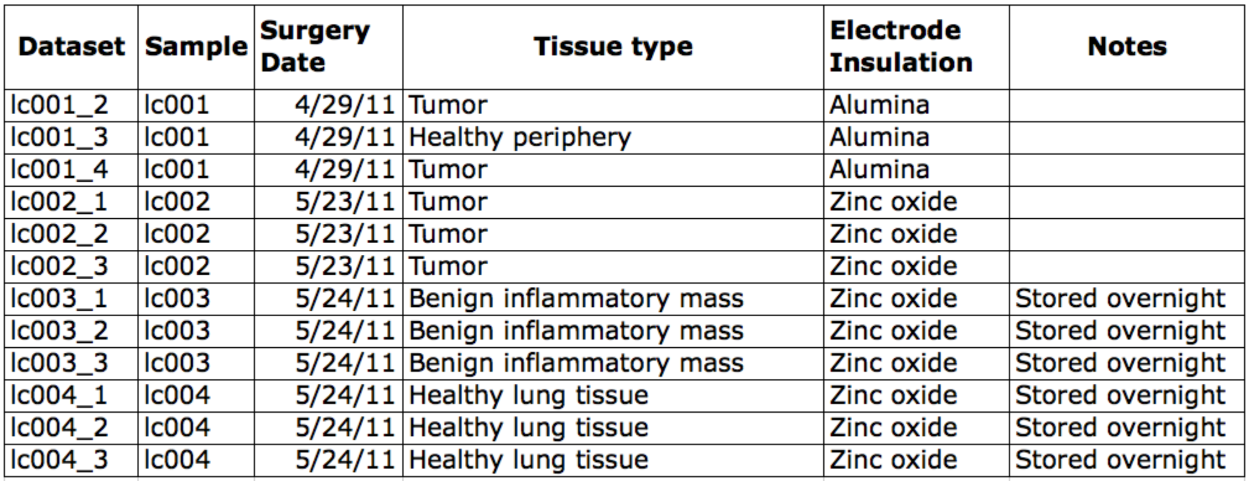

Dataset	Sample	Surgery Date	Tissue type	Electrode Insulation	Notes
lc001_2	lc001	4/29/11	Tumor	Alumina	
lc001_3	lc001	4/29/11	Healthy periphery	Alumina	
lc001_4	lc001	4/29/11	Tumor	Alumina	
lc002_1	lc002	5/23/11	Tumor	Zinc oxide	
lc002_2	lc002	5/23/11	Tumor	Zinc oxide	
lc002_3	lc002	5/23/11	Tumor	Zinc oxide	
lc003_1	lc003	5/24/11	Benign inflammatory mass	Zinc oxide	Stored overnight
lc003_2	lc003	5/24/11	Benign inflammatory mass	Zinc oxide	Stored overnight
lc003_3	lc003	5/24/11	Benign inflammatory mass	Zinc oxide	Stored overnight
lc004_1	lc004	5/24/11	Healthy lung tissue	Zinc oxide	Stored overnight
lc004_2	lc004	5/24/11	Healthy lung tissue	Zinc oxide	Stored overnight
lc004_3	lc004	5/24/11	Healthy lung tissue	Zinc oxide	Stored overnight

Figure 81 plots the 3 scans collected from sample lc001. Datasets lc001_2 and lc001_4 were collected from the thick central portion of the sample shown in Figure 78 and Figure 79. Dataset lc001_3 was taken from the periphery region shown in Figure 80, which is likely to be healthy tissue. Adequate electrode penetration was achieved for all datasets. There is a distinct difference in the behavior between the two cancerous datasets (lc001_2 and lc001_4) and the probable healthy set (lc001_3). The latter shows a peak in the phase curve at a significantly lower frequency than the other 2 datasets. The elbow observed in the magnitude of impedance plot also occurs at a significantly lower frequency. The two samples from the central tumor region show extremely consistent behavior. No conclusions can be drawn from this 1 set of measurements alone, but provide evidence supporting the potential for using EIS to discriminate between healthy and cancerous tissue.

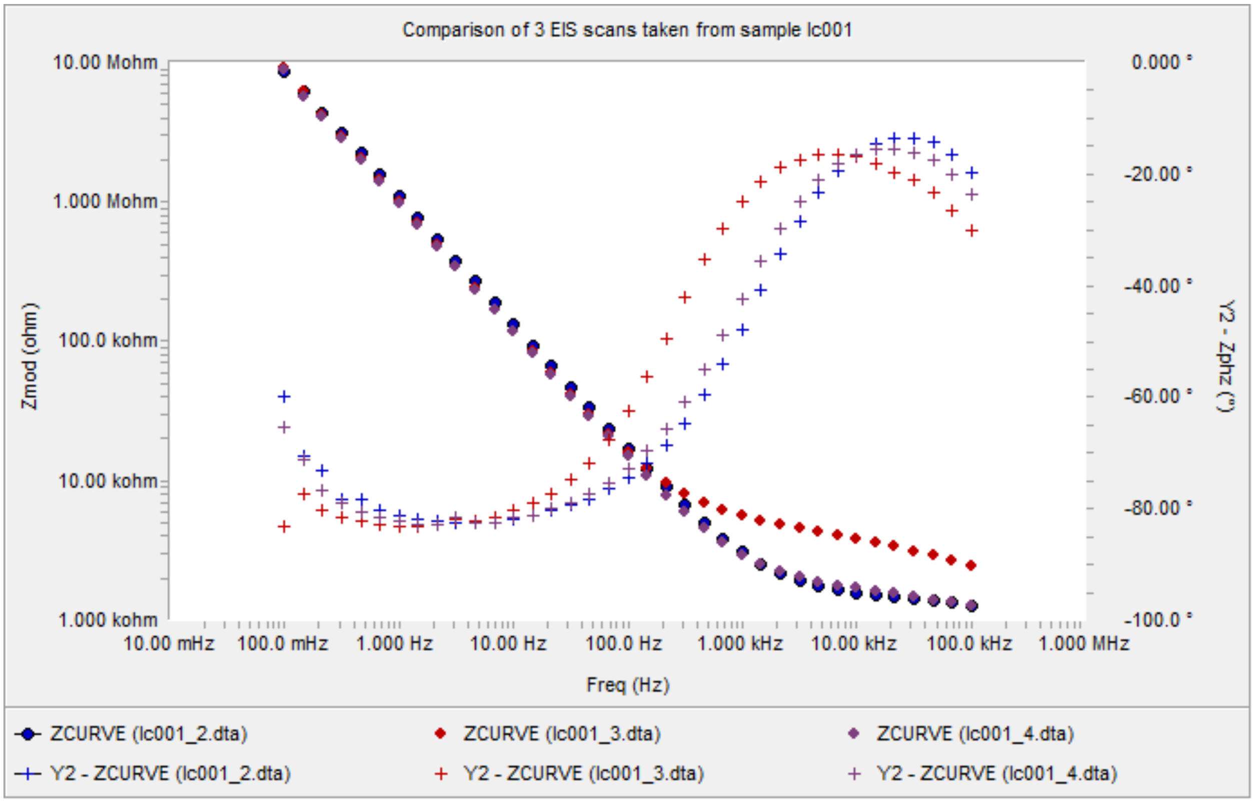

Figure 81: Comparison of Bode plots for 3 EIS scans collected with alumina insulated electrodes in sample lc001. Trial lc001_3 (red) is collected from periphery region, which is likely to be composed of healthy tissue.

Figure 82 plots the 3 datasets collected from sample lc002. All 3 datasets exhibit extremely similar behavior. Moderate variation in magnitude is observed. The zinc oxide insulated electrodes were used for this dataset, which were shown to show variation in magnitude associated with variation in penetration depth due to inadequate electrical insulation in the zinc region. As a result, the observed variation in magnitude is to be expected.

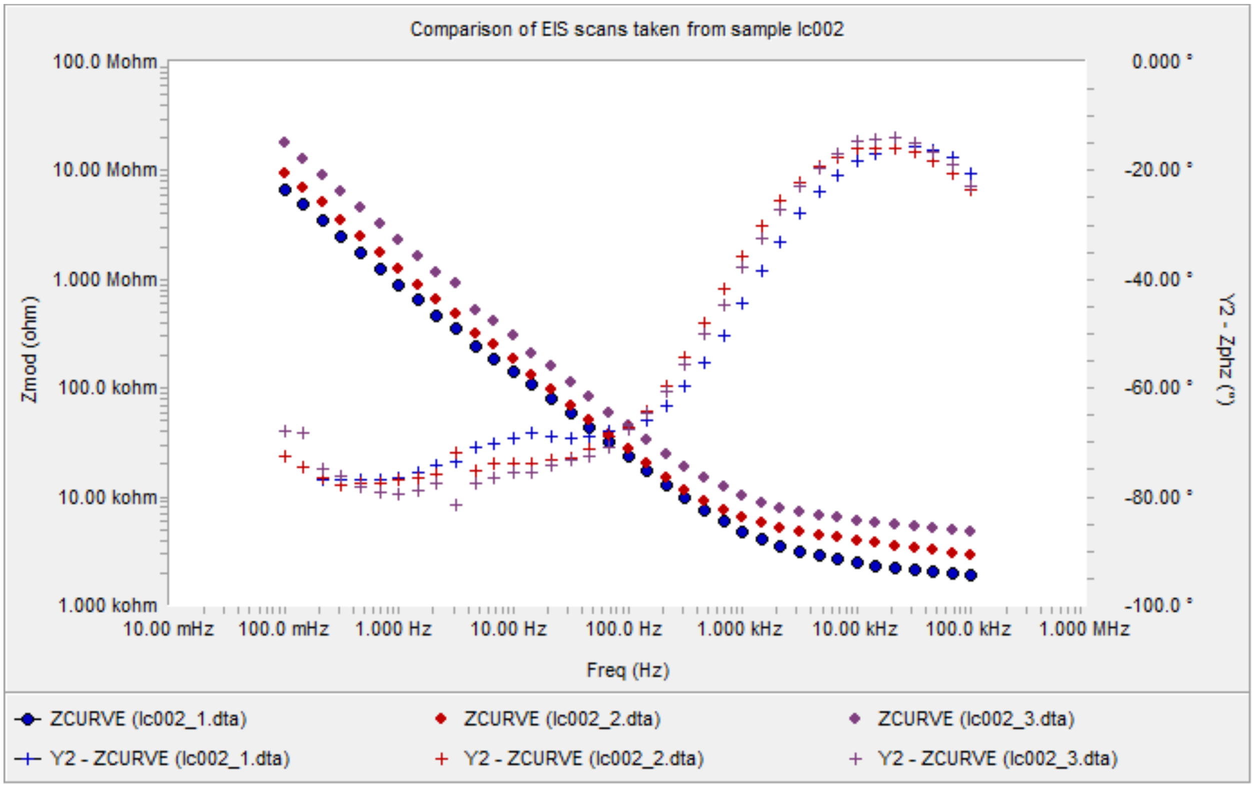

Figure 82: Comparison of Bode plots for 3 EIS scans with zinc oxide insulated electrodes from sample lc002

Figure 83 plots the 3 datasets taken from sample lc003, which was a benign inflammatory mass. The datasets were collected with the zinc insulated electrodes. All 3 datasets are extremely similar. Figure 84 plots the 3 datasets taken from sample lc004, which was normal, healthy lung tissue. Data was collected with the zinc electrodes. Both samples lc003 and lc004 were left in a cooler on ice overnight before data collection. This is not ideal as tissue impedance is sensitive to temperature and water content.

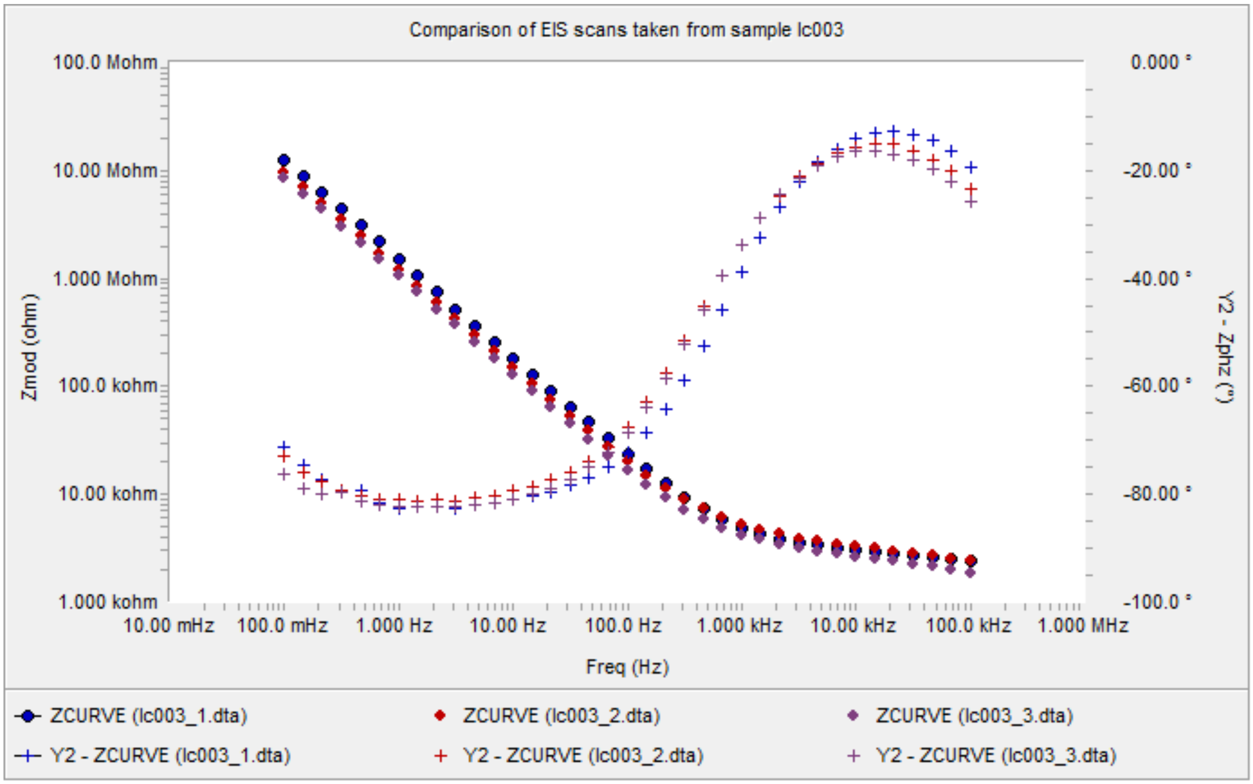

Figure 83: Comparison of Bode plots for 3 EIS scans with zinc oxide insulated electrodes from sample lc003

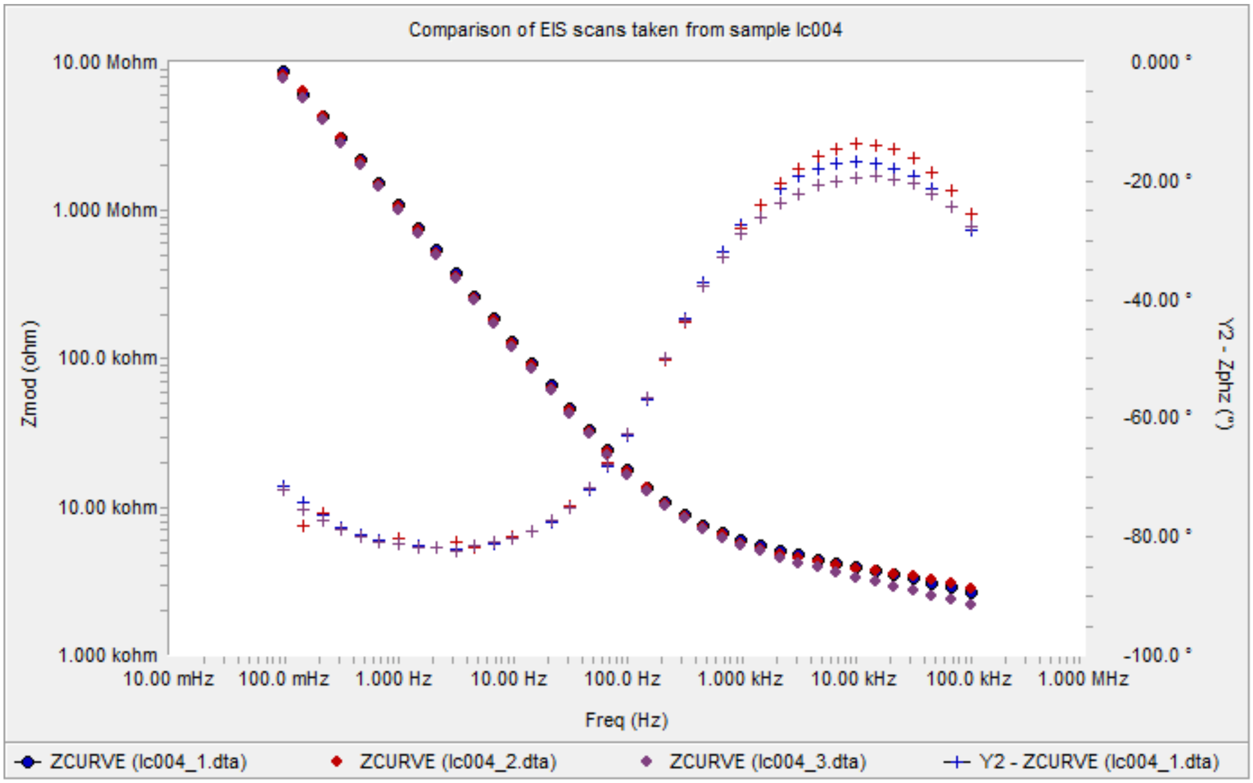

Figure 84: Comparison of Bode plots for 3 EIS scans with zinc oxide insulated electrodes in sample lc004

Figure 85 plots representative datasets from each sample collected to date. All scans from lc002, lc003, and lc004 were extremely similar, so the chosen representative dataset was arbitrary. Because data was collected from 2 distinct regions with resultant distinct data properties in sample lcc001, datasets lc001_2 and lc001_3 are included here. A clear pattern is easily observable: measurements taken from healthy tissue (lc004 and presumably lc001_3) both exhibit relative maxima at lower frequencies (approximately 8 kHz). Measurements taken from nodules, benign or malignant, show relative maxima at higher frequencies (approximately 20 kHz). The associated Nyquist plots, presented in Figure 86, show a similar shift between healthy tissue and nodules, both malignant and benign. While this is an interesting distinction, the end goal of this project is to provide a means to distinguish between benign lung nodules and malignant tumors.

Data from sample lc002 shows an interesting deviation in the phase plot at approximately 10 Hz when compared to all other samples. The source of the deviation is currently unknown. This phenomena will be investigated further with the accumulation of more EIS data from additional samples and corresponding histology.

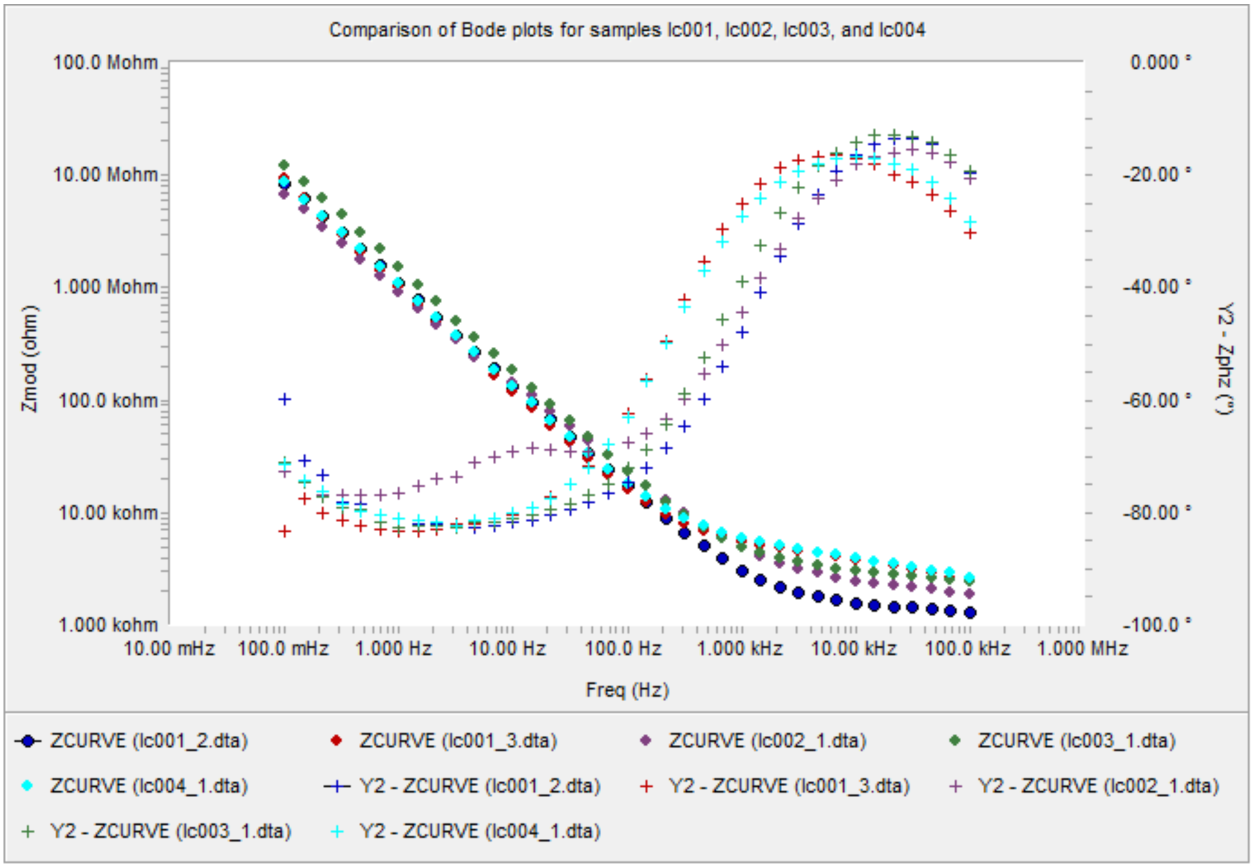

Figure 85: Comparison of representative EIS data for samples lc001, lc002, lc003, and lc004

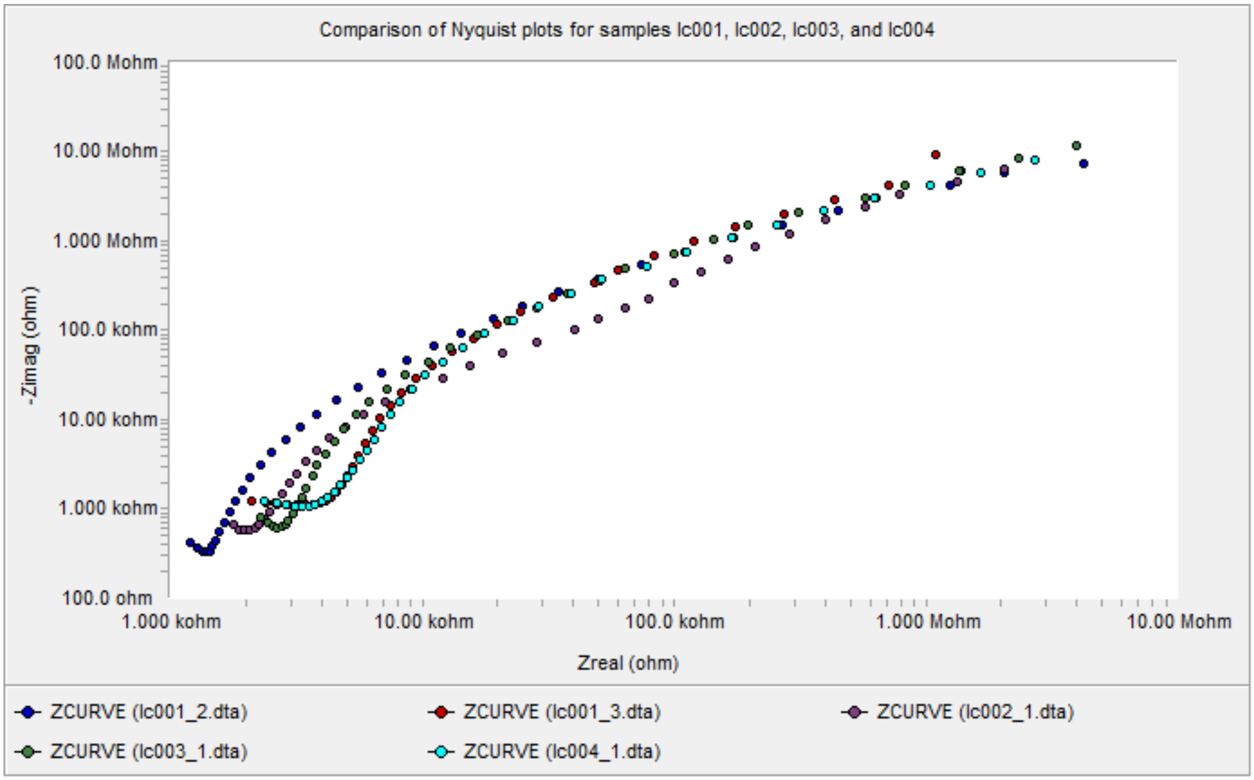

Figure 86: Comparison of Nyquist plots for representative data from samples lc001, lc002, lc003, and lc004

6. Conclusions

The research summarized in this document made several accomplishments to further work in the Nanoworld lab. Methods for making EIS readings across implanted samples were developed and refined. Corrosion and biofouling phenomena were observed using these methodologies. Insulated CNT thread was successfully used as a copper wire replacement for transdermal power transfer. Future experimentation in this lab will continue to use these techniques to further efforts to apply cathodic protection to increase control of the biodegradation of implanted devices.

Experimental methods for employing EIS in tissue analysis were developed. Custom electrode setups were developed and optimized for this line of research. Preliminary data was collected, showing distinct, consistent differences between certain classes of tissue. Data was collected from 4 different human lung tissues for use in the study of applying EIS to differentiate malignant lung cancer from benign nodules. This data appears to permit easy distinction between healthy lung tissue and nodules. No distinguishing features have been found to date to distinguish between benign nodules and malignant tumors. The data collection from human samples will continue past the completion of this document.

7. References

1. Wang, J. Analytical Electrochemistry, 2nd ed. New York: Wiley, 2000.

2. Grimnes, S., and Martinsen, O.G. *Bioimpedance & Bioelectricity Basics.* London: Academic Press, 2000.

3. C. Gabriel, S. Gabriel, E. Corhout. "The dielectric properties of biological tissues: I. Literature survey." *Physics in Medicine and Biology* 41 (1996): 2231-2249.

4. S. Gabriel, R.W. Lau, C. Gabriel. "The dielectric properties of biological tissues: II. Measurements in the frequency range 10 Hz to 20 GHz." *Physics in Medicine and Biology* 41 (1996): 2251-2269.

5. S. Gabriel, R.W. Lau, C. Gabriel. "The dielectric properties of biological tissues: III. Parametric models for the dielectric spectrum of tissues." *Physics in Medicine and Biology* 41 (1996): 2271-2293.

6. Perez, N. *Electrochemistry and Corrosion Science.* Norwell: Kluwer Academic Publishers, 2004.

7. J. Chen, J. Wang, E. Han, J. Dong, W. Ke. "AC impedance spectroscopy study of the corrosion behavior of an AZ91 magnesium alloy in 0.1 M sodium sulfate solution." *Electrochimica Acta* 52 (2007): 3299-3309.

8. H.M. Wong, K.W.K. Yeung, K.O. Lam, V. Tam, P.K. Chu, K.D.K. Luk, K.M.C. Cheung. "A biodegradable polymer-based coating to control the performance of magnesium alloy orthopaedic implants." *Biomaterials* 31 (2010): 2084-2096.

9. Y. Yun, Z. Dong, D. Yang, M.J. Schulz, V.N. Shanov, S. Yarmolenko, Z. Xu, P. Kumta, C. Sfeir. "Biodegradable Mg corrosion and osteoblast cell culture studies." *Materials Science and Engineering C.* 29 (2009): 1814-1821.
10. W.J. Lorenz, F. Mansfeld. "Determination of corrosion rates by electrochemical DC and AC methods." *Corrosion Science* 21 (1981): 647-672.
11. P.L. Bonora, F. Deflorian, L. Fedrizzi. "Electrochemical impedance spectroscopy as a tool for investigating underpaint corrosion." *Electrochimica Acta* 41 (1996): 1073-1082.
12. N.T. Kirkland, J. Lespagnol, N. Birbilis, M.P. Staiger. "A survey of bio-corrosion rates of magnesium alloys." *Corrosion Science* 52 (2010): 287-291.
13. L. Yang, Y. Wei, L. Hou, D. Zhang. "Corrosion behaviour of die-cast AZ91D magnesium alloy in aqueous sulphate solutions." *Corrosion Science* 52 (2010): 345-351.
14. C. Liu, Q. Bi, A. Leyland, A. Matthews. "An electrochemical impedance spectroscopy study of the corrosion behaviour of PVD coated steels in 0.5 N NaCl aqueous solution: Part II. EIS interpretation of corrosion behavioiur." *Corrosion Science* 45 (2003): 1257-1273.
15. Juttner, K. "Electrochemical impedance spectroscopy (EIS) of corrosion processes on inhomogenous surfaces." *Electrochimica Acta* 35 (1990): 1501-1508.
16. M. Kendig, F. Mansfeld, S. Tsai. "Determination of the long term corrosion behavior of coated steel with A.C. impedance measurements." *Corrosion Science* 23 (1983): 317-329.
17. Mansfeld, F. "Use of electrochemical impedance spectroscopy for the study of corrosion protection by polymer coatings." *Journal of Applied Electrochemistry* 25 (1995): 187-202.
18. C.T. Chen, B.S. Skerry. "Assessing the corrosion resistance of painted steel by AC impedance and electrochemical noise techniques." *Corrosion* 47 (1991): 598-611.

19. D.W. Law, S.G. Millard, J.H. Bungey. "Galvanostatic pulse measurements of passive and active reinforcing steel in concrete." *Corrosion* 56 (2000).

20. F. Mansfeld, B. Little. "A technical review of electrochemical techniques applied to microbiologically influenced corrosion." *Corrosion Science* 32 (1991): 247-272.

21. F. Mansfeld, M.W. Kendig, S. Tsai. "Evaluation of corrosion behavior of coated metals with AC impedance measurements." *Corrosion* 38 (1982): 478-485.

22. G. Baril, C. Blanc, N. Pebere. "AC impedance spectroscopy in characterizing time-dependent corrosion of AZ91 and AM50 magnesium alloys." *Journal of the Electrochemical Society* 148 (2001): B489-B496.

23. G. El-Mahdy, A. Nishikata, T. Tsuru. "AC impedance study on corrosion of 55% Al-Zn alloy-coated steel under thin electrolyte layers." *Corrosion Science* 42 (2000): 1509-1521.

24. G. Song, A. Atrens, D. St John, X. Wu, J. Nairn. "The anodic dissolution of magnesium in chloride and sulphate solutions." *Corrosion Science* 39 (1997): 1981-2004.

25. J.E. da Silva, J.P.M. de Sa, J. Jossinet. "Classification of breast tissue by electrical impedance spectroscopy." *Medical & Biological Engineering & Computing* 38 (2000): 26-30.

26. R.J. Halter, A. Hartov, J.A. Heaney, K.D. Paulsen, A.R. Schned. "Electrical impedance spectroscopy of the human prostate." *IEEE Transactions on Biomedical Engineering* 54 (2007): 1321-1327.

27. B.R. Lee, W.W. Roberts, D.G. Smith, H.W. Ko, J.I. Epstein, K. Lecksell, A.W. Partin. "Bioimpedance: Novel use of a minimally invasive technique for cancer localization in the intact prostate." *The Prostate* 39 (1999): 213-218.

28. L. Tang, C. Yao, C. Sun. "Apoptosis induction with electrical pulses - A new approach to cancer therapy with drug free." *Biochemical and Biophysical Research Communications* 390 (2009): 1098-1101.

29. P. Aberg, I. Nicander, J. Hansson, P. Geladi, U. Holmgren, S. Ollmar. "Skin cancer identification using multifrequency electrical impedance - a potential screening tool." *IEEE Transactions on Biomedical Engineering* 51 (2004): 2097-2102.

30. L. Sha, E.R. Ward, B. Stroy. "A review of dielectric properties of normal and malignant breast tissue." *Proccedings IEEE SoutheastCon*, 2002: 457-462.

31. A. Keshtkar, A. Keshtkar, R.H. Smallwood. "Electrical impedance spectroscopy and the diagnosis of bladder pathology." *Physiological Measurement* 27 (2006): 585-596.

32. B.H. Brown, J.A. Tidy, K. Boston, A.D. Blackett, R.H. Smallwood, F. Sharp. "Relation between tissue structure and imposed electrical current flow in cervical neoplasia." *The Lancet* 355 (2000): 892-895.

33. C. Skourou, P.J. Hoopes, R.R. Strawbridge, K.D. Paulsen. "Feasibility studies of electrical impedance spectroscopy for early tumor detection in rats." *Physiological Measurement* 25 (2004): 335-346.

34. Jossinet, J. "Variability of impedivity in normal and pathological breast tissue." *Medical & Biological Engineering & Computing* 34 (1996): 346-350.

8. Appendices: Preliminary tissue discrimination dataset

The following images show two sets of measurements taken from tissue samples from a mouse. The first set uses uninsulated electrodes and consequentially provides an inconsistent measurement volume. The second set uses refined equipment to improve the data. In particular, an insulated set of electrodes was used in conjunction with a controlled lift for electrode placement. E1 denotes experiment set 1. E2 denotes experiment set 2.

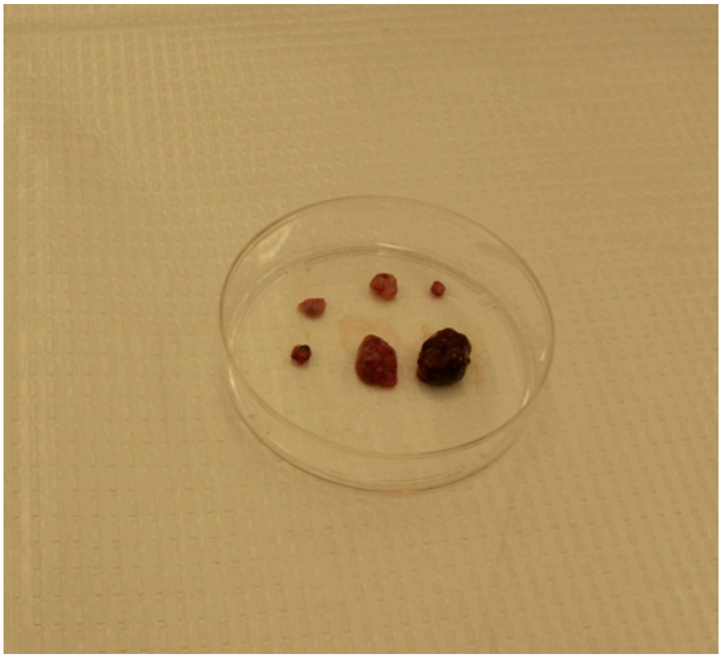

Figure 87: Tissue samples for preliminary EIS

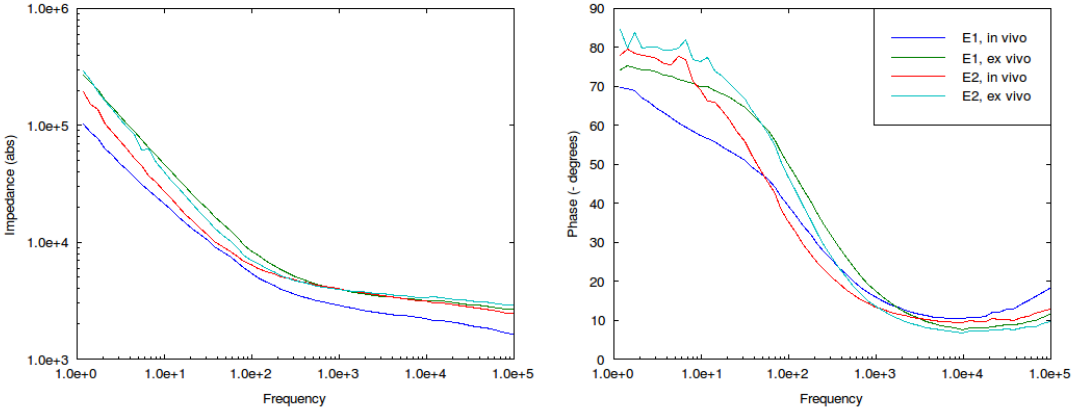

Figure 88: EIS scans of brain tissue

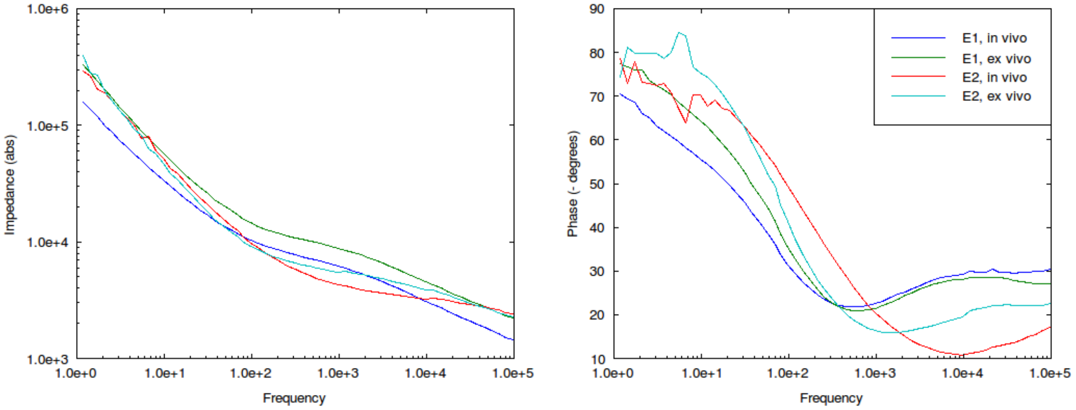

Figure 89: EIS scans of heart tissue

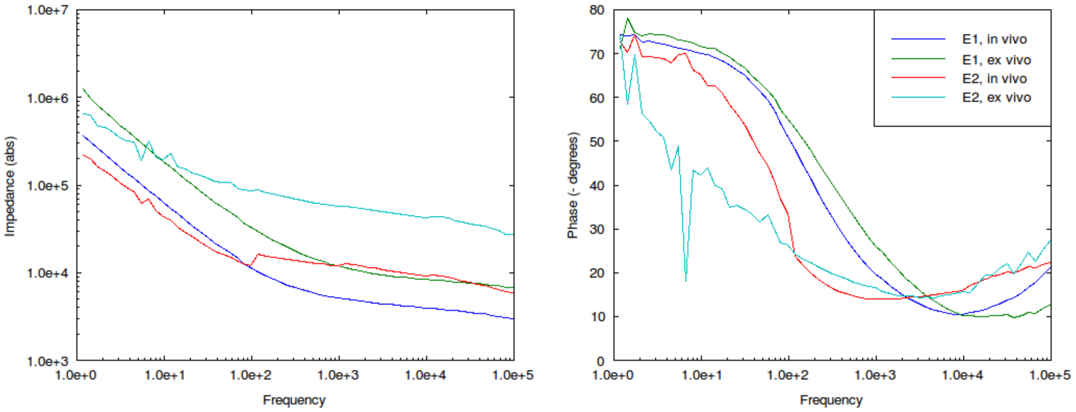

Figure 90: EIS scans of intestine tissue

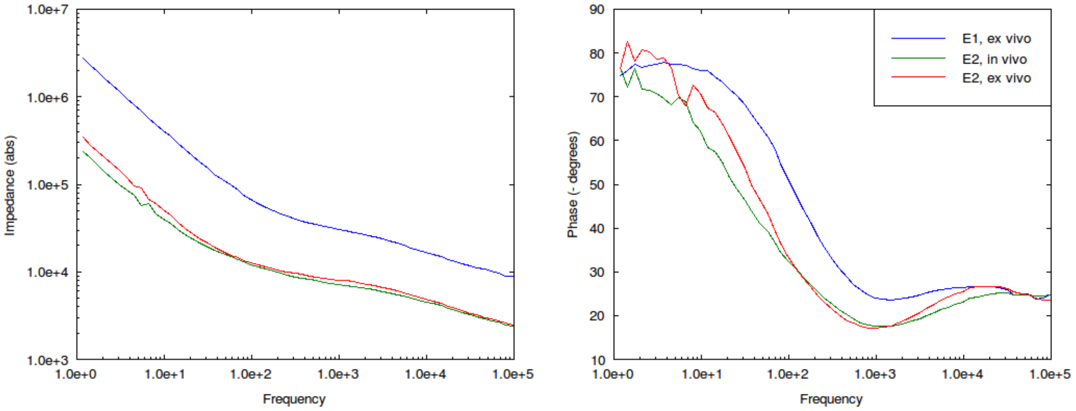

Figure 91: EIS scans of kidney tissue

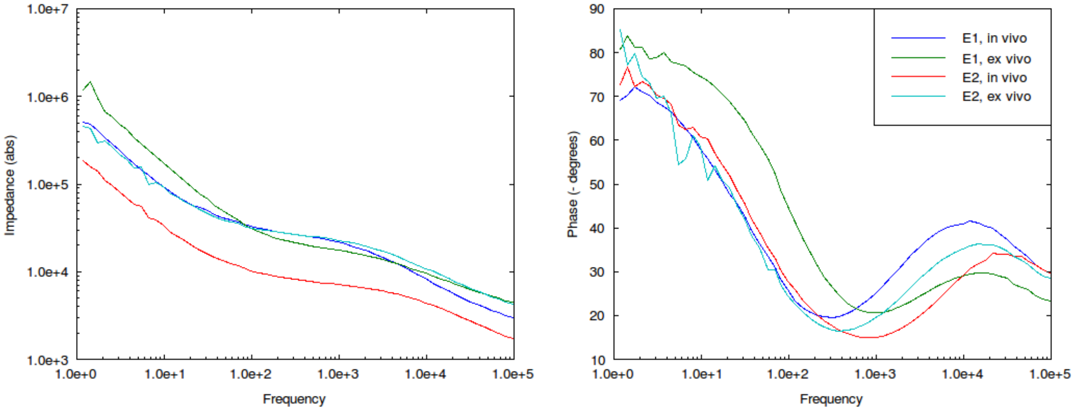

Figure 92: EIS scans of liver tissue

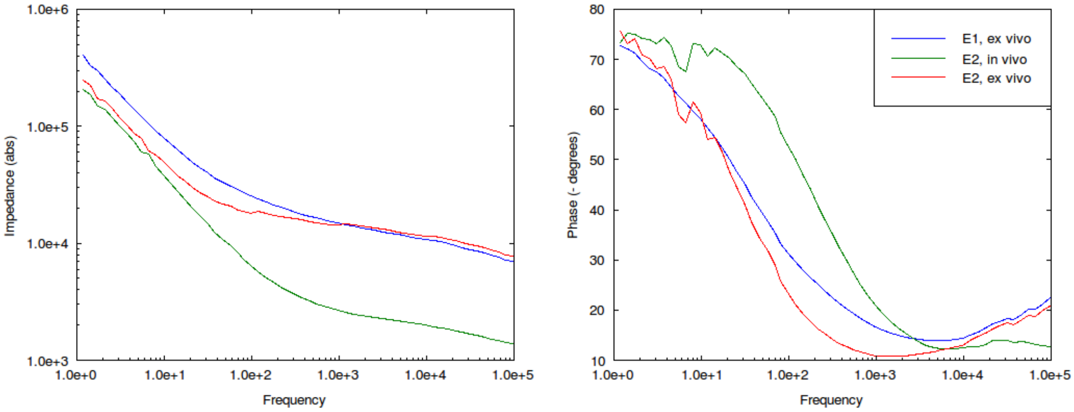

Figure 93: EIS scans of lung tissue

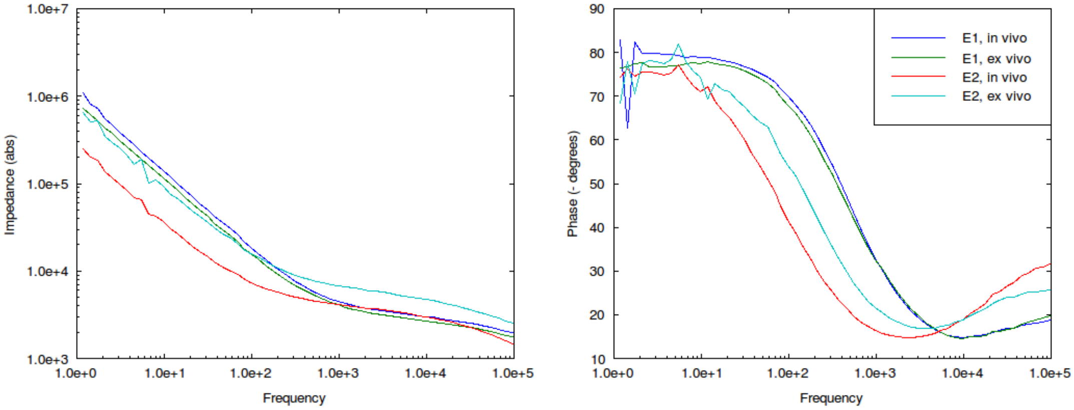

Figure 94: EIS scans of muscle tissue

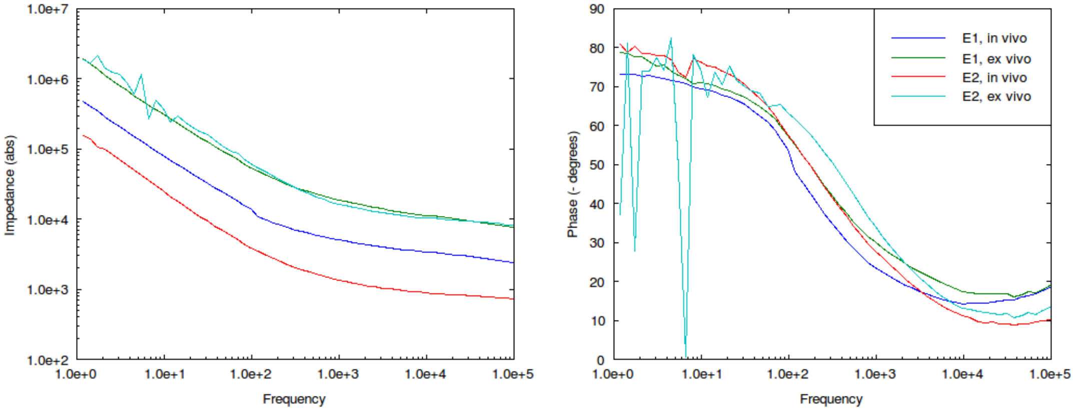

Figure 95: EIS scans of prostate tissue

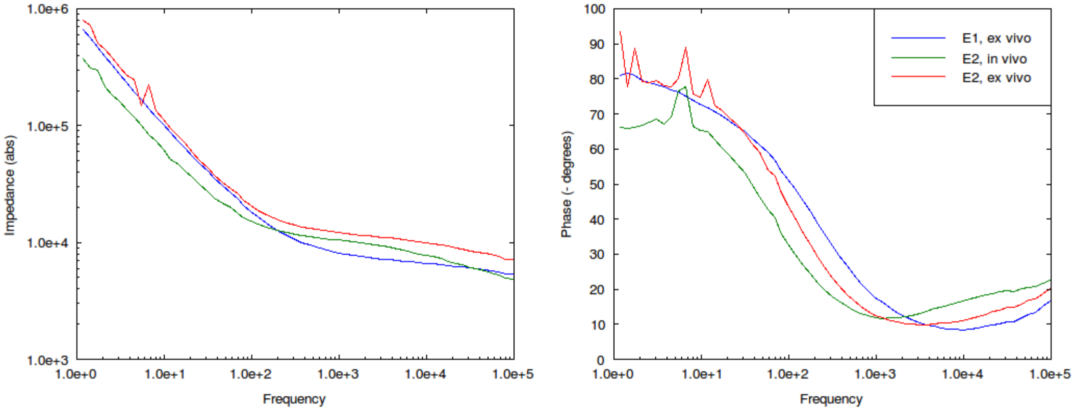

Figure 96: EIS scans of spleen tissue